

XIV<sup>th</sup> Pan-American  
Current Research  
On Fluid Inclusions

# PACROFI 14



June 12-14, 2018



Rice University, Houston, Texas, U.S.A.



The XIV<sup>th</sup> “Edwin W. Roedder”  
**Pan-American Current**  
**Research on Fluid Inclusions**  
Conference

Conveners

Michael P. Smith and Gary G. Gray

**Abstracts with Program**

Edited by

Andras Fall

June 12-14, 2018

Rice University, Houston, Texas, U.S.A.



## Preface

We are happy to welcome everyone to the 14<sup>th</sup> Pan-American Current Research on Fluid Inclusions Conference, held for the first time at Rice University, in Houston, Texas...The energy capital of the world. It is no accident that this year's program will highlight applications of fluid inclusions for the exploration, development, and production of hydrocarbon resources. We also have a full slate of presentations on advances in analytical techniques, melt inclusions, ore deposits, plus a few talks that range from ancient atmosphere inclusions in ice cores to direct samples of aqueous fluids in the early solar system! Our post-meeting field trip will venture down to South Texas to see active drilling in the Eagle Ford 'shale' unconventional oil play.

We would like to thank the many entities that have made this meeting possible. Rice University and the Department of Earth, Environmental, and Space sciences in particular for their sponsorship of this meeting for granting us access to their excellent facilities. We'd also like to thank our principal co-sponsor, Advanced Hydrocarbon Stratigraphy, in Tulsa, OK, Thanks also to Core Labs for sponsoring the post-meeting field trip, and to McCrone Microscopes and Accessories, and AWL Mud Logging for their support. PACROFI (and sister act ECROFI) is a unique and entirely volunteer organization. We invite everyone who is interested in the future of PACROFI to come and provide their input at the business meeting on Wednesday night at the conference banquet. Thanks to everyone for your participation in the meeting.

The Organizing Committee,  
PACROFI XIV, June 2018

**ON THE COVER:** Photomicrograph of an oil inclusion trapped in doubly-terminated quartz crystal from Belochistan, Pakistan, shown under combined transmitted and UV-fluorescent lights. This inclusion is exceptionally large, approximately 1500 microns in largest dimension. Multiple phases are visible, including a large gas bubble, blue-fluorescent oil, and dark "blebs" of asphaltene precipitate. The API gravity of this oil determined from quantitative fluorescence spectroscopy is approximately  $41.4 \pm 3.9$  °API. *Courtesy of Steve Becker.*

# Acknowledgements

The PACROFI 14 organizing committee would like to thank the following persons and sponsoring companies for their support for the meeting:

## Keynote Speakers:

Bob Burruss	USGS (retired)
Pilar Lecumberri-Sanchez	University of Alberta
Dan Marshall	Simon Fraser University
Jacques Pironon	Université de Lorraine
Ed Waddington	University of Washington
Jim Webster	American Museum of Natural History
Zoltán Zajacz	University of Toronto
Mike Zolensky	NASA Johnson Space Center

## Sponsors:

The McCrone Group  
AWL Services  
Core Labs  
Advanced Hydrocarbon Stratigraphy  
Department of Earth, Environmental and Planetary Sciences, Rice University

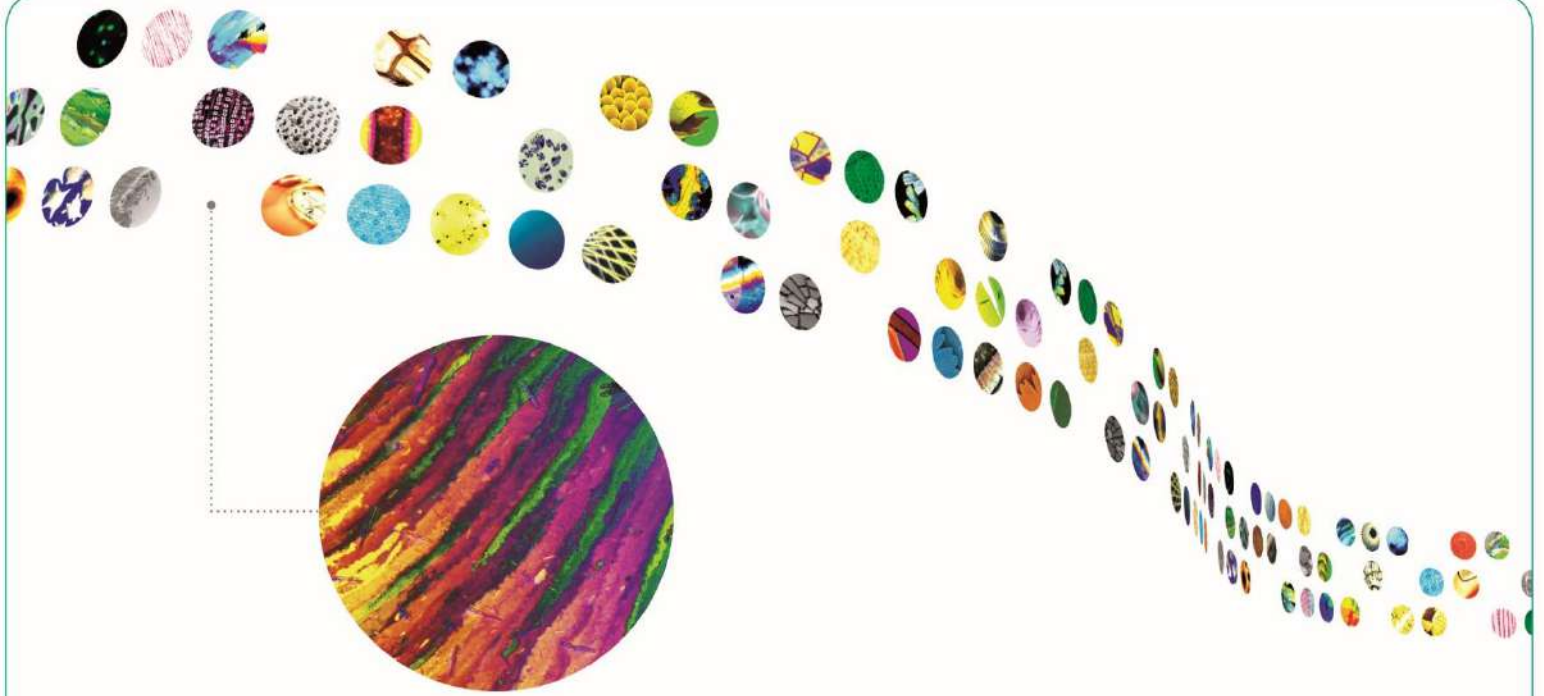
## Organizing and Scientific Committee:

Mike Smith	Advanced Hydrocarbon Stratigraphy
Gary Gray	Rice University
Steve Becker	ExxonMobil URC
Ash Bigge	Consultant
Katrina Cox	CoreLabs
András Fall	The University of Texas at Austin
Janet Haggerty	University of Tulsa
Don Hall	Schlumberger, FIT
Cyn-Ty Lee	Rice University
Zhaoqi Li	University of Kansas, CGG
Gordon MacLeod	Chesapeake Energy
Bob Pottorf	ExxonMobil URC (retired)
Jinny Sisson	University of Houston
Dennis Smith	ExxonMobil URC (retired)
Mike Sterner	Schlumberger, FIT

## Our Sponsors

We would like to thank the following companies and organizations for their gracious support for our conference:





# UNLIMITED SCOPE

in Fluid Inclusion Research

For more than 60 years, McCrone Microscopes & Accessories has provided instrumentation and expert consultation to geologists worldwide. We are proud to sponsor the PACROFI 2018 meeting.

Let our technical experts show you how a McCrone fluid inclusion microscope system effectively allows fluid inclusionists to study melt and fluid inclusion behavior. With research-grade Nikon and Olympus microscopes, Linkam thermal stages, and digital microscope cameras, the McCrone fluid inclusion microscope system remains the industry standard.

Call today, 800-622-8122, or email [mmaorder@mccrone.com](mailto:mmaorder@mccrone.com) to find the optimal equipment for you and your geological laboratory.

 **McCRONE**<sup>™</sup>  
**MICROSCOPES & ACCESSORIES**  
[www.mccrone.com/instrument-sales](http://www.mccrone.com/instrument-sales)

850 Pasquinelli Drive • Westmont, Illinois 60559



# EC

# R



# FI

**BUDAPEST,**

**HUNGARY**

**11-18<sup>TH</sup> AUGUST**

**2019**

***<http://ecrofi2019.elte.hu/>***

- **THE WEEK BEFORE GOLSCHMIDT2019 CONFERENCE BARCELONA**
- **PLENARY SESSIONS, FIELD TRIP TO BAKONY-BALATON-HIGHLAND, WORKSHOPS**
- **HOST INSTITUTE: LITHOSPHERE FLUID RESEARCH LAB, EÖTVÖS LORÁND UNIVERSITY**

***LOOKING FORWARD TO SEEING YOU IN  
BUDAPEST IN 2019!***







# Conference Schedule

PACROFI 14, 2018

(\* – not presented)

## Monday, June 11

7:00-9:00 pm Registration – Keith-Wiess Geological Labs

## Tuesday, June 12

Main meeting venue is at Sewall Hall, Room 301

7:00-8:30 Registration – Sewall Hall 301

8:30 Welcome and Intro

### Session 1: Sedimentary and Petroleum Inclusions

*Session Chair: Bob Pottorf*

8:40 Jacques PIRONON

▶ **Keynote Lecture:** Hydrocarbon inclusions: the story

9:20 Stephen P. BECKER

▶ Fluid inclusion tools in petroleum systems analysis

9:50 Erich de Zoeten, Robert H. GOLDSTEIN

▶ Open system diagenesis in unconventional reservoirs of the Midland Basin, Howard County, Texas

10:20 **Break**

*Session Chair: Bob Burruss*

10:40 Michael P. SMITH

▶ Rock volatiles stratigraphy: A tool for petroleum exploration and production

11:20 Zhaoyi LI, Robert H. Goldstein, Evan Franseen

▶ Application of fluid inclusions to study low-temperature diagenesis in Miocene carbonates, La Molata, SE Spain

- 11:40 **András FALL**, Robert J. Bodnar
- ▶ Constraining the history of fluid events using the fluid inclusion assemblage (FIA) method for collecting, displaying and interpreting microthermometric data
- \*[(**Guangxi OU**, Min Zhang, Tieguan Wang, Di Wu, Qiong Li, Jian Ma
- \*▶ Characteristics and significance of fluid inclusions in the Longmaxi Shale in the Jiaoshiba area, Eastern Sichuan Basin]]

**12:10 Lunch**

*Session Chair: Jacques Pironon*

- 1:20 **Robert C. BURRUSS**
- ▶ **Keynote Lecture:** Quantitative Raman spectroscopy of single phase hydrocarbon gas-rich fluid inclusions
- 2:00 **Julien BOURDET**, Claudio Delle Piane, Chen Qiu, Martin Frenz
- ▶ **Invited lecture:** Investigation of monophasic water inclusions in quartz cement: An example from the Triassic Lesueur Sandstone aquifer, Perth Basin, Australia
- 2:20 **Eszter SENDULA**, Benjamin C. Gill, J. Donald Rimstidt, Tim K. Lowenstein, Javier García-Veigas, Robert J. Bodnar
- ▶ Redox evolution of seawater in the Late-Permian Zechstein Basin: implications from redox-sensitive trace elements in fluid inclusions in halite
- \*[(**Min ZHANG**, Guangxi Ou
- \*▶ Application of fluid inclusions to study shale hydrocarbon: A case study of Shaxin Well #2 on the southwestern margin of the Paleogene Qaidam Basin, northwest China]]
- 2:40 **Volker LÜDERS**, Johannes Schoenherr, Marta Sośnicka
- ▶ Origin of CO<sub>2</sub>-rich Zechstein-2-Carbonate-hosted gas reservoirs in the Lower Saxony Basin, NW Germany

**3:00 Break**

*Session Chair: Steve Becker*

- 3:20 **Sandra SILJESTRÖM**, Robert Pottorf, Sebastien Dreyfus, Stephen P. Becker
- ▶ **Invited Lecture:** Determination of source rock facies of oils trapped in single inclusions by ToF-SIMS

- 3:40 **Alexy ELIAS BAHNAN**, J. Pecqueur, J. Pironon, C. Carpentier, E.C. Gaucher, S. Calassou, A. Virgone  
 ▶ Diagenesis and fluid-rock interactions in the Upper Lacq carbonate petroleum reservoir, Southwestern France
- 4:00 **Marta SOŚNICKA**, Volker Lüders  
 ▶ Fluid inclusion evidence for methane-dominated thermochemical sulfate reduction in the North German Basin
- 4:20 **Julien BOURDET**, Richard Kempton  
 ▶ Attributes of petroleum inclusion assemblages for unravelling charge history
- 4:40 **Edwin D. WADDINGTON**  
 ▶ **Keynote Lecture:** Fluid inclusions in ice
- 5:30 **Icebreaker + Poster presentations**  
 - **Keith-Wiess Geological Labs**

## Wednesday, June 13

### **Session 2: Theoretical/Analytical/Experimental Advances**

*Session Chair: András Fall*

- 9:00 **Zoltán ZAJACZ**, Alexandra Tsay, Nuur Ghazali  
 ▶ **Keynote Lecture:** The fate of sulfur at the magmatic-hydrothermal transition in the porphyry ore-forming environment
- 9:40 Guillaume Barré, **Raymond MICHELS**, Laurent Truche, Valérie Burklé-Vitzthum, Catherine Lorgeoux  
 ▶ Geochemistry alive: How natural fluid inclusions and capillary reactors help unravel sulfur reactivity during Thermochemical Sulfate Reduction
- 10:00 **Hector M. LAMADRID**, Zoltán Zajacz  
 ▶ **Invited Lecture:** Rates of serpentinization in pyroxene micro-reactors

**10:20      Break**

*Session Chair: Martin Appold*

- 10:40      **Dan Marshall**, Brandon Boucher, Chris McFarlane  
 ▶ On the use of LA-ICP-MS spectrometry chemical mapping to identify the relative timing of healed mineral fractures and contained fluid inclusion assemblages
- \*[(**Matthew STEELE-MACINNIS**, Kyle T. Ashley, Drew W. Barkoff  
 \*▶ **Invited Lecture:** Mineral inclusion thermobarometry: A new approach to estimate the temperatures and pressures of hydrothermal ore formation)]
- 11:00      **D. Matthew SUBLETT Jr.**, Hector. M. Lamadrid, Matthew Steele-MacInnis, Georg Spiekermann, Robert J. Bodnar  
 ▶ N<sub>2</sub>, CO<sub>2</sub>, and CH<sub>4</sub> fugacities determined for gas mixtures from 10-500 bars at 22 °C using Raman spectroscopy
- 11:20      **Yury I. KLYUKIN**, Robert J. Bodnar  
 ▶ P-T paths of H<sub>2</sub>O-NaCl fluid inclusions during heating to the homogenization temperature
- 11:40      **Discussion**  
 \*[(**Matthew STEELE-MACINNIS**  
 \*▶ A model for composition and density of H<sub>2</sub>O-NaCl-CO<sub>2</sub> fluid inclusions)]

**12:00      Lunch**

**Session 3: Melts/Magmas/Volcanoes**

*Session Chair: Dan Marshall*

- 1:30      **Jim WEBSTER**  
 ▶ **Keynote Lecture:** Reassessing Cl in melt inclusions: New insights on magma and magmatic fluid geochemistry based on Cl solubility in silicate melts
- 2:10      **Celestine N. MERCER**, Kathryn E. Watts, Albert H. Hofstra, Zoltán Zajacz, Matthew A. Coble  
 ▶ **Invited Lecture:** Metal and volatile budget of rhyolite magmas coincident with Nevada's world-class Carlin-type gold deposits

- 2:30 Tibor Guzmics, **Márta BERKESI**, Ralf Milke, Csaba Szabó  
▶ **Invited Lecture:** A new approach to understand natrocarbonatite formation based on melt and fluid inclusions from the Kerimasi volcano, Tanzania
- 2:50 **Lowell R. MOORE**, Esteban Gazel, Robert J. Bodnar  
▶ The volatile budget of Haleakala (Maui): New insights from melt inclusions
- 3:10 Break**
- Session Chair: Zoltán Zajacz*
- 3:30 **Megan E. NEWCOMBE**, Alexander S. Lloyd, David Ferguson, Anna Barth, Erik Hauri, Terry A. Plank  
▶ **Invited Lecture:** The melt inclusion record of the final countdown to eruptions
- 3:50 **Michael ZOLENSKY**, Queenie H.-S. Chan, Yoko Kebukawa, Robert J. Bodnar, Marc Fries  
▶ **Keynote Lecture:** Fluid inclusions in Astromaterials: Direct samples of early solar system aqueous fluids
- 4:30 **Philip E. BROWN**  
▶ 31 years of PACROFI
- 6:00-9:00 Conference Dinner**  
- **The Café at The Museum of Fine Arts**

## Thursday, June 14

### Session 4: Fluid Inclusions in Ore Deposits

*Session Chair: Julien Bourdet*

- 9:00 **Adam C. SIMON**, Jaayke Knipping, Martin Reich, Fernando Barra, Artur P. Deditius, Laura Bilenke, Tristan Childress<sup>1</sup>  
▶ **Invited Lecture:** A magmatic flotation model that genetically links iron oxide–apatite (IOA) and iron oxide–copper–gold (IOCG) deposits

\*[(**Pilar LECUMBERRI-SANCHEZ**, Christoph A. Heinrich, Markus Wälle, Marta Codeço, Phillip Weis, Marta Sośnicka, Filipe Pinto

\*▶ **Keynote Lecture:** Genetic relationship between mineral paragenesis, fluid chemistry and fluid source in a tungsten vein deposit: Panasqueira)]

9:40

**John RIDLEY**

▶ Different modes of fluid phase separation in a single hydrothermal fluid?

10:00

**Martin S. APPOLD**, Emalyn R. Glastetter

▶ Determination of sulfur concentration in fluid inclusions through SEM-EDS analysis of fluid inclusion decrepitates: Application to the Illinois-Kentucky Mississippi Valley-type district

10:20

**Wyatt M. BAIN**, Matthew Steele-MacInnis, Frank K. Mazdab, Erin Marsh

▶ Aqueous brines and carbonate melts represented by inclusions in apatite from the Buena Vista iron-oxide apatite deposit, Nevada

**10:40**

**Break**

*Session Chair: Bob Bodnar*

11:00

**Adam SIMON**

▶ Basaltic underplating and the evolution of redox gradients in systems: implications for porphyry deposits

\*[(**Pilar LECUMBERRI-SANCHEZ**, M. Bouabdellah, O. Zemri

\*▶ Fluid inclusion characteristics at the El Hammam REE-rich fluorite deposit)]

11:20

**Dan MARSHALL**, Gaston Giuliani, Lara L. Loughrey

▶ **Keynote Lecture:** Stable isotope disequilibrium in zoned emeralds precipitated from two phase fluids at chemical equilibrium?

12:00

**Discussions and Business Meeting**

12:30

**Meeting Adjourned; Field trip departs to West Texas**

## Posters

### **Presented Tuesday at the Icebreaker, then posted for the rest of the meeting in Sewall Hall 301**

Hanna L. Brooks, **Matthew STEELE-MACINNIS**

- \*▶ A new model for the solubility of common rock-forming minerals in saline aqueous fluids up to 1100 °C and 20 kbar

**Michael H. DECINDIS**, Matthew Steele-MacInnis

- \*▶ Low-temperature phase equilibria of saline aqueous systems containing carbonate, bicarbonate and other anions

**Hunter R. EDWARDS**, D. Matthew Sublett Jr., Robert J Bodnar

- ▶ An investigation of the phase behavior and composition of the surface and crust of Titan using Synthetic Fluid Inclusions combined with Raman spectroscopy

**Stephanie R. FORSTNER**, Stephen E. Laubach, András Fall

- ▶ Evolution of deformation in the Buck Mountain Fault damage zone, Cambrian Flathead Sandstone, Teton Range, WY

**Jordan JENSEN**, Paulo Coutinho, Oscar Laurent, Jon Spencer, Matthew Steele-MacInnis

- \*▶ Microthermometric and LA-ICP-MS measurements of hematite-hosted fluid inclusions reveal the temperature and composition of ore-forming fluids, Buckskin-Rawhide Mountains, western Arizona, USA

**Jan Braly KIHLE**, Jørn Harald Hurum, Lene Liebe

- ▶ Liquid hydrocarbons in intracellular mineral precipitates in the vertebrae of a Jurassic marine reptile – animal or petroleum origin?

**Sarah E. SMITH-SCHMITZ**, Martin S. Appold

- ▶ Determination of F concentrations in ore-stage MVT fluids through SEM-EDS analysis of fluid inclusion decrepitates

**Heather M. VANDERGRIFT**, Robert J. Bodnar Maxim Gavrilenko, Michael Krawczynski

- ▶ Analysis of water content in melts (silicate glass) using Raman spectroscopy

**Qiqi WANG**, Stephen E. Laubach, András Fall

- \*▶ Unraveling the history of ultra-deep fractures in sedimentary basins





# Abstracts



## Determination of sulfur concentration in fluid inclusions through SEM-EDS analysis of fluid inclusion decrepitates: Application to the Illinois-Kentucky Mississippi Valley-type district

Martin S. APPOLD, Emalyn R. GLASTETTER

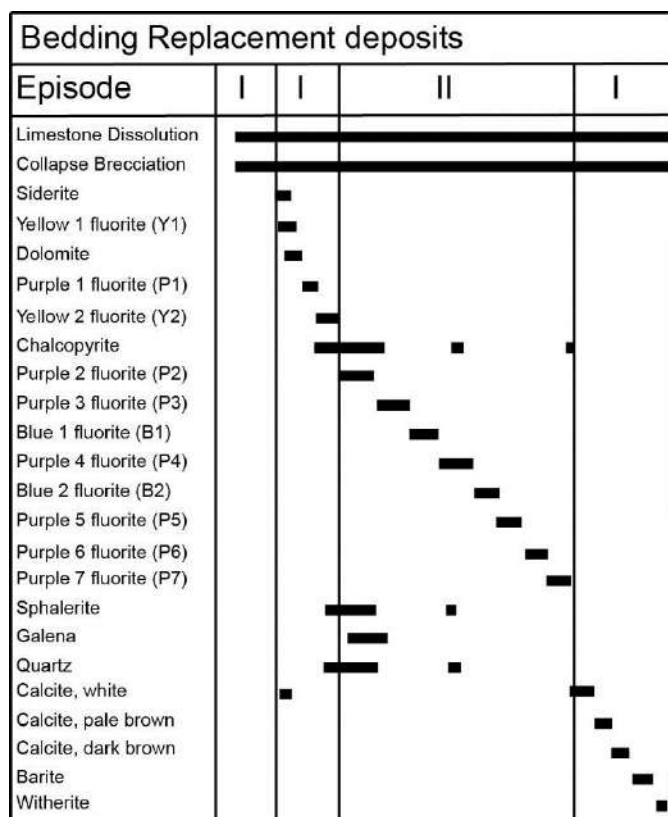
*Department of Geological Sciences, University of Missouri, Columbia, Missouri, U.S.A.*

*E-mail: appoldm@missouri.edu*

Sulfur plays a fundamental role in the precipitation of Mississippi Valley-type (MVT) ore deposits but its concentration in MVT ore fluids is not well known. In order to determine the mechanism of precipitation of base metal sulfide minerals in MVT deposits, whether anomalously sulfur-rich fluids are needed to form MVT ore deposits, and how much time is needed to form MVT ore deposits, the sulfur content of MVT ore fluids must be known.

Sulfide minerals in MVT deposits have long been considered to precipitate according to one or more of the following general precipitation mechanisms: (1) Mixing of a metal-rich, sulfide-poor fluid with a metal-poor, sulfide-rich fluid, (2) reduction of sulfate in a fluid rich in metals, (3) cooling, pH increase, or dilution of a fluid carrying both metals and sulfide at relatively low concentrations. By characterizing the spatial and temporal variation of ore fluid sulfur concentration in a MVT deposit, the operating precipitation mechanism should be identifiable. This can potentially be accomplished by determining sulfur concentration in fluid inclusions hosted by non-sulfide minerals from various locations and paragenetic stages in a MVT deposit.

The Illinois-Kentucky district is a favorable site in which to test this approach because the district contains numerous distinct stages of fluorite that precede, overlap, and post-date sulfide minerals in the paragenetic



sequence (Fig. 1). Thus, if fluid inclusions throughout the fluorite paragenesis and throughout the district were consistently found to have low sulfur concentrations, then this would suggest that base metals and sulfide were transported together in solution and precipitated due to local cooling, pH change, or dilution. Cooling and dilution are both allowed, though not definitely identified, by previously published microthermometry data (Pelch et al., 2015 and references therein). If both high-sulfur and low-sulfur populations of fluid inclusions were found, then this would point to either the mixing or sulfate reduction precipitation mechanisms. These two precipitation mechanisms could be distinguished from one another by using Raman spectroscopy to determine whether the sulfur was in the form of sulfate or sulfide.

**Figure 1.** Paragenetic sequence of bedding replacement MVT mineralization in the Illinois-Kentucky district (after Richardson and Pinckney, 1984 and Hall and Friedman, 1963).

Sulfur is an element whose concentration is difficult to quantify reliably using LA-ICP-MS, a technique that has been used successfully for in situ measurement of concentration of many other elements in fluid inclusions. However, SEM-EDS analysis of evaporative solute mounds formed by fluid inclusion decrepitation is a promising alternative for measuring sulfur and has begun to be used in the present study. In order to calibrate the SEM-EDS signal, six standard ore solutions were prepared to allow actual sulfur concentrations in fluid inclusions to be determined from sulfur concentrations in evaporative solute mounds measured by SEM-EDS. These standard solutions contain known concentrations of sulfur of 10, 50, 100, 500, 1000, and 5000 ppm, and the major element (Na, Ca, K, Mg, Cl) composition of the Illinois-Kentucky ore fluid inclusions based on the LA-ICP-MS study of Pelch et al. (2015). Droplets of standard solutions were placed onto clean polished fluorite samples and allowed to evaporate, generating solute mounds. Solute mounds were analyzed using SEM-EDS under the same conditions used for the natural samples, creating a calibration relationship that allowed for the S/Cl ratio in the fluid inclusions from natural samples to be calculated from the measured S/Cl ratio of standard ore solutions. Compositional analysis of evaporative solute mounds is being carried out using a Sigma 500 VP SEM in the Department of Geological Sciences at the University of Missouri—Columbia. Tests so far show the detection limit for sulfur in fluid inclusions to be between 10 and 50 ppm.

To date, fluid inclusions from two early fluorite stages (P1 and Y2 fluorite) from the Cave-in-Rock subdistrict have been analyzed. Fluid inclusion sulfur concentration in P1 fluorite was found to be about 40 ppm and in Y2 fluorite to be about 110 ppm. These sulfur concentrations lie within the range typical of sedimentary brines (Hanor, 1998). Over the pH range of 4 to 5.5 typical of MVT ore-forming brines, these sulfur concentrations, if in the form of sulfide, could coexist in solution with up to 10's of ppm Zn. Thus, a regional sedimentary brine that delivered sulfur and base metals to the Illinois-Kentucky district would have been a relatively fertile ore fluid. However, work by Kenderes and Appold (2017) suggests that sulfide mineralization in the Illinois-Kentucky district formed at very low pH values between 0 and 1, based on the high F concentration in sphalerite-hosted fluid inclusions, though these low pH values would have been localized to sites where magmatic HF was being titrated into the regional sedimentary brine system via faults. One way to overcome the greatly increased solubility of sulfide minerals at such low pH is to increase the concentration of aqueous sulfide in the ore fluid. This is a hypothesis that will be tested in future work by analyzing fluid inclusions from later fluorite stages that paragenetically overlap sulfide minerals.

#### REFERENCES

- Hall W. E. and Friedman I. (1963) Composition of fluid inclusions, Cave-in-Rock fluorite district, Illinois, and Upper Mississippi Valley zinc-lead district: *Economic Geology* 58, 886–911.
- Hanor, J. S. (1998) Geochemistry and origin of metal-rich brines in sedimentary basins, in, Pongratz, J. and McGoldrick, P. (eds.) *Basins, fluids and Zn-Pb ores*: University of Tasmania, Centre for Ore Deposit Research (CODES), Special Publication 2.
- Kenderes, S. M., Appold, M. S. (2017) Fluorine concentrations of ore fluids in the Illinois-Kentucky district: Evidence from SEM-EDS analyses of fluid inclusion decrepitates: *Geochimica et Cosmochimica Acta* 210, 132-151.
- Pelch, M. A., Appold, M. S., Emsbo, P., Bodnar, R. J. (2015) Constraints from fluid inclusion compositions on the origin of Mississippi Valley-type mineralization in the Illinois-Kentucky district: *Economic Geology* 110, 787–808.
- Richardson, C. K. and Pinckney, D. M. (1984) The chemical and thermal evolution of the fluids in the Cave-in-Rock fluorspar district, Illinois: mineralogy, paragenesis, and fluid inclusions: *Economic Geology* 79, 1833–1856.

## Aqueous brines and carbonate melts represented by Inclusions in apatite from the Buena Vista iron-oxide apatite deposit, Nevada

Wyatt M. BAIN<sup>1</sup>, Matthew STEELE-MACINNIS<sup>1</sup>, Frank K. MAZDAB<sup>2</sup>, Erin MARSH<sup>3</sup>

<sup>1</sup>Department of Earth & Atmospheric Sciences, University of Alberta, Edmonton, Alberta, Canada

<sup>2</sup>Department of Geosciences, University of Arizona, Tucson, Arizona, U.S.A.

<sup>3</sup>U.S. Geologic Survey, Denver, Colorado, U.S.A.

Email: [wbain@ualberta.ca](mailto:wbain@ualberta.ca)

Genetic models for iron-oxide-apatite (IOA) deposits span a spectrum between magmatic and hydrothermal end members. Magmatic models typically involve the immiscible formation of an Fe-oxide phosphate magma from a silicate melt of felsic to intermediate (or, less commonly, mafic) affinity (Nyström and Henriquez, 1994) and subsequent formation of voluminous Ca-Na alteration by hydrothermal fluids of magmatic or basinal origin (Tornos et al., 2017; Harlov et al., 2016; Westhues et al., 2016; Chen et al. 2010). In contrast, hydrothermal models of IOA formation involve the formation of Ca-Na alteration and Fe mobilization by hydrothermal fluids of magmatic, basinal, or metamorphic origin which have equilibrated with Fe-rich magmas or leached Fe from country rocks (Johnson and Barton, 2000; Hunt et al., 2007; Richards and Mumin, 2013).

The Buena Vista deposit (Pershing County, Nevada) has been reported as an example of hydrothermal IOA mineralization. This IOA deposit is associated with gabbros which intruded late-Triassic to early-Jurassic basalts, carbonates, and evaporites during mid-Jurassic back-arc extension. Johnson and Barton (2000) interpreted the IOA mineralization in this deposit as being related to amagmatic fluids of basinal affinity. This interpretation is based on cross-cutting relationships between ores and altered lithologies, petrographic observation of brine-rich fluid inclusions, and mass-balance constraints between altered rocks and magnetite ores.

Here we present petrographic observations, microthermometry, Raman analyses, EDS maps, and laser ablation ICPMS data from apatite and clinocllore-hosted fluid inclusions from massive magnetite (+apatite) ore (magnetite ore) and carbonate (+apatite) vein (carbonate veins) assemblages in the Buena Vista deposit. Magnetite ore and carbonate vein assemblages host abundant aqueous brines which form coeval assemblages with polycrystalline inclusions composed of carbonate (calcite or siderite), Fe- and Ti-oxides, and variable amounts of Si- and Al- rich phases ( $\pm$  H<sub>2</sub>O) (Figure 1). Primary and secondary aqueous inclusions from magnetite ores and carbonate veins are primarily halite-bearing, show consistent microthermometric behavior (first ice melting observed from -60 to -45°C, vapor dissolution from 90 to 140°C, and homogenization by halite melting at ~245-285°C) and have salinities from 36-38 wt% NaCl equivalent. During heating, polycrystalline inclusions showed onset of melting at ~400°C and were mostly molten at ~800°C. Residual phases present above 850°C did not appear to melt with further heating and included red or opaque granules, which were interpreted as hematite plus an unidentified translucent phase.

Laser ablation ICPMS analysis showed that aqueous brine inclusions are dominated by Na-K-Ca, similar to fluids reported in other IOA environments. Brines associated with the magnetite ores are strongly depleted in Fe and K and are compositionally similar to basinal fluids (Yardley, 2005), while brines associated with carbonate veins are relatively enriched in K, Fe, and B, suggesting a magmatic affinity. Polycrystalline inclusions contain abundant Fe, Al, and Mg, with lesser K, Ti, V, Mn, and Cu. This correlates well with EDS maps which show discrete Fe, Al, and Ti phases in breached polycrystalline inclusions. In addition, ICPMS analysis showed that major element ratios within temporally related inclusion groups show little variability and have not been altered by post-entrapment water loss or ion diffusion.

Coeval assemblages of polycrystalline inclusions and aqueous brines, such as those reported in porphyry systems, are commonly interpreted to represent the coexistence of immiscible fluid phases (melt and aqueous fluid). Similarly, the coexistence of brine and carbonate-dominated polycrystalline inclusions in the Buena Vista system indicates that an aqueous brine and a carbonate liquid coexisted immiscibly during the formation of magnetite ores and carbonate veins. The primary implication of these results is therefore that Buena Vista – previously interpreted as a hydrothermal end-member of IOA formation – is actually a hybrid magmatic-hydrothermal system wherein carbonate melts coexisted with aqueous brines. Furthermore, data presented here indicate that Fe, Al and other

nominally insoluble elements were partitioned into the carbonate liquid rather than the coexisting brine. This suggests that the carbonate liquid might have played an important role in promoting element mobility during the formation of both the magnetite-apatite and carbonate-vein assemblages.

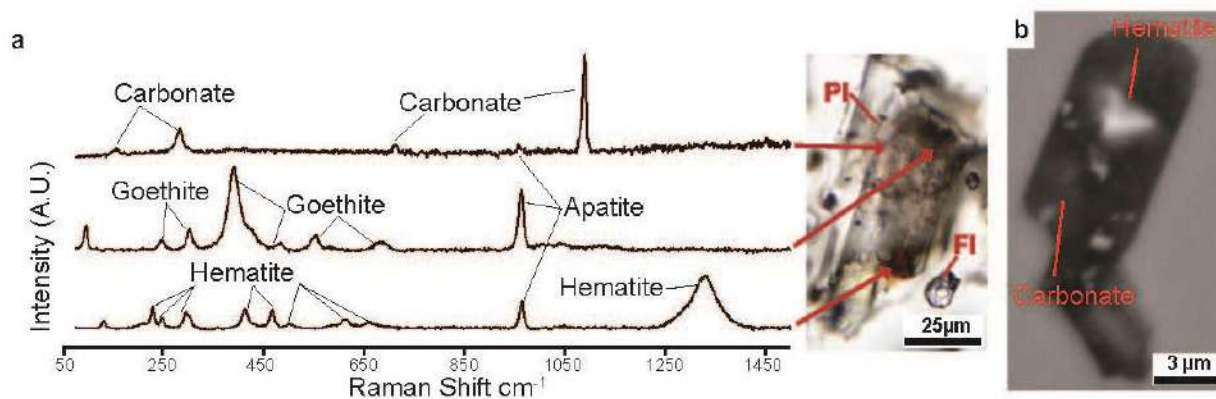


**Figure 1.** a) Raman spectra for carbonate and Fe-oxides from an apatite-hosted polycrystalline inclusion (PI) shown in the corresponding photomicrograph. Note the coexisting brine fluid inclusion (FI) in the bottom right side of the photomicrograph. b) Backscatter electron image of a breached polycrystalline inclusion showing a hematite crystal and carbonate adhered to the margins of the inclusion.

#### REFERENCES

- Chen, H. et al. (2010) The Marcona magnetite deposit, Ica, south-central Peru: A product of hydrous, iron oxide-rich melts? *Econ. Geol.* 105, 1441-1456.
- Harlov, D.E. (2016) Mineralogy, chemistry, and fluid-aided evolution of the Pea Ridge Fe oxide-(Y+REE) deposit, Southeast Missouri, USA, *Econ. Geol.* 111, 1963-1984.
- Hunt, J.A. et al. (2007) A review of iron oxide copper-gold deposits, with focus on the Wernecke breccias, Yukon, Canada, as an example of a non-magmatic end member and implications for IOCG genesis and classification, *Exp and Mining Geol.* 16, 209-232.
- Johnson, D.A., Barton, M.D. (2000) Time-space development of an external brine-dominated, igneous-driven hydrothermal system; Humboldt mafic complex, western Nevada. *Soc of Econ Geol Guidebook Series.* 32, 127-144
- Nyström, J.O., Henriquez, F. (1994) Magmatic features of iron ores of the Kiruna type in Chile and Sweden: Ore textures and magnetite geochemistry, *Econ. Geol.* 89, 820-839.
- Richards, J.P., Mumin, A.H. (2013) Magmatic-hydrothermal processes within an evolving Earth: Iron oxide-copper-gold and porphyry Cu Mo Au deposits, *Geology.* 41, 767-770.
- Tornos, F. et al. (2017) The magmatic to magmatic-hydrothermal evolution of the El Laco deposit (Chile) and its implications for the genesis of magnetite-apatite deposits, *Econ. Geol.* 112, 1595-1628
- Westhues, A. et al. (2016) New Constraints on the timing of host-rock emplacement, hydrothermal alteration and iron oxide-apatite mineralization in the Kiruna district, Norrbotten, Sweden, *Econ. Geol.* 111, 1595-1618
- Yardley, B.W. (2005) Metal concentrations in crustal fluids and their relationship to ore formation, *Econ. Geol.* 100, 613-632.

## Geochemistry alive: How natural fluid inclusions and capillary reactors help unravel sulfur reactivity during Thermochemical Sulfate Reduction

Guillaume BARRÉ<sup>1</sup>, Raymond MICHELS<sup>1</sup>, Laurent TRUCHE<sup>2</sup>, Valérie BURKLÉ-VITZTHUM<sup>3</sup>, Catherine LORGEUX<sup>1</sup>

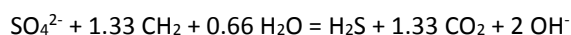
<sup>1</sup>GeoRessources Lab, CNRS, Université de Lorraine, Nancy, France

<sup>2</sup>ISTerre, Grenoble, France

<sup>3</sup>LRGP CNRS, ENSIC, Université de Lorraine, France

E-mail: raymond.michels@univ-lorraine.fr

Sulfur chemistry plays an important role in geochemical processes. Indeed, depending on physico-chemical conditions the various oxidations states of sulfur (from S<sup>-II</sup> to S<sup>+VI</sup>) lead to great variety of minerals, aqueous species as well as organic compounds. Sulfur chemistry is thus implied in major geological cycles and involved in the formation of ore and evolution of hydrocarbons deposits. Among the many possible chemical reactions, thermochemical sulfate reduction (TSR) has attracted specific attention. A general reaction for TSR may be written as:



This process implies mineral as well as organic matter and triggers complex reaction mechanisms in both the aqueous and the organic phases.

A major difficulty to study TSR in natural fluids is to collect solid, aqueous, organic, gaseous phases in equilibrium at geological pressure-temperature. This is why TSR is seldom studied in situ of geological settings. Laboratory experimentation is thus the most common approach and most published data deal with post-experimentation fluid compositions. The actual sulfur reactivity and speciation within natural fluid compositions and at geological temperature and pressure is therefore not commonly investigated.

In order to study organic-mineral reactivity during TSR and understand the chemical mechanisms involved, we developed a strategy using natural fluid inclusions, capillary reactors as well as gold cell reactors. Natural fluid inclusions were collected in the French Alps (evaporites deposits of the Carnian “Nappe des Gypses” formation located in the Arc Valley). Experiments of TSR were conducted in capillary reactors while sulfur reactivity in the organic phase was studied using gold cell reactors as to complete geochemical information. Analyses were performed by Raman spectroscopy, FTIR, GC-MS. Objective was to document as precisely as possible the speciation and reactive pathways of sulfur in the aqueous, gaseous and organic phases.

Natural fluid inclusions from the “Nappe des Gypses” formation hosted in quartz, albite, fluorite revealed the presence of a two liquid-gas system composed of NaCl, CaCl<sub>2</sub>, SO<sub>4</sub><sup>2-</sup>, S<sub>8</sub>, H<sub>2</sub>S, CO<sub>2</sub>, N<sub>2</sub>±CH<sub>4</sub>, traces of hydrocarbons with sometimes the presence of solids (native sulfur and halite). Salinities range from 26 to 60 wt% eq NaCl with a mean at 31wt%eq NaCl. Homogenization temperatures range from 98°C to 355°C depending on their trapping conditions during the Alpine exhumation.

The study of sulfur speciation within the fluid inclusions at 25°C reveals mainly the presence of SO<sub>4</sub><sup>2-</sup> as well as S<sub>8</sub> in the aqueous phase and H<sub>2</sub>S in the gas phase. The study under progressive heating above 100°C evidenced the presence of significant amounts of the metastable S<sub>3</sub><sup>-</sup> radical ion species in the aqueous phase within a fluid at typical P-T conditions of TSR. While this species had been identified in previous experimental work this is the first evidence of the importance of this radical ion in a natural geological fluid.

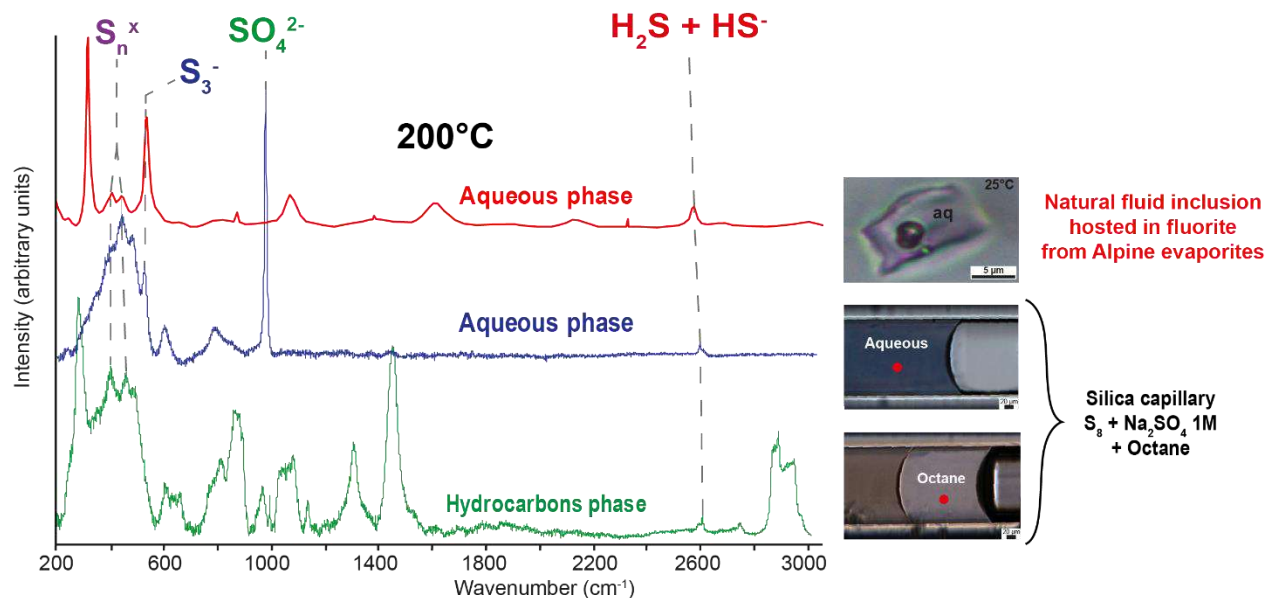


**Figure 1.** Red spectrum: First detection of the  $S_3^-$  radical ion in the aqueous phase of natural fluid inclusions hosting TSR reactants and products. Blue and green spectra: study of sulfur speciation partitioned between aqueous and organic phases during TSR experimentation in silica capillary reactor.

Silica capillary reactors were loaded with either  $S_8 + Na_2SO_4$  or  $Na_2S_2O_3$  aqueous solution in the presence of octane and heated at temperatures ranging between 200 and 350°C. Estimated pressure was about 200 bars. Each phase present in the capillary was monitored using Raman and FTIR as to identify reacting species. During heating,  $S_8$  is in equilibrium between octane and aqueous phase until all is disproportionated into  $SO_4^{2-}$  and  $H_2S$ .  $H_2S$  as reaction product was detected in water, octane and gas. The  $S_3^-$  radical was detected in the aqueous phase only and quantified.

The detection of polysulfides as well as the  $S_3^-$  radical ion at significant concentrations during heating in the aqueous phase is strong evidence of the role of sulfur at intermediate valence during TSR. Yet,  $S_3^-$  was not detected in the octane phase. In order to identify octane sulfurization reactions in the organic phase, we conducted pyrolysis studies of octane in the presence of  $H_2S$  (the most abundant sulfur species detected in the organic phase) using gold cell reactors. Post-run analysis allowed to identify the formation of sulfur bearing hydrocarbon species. These results lead to propose reaction mechanisms of formation specific to the organic phase.

While the study of alpine fluid inclusions evidenced the importance of the  $S_3^-$  radical ion in the TSR reaction of natural geological fluids at specific P-T conditions, the use of capillary reactors allowed to investigate the 3 phases water-hydrocarbon-gas system during heating. The nature, concentration and phase distribution of chemical species could therefore be constrained. Specific study of the reactivity of the octane phase in the presence of  $H_2S$  brought an independent view on the organic reactivity. Main conclusions from our work show that sulfur reactivity during TSR necessitates to investigate the aqueous, hydrocarbon and gas phases during experimentation in which the nature and distribution of major reacting species may be monitored. Specific reaction pathways have been identified in the aqueous and hydrocarbon phases which involved different reaction mechanisms with specific sulfur species. Efforts still need to be developed as to conceal the reaction formalisms as to describe the reactivity of the whole system and eventually access kinetic modeling.

## Fluid inclusion tools in petroleum systems analysis

Stephen P. BECKER

ExxonMobil Upstream Research Company, Houston, Texas, U.S.A.

E-mail: stephen.becker@exxonmobil.com

A petroleum system is a linked group of play elements comprising a mature source rock, migration pathway, reservoir, trap, seal, and the temporal and spatial distribution of these elements that allow for the accumulation of hydrocarbons in the subsurface (Magoon and Dow, 1994). Successful exploration for economic quantities of hydrocarbons requires adequate understanding of the risk that one or more of these play elements is insufficient and/or mistimed. As such, we dedicate significant effort, both pre- and post-drill to de-risk play elements based on available data and/or conceptual models, which are integrated to make business decisions on acreage acquisition and/or future well location.

Because fluid inclusions provide a unique opportunity to study the composition and distribution of fresh, uncontaminated hydrocarbons in a petroleum system over time, they are an important tool we use to help de-risk hydrocarbon systems. At ExxonMobil, we employ a workflow that begins with rapid and cheap screening of samples for the likely presence of hydrocarbon inclusions beginning with the Fluid Inclusion Volatiles (FIV) mass spectrometry technique. More than simply telling us that hydrocarbons inclusions are or aren't present in any given sample, we screen cuttings and/or core in depth profile to produce a pseudo-well log of paleo-hydrocarbon migration and relative sealing capacity (Fig. 1). Generally, we observe that intensity of FIV response scales with robustness of a hydrocarbon system, and distribution of hydrocarbon components that directionally scales with hydrocarbon composition.

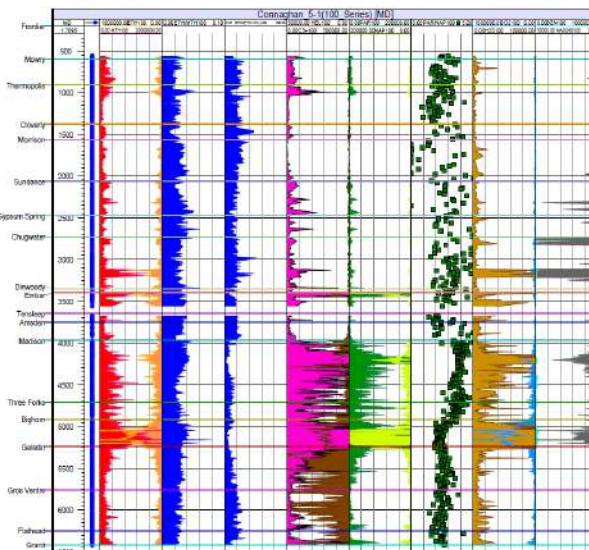


**Figure 1.** Fluid Inclusion Volatiles data, Conaghan 5-1 well, Oregon Basin field, Bighorn Basin, Wyoming

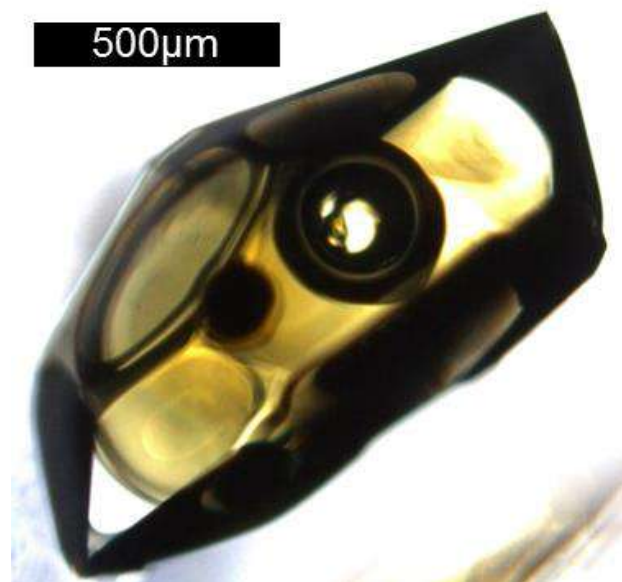


**Figure 2.** Oil inclusion in quartz, Belochistan, Pakistan

Beyond the FIV technique, we often proceed with optical fluid inclusion petrography and microthermometry to identify fluid inclusion assemblages (Goldstein and Reynolds, 1994) that are relevant to the types of problems we want to solve. In a “dry” hole, did hydrocarbons ever move through these rocks? What is the likelihood of oil vs. gas? What was the maximum burial temperature? What is the composition of hydrocarbons? Has the composition changed over time? Is it possible that hydrocarbons have been significantly altered?

Towards answering compositional questions, we maintain the ability to conduct microanalysis of the PVTX properties of hydrocarbon inclusions (Fig. 2). This includes spectroscopic methods such as fluorescence and/or Raman, and confocal laser scanning microscopy

(e.g. Aplin et al., 1999; Tseng and Pottorf, 2002). Ultimately, in characterizing the composition and phase behavior of hydrocarbon inclusions, we can place this in a relative timing framework from the petrography, and then constrain absolute timing with a calibrated basin model.

Compared to academic studies, our workflow isn't fundamentally that different from how typical fluid inclusion studies are conducted. However, the short scale of time and large scale of money involved in petroleum exploration necessitates rigorous QA/QC and fact-based interpretation of our data, and also integrate with many independent indicators of petroleum systems play element risk.

#### REFERENCES

- Aplin, A.C., Macleod, G., Larter, S.R., Pedersen, K.S., Sorensen, H., and Booth, T. (1999) Combined use of Confocal Laser Scanning Microscopy and PVT simulation for estimating the composition and physical properties of petroleum in fluid inclusions, *Marine and Petroleum Geology*, 16, 97-110.
- Goldstein, R.H. and Reynolds, T.J. (1994) Systematics of fluid inclusions in diagenetic minerals, *SEPM Short Course* 31, 199p.
- Magoon, L.B. and Down, W.G. (1994) *The Petroleum System – From Source to Trap*, AAPG Memoir 60, 665p.
- Tseng, H. and Pottorf, R.J. (2002) Fluid inclusion constraints on petroleum PVT and compositional history of the Greater Alwyn—South Brent petroleum system, northern North Sea, *Marine and Petroleum Geology*, 19, 797-809.

## Invited – Investigation of the monophasic water inclusions in quartz cement: An example from the Triassic Lesueur Sandstone aquifer, Perth Basin, Australia

Julien BOURDET<sup>1</sup>, Claudio DELLE PIANE<sup>1</sup>, Chen QIU<sup>2</sup>, Martin FRENZ<sup>2</sup>

<sup>1</sup>CSIRO Energy, Bentley, Western Australia, Australia

<sup>2</sup>Institute of Applied Physics, University of Bern, Bern, Switzerland

E-mail: Julien.Bourdet@csiro.au

The Middle to Late Triassic Lesueur Sandstone in the southern part of the Perth Basin, Western Australia, is constituted by fluvial to shallow marine siliciclastic units currently being evaluated as a possible target for geosequestration of CO<sub>2</sub>. The Lesueur Sandstone can be differentiated into a 700m thick sand, siltstone and claystone unit, the Yalgorup Mbr (Upper Lesueur) and a 1500 m thick sandstone dominated unit, the Wonnerup Member (Lower Lesueur). The CO<sub>2</sub> containment strategy relies on dissolution and residual trapping mechanisms within the Lesueur Sandstone as the primary mechanism and the effectiveness of the Yalgorup Mbr and overlying Eneabba Formation (Lower Jurassic) to act as a secondary barrier for mobile CO<sub>2</sub> (Stalker et al., 2013).

The upper section of the Wonnerup Mbr is dominated by quartzo-feldspathic sandstones showing good reservoir quality and permeability. Petrographic analysis of deeper section indicate a significant effect of diagenesis on reservoir quality. Porosity and permeability are strongly reduced with increasing depth via precipitation of pore occluding clay minerals and deposition of quartz overgrowth. Understanding the quartz cementation mechanism in different part of the reservoir unit is critical for injection, storage capacity and plume movement prediction in this semi-open aquifer. Moreover, an exhumation of the area of at least 1 km has been evaluated based on wireline logging sonic transit time-depth trends analysed across the basin (Olierook and Timms, 2016). The fluid inclusion data in quartz overgrowths are also expected to improve the understanding of the burial history of the formations. To this end, quartz cementation was investigated using petrographic and fluid inclusions techniques in sandstone samples from both the Wonnerup and the Yalgorup Mbrs, from four wells (Harvey-1, Harvey-2, Harvey-3 and Harvey-4) located on the structural high known as the Harvey Ridge and one well (Pinjarra-1) located 40 km north where the Lesueur Sandstone is deeply buried.

Initial observations indicated that in many cases, the water inclusions trapped in quartz cements were monophasic at room temperature (Figure 1) and even cooling treatments failed to nucleate bubbles in order to derive temperature using microthermometric methods. Therefore, an amplified femtosecond laser system (Coherent) at University of Bern (Switzerland) was used to stimulate vapour bubble nucleation in the metastable liquid state of the inclusions by means of single ultrashort laser pulses allowing for measurements of homogenisation temperatures. For a detailed description of the setup we refer to Krüger et al. (2007). The samples from Pinjarra-1 were not investigated using this technique. Salinities were measured using Raman spectroscopy technique. No dissolved gas was detected using Raman spectroscopy, dissolved in the water or in the bubble of a limited number of inclusions.

Homogenisation temperatures ( $T_H$ ) of 39°C to 115°C were measured in samples from Harvey 1-4. Temperature histograms for the samples from the Yalgorup and the Wonnerup Mbrs are presented in Figure 2. The histograms are skewed toward higher temperature commensurate with sample depth. The shallowest samples indicate, after pressure correction, that the quartz cementation process

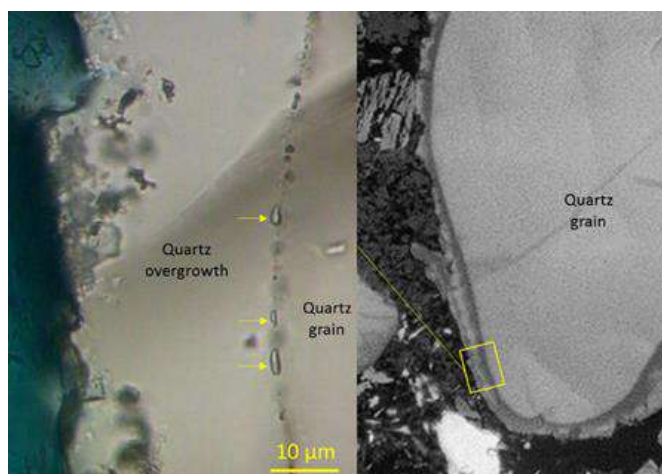


**Figure 1.** Monophasic water inclusions at quartz-overgrowth boundary from a sandstone sample. Harvey-2 well at 1245.15 mRT.

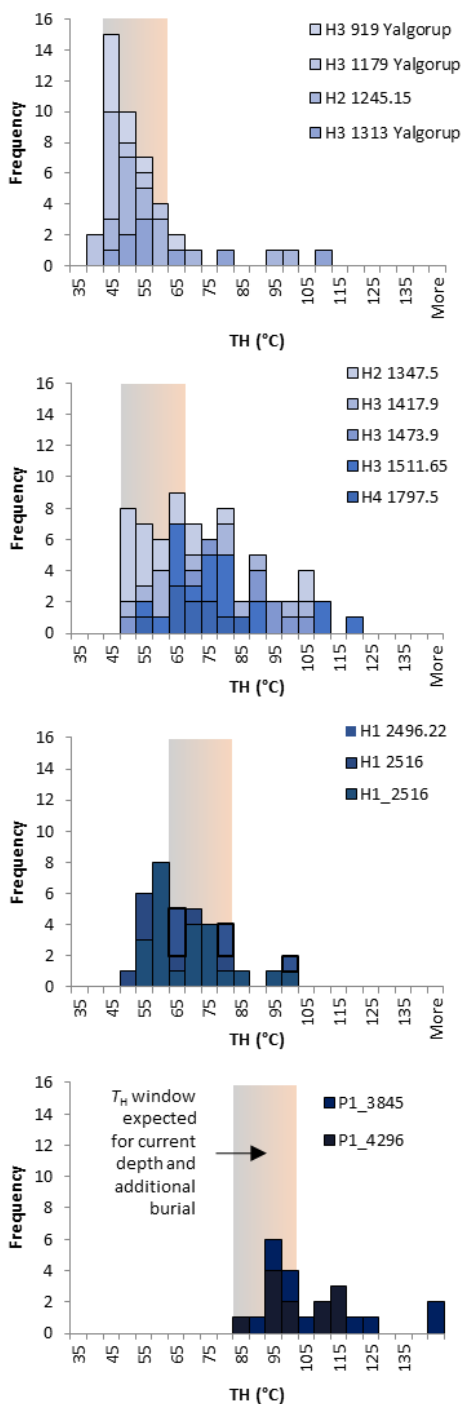


**Figure 2.**  $T_H$  histograms of water inclusion in quartz cements in sandstone from shallow to deep samples from Harvey-1, 2, 3, 4 and Pinjarra-1. The  $T_H$  window is calculated assuming  $H_2O-NaCl$  fluid devoid of dissolved gas.

started below 50°C. The deeper samples present higher minimum temperatures. In the deep samples from Pinjarra-1, where monophasic water inclusions were not detected or investigated carefully, those low temperatures are absent of the histogram. Assuming that quartz cementation started for all samples at a fixed temperature of about 50°C and continued with burial, these results suggest that the lowest  $T_H$  water inclusions re-equilibrated with increasing temperature during burial. The resulting fluid inclusion dataset can then not be used for deriving the temperature of initiation of quartz cementation.

Figure 2 shows temperature windows of expected  $T_H$  for water inclusion entrapment at current sample depths and with an additional burial of 1200 m. The  $T_H$  lower than this interval indicate cementation at shallower depth. Most  $T_H$  values can be reconciled with this uplift history. The minimum  $T_H$  value in each cases seems to carry a geological meaning, either in term of initiation of quartz cementation (shallow samples) or equilibrium to current conditions (deep samples). However, most samples have some water inclusions with higher  $T_H$  values. These water inclusions can either have been generated by overheating and stretching low  $T_H$  inclusions, or they can be a marker of fast fluid circulation from deeper fluids, facilitated by deformation and faulting episode.

Salinities ranged between <5,000 ppm to 70,000ppm with a bimodal histogram at 15,000-25,000 ppm and 35,000-45,000 ppm. The salinity values are consistent with the formation water being derived from connate water in fluvial to shallow marine paleo-environments. A  $T_H$  versus salinity cross-plot shows that most of the data generated can be contained in a restricted interval of temperature and salinity. The anomalous high  $T_H$  values appear as a broad cluster of data points outside this restricted interval, sitting at higher temperature values. This cluster does not show trends and therefore does not seem to be consistent with a deep fluid source. These fluid inclusions are likely to have been generated by overheating and stretching low  $T_H$  inclusions.

Overall, the use of femto-second laser system to stimulate vapour bubble nucleation in monophasic inclusions allowing for the measurements of their homogenisation temperatures revealed to be successful. It also provided clues about how to interpret fluid inclusion data for understanding quartz cementation and burial history.

REFERENCES

Krüger, Y. et al. (2007) Femtosecond lasers in fluid-inclusion analysis: overcoming metastable phase states. *European Journal of Mineralogy*, 19(5), 693-706.  
 Olierook, H.K.H., Timms N.E. (2016) Quantifying multiple Permian-Recent exhumation events during the break-up of eastern Gondwana: Sonic transit time analysis of the central and southern Perth Basin. *Basin Research* 28, 796-826.  
 Stalker, L. et al. (2013) SouthWest Hub: a carbon capture and storage project. *Aust. J. Earth Sci.* 60, 45-58.

## Attributes of petroleum inclusion assemblages for unravelling charge history

Julien BOURDET, Richard KEMPTON

CSIRO Energy, Bentley, Western Australia, Australia

E-mail: Julien.Bourdet@csiro.au

A diversity of fluid inclusion techniques are established in the petroleum industry that involve measuring their abundance, fluorescence, PVT properties and geochemistry to constrain the state of the fluid, its composition, density, trapping temperature and pressure or gas saturation. This contributes to understanding basin-scale migration-accumulation processes. Because they trap paleo fluids fluid inclusions offer unique insights into the filling of petroleum reservoirs. There is untapped potential for expanding the range of techniques or new interpretations

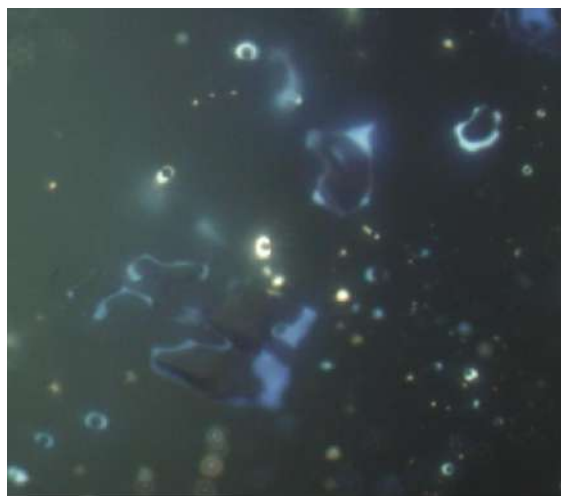


**Figure 1:** Example of oil inclusion assemblage trapped at the quartz overgrowth boundary. This assemblage presents variability of the attributes such as the vapor-phase size and of the fluorescence color of the oil. It results from the heterogeneous trapping of a residual oil and gas in a gas zone within a same oil inclusion assemblage.

of fluid inclusion data to make them more widely applied. Fluid inclusion techniques are a small part of the large data sets used in petroleum exploration and to be accepted the interpretations must be precise and accurate.

The GOI™ (Grains containing Oil Inclusions) technique (Eadington et al., 1996) is used widely to detect paleo-oil zone or evidence for oil migration in currently oil-, gas- or water- saturated reservoirs. A difference between the depth and or attitude of fluid contacts is revealing of processes that operate during the preservation time of oil in reservoirs including displacement of oil by gas and leakage of oil through the seal (Lisk and Eadington, 1994; Lisk et al., 1997; Kempton et al., 2011). In addition to documenting the abundance of oil inclusions the GOI workflow documents selected attributes of oil inclusion assemblages (Figure 1) such as the petrographic superposition sequence, variance in the proportion of vapor, variability of the fluorescence color of the oil, in datasets that reveal correlation and covariance between attributes that are useful for interpretation.

More recently, petrographic, experimental and spectroscopic studies of the attributes of oil inclusion assemblages (Bourdet et al., 2012, 2014) demonstrated some of the variance in the appearance of oil inclusion assemblages is a consequence of in-reservoir fluid interactions. The known but controversial empirical relationship between UV-fluorescence colors of oil with its composition was used to calculate equations to derive the degree API of the oil as well of their saturates-aromatics-resins-asphaltene fractions. FT-IR spectra were used to measure and assess the variability of the CH<sub>2</sub>/CH<sub>3</sub> ratio and methane content in different zones of a reservoir. Experiments were conducted in silica capillary capsules to reproduce some of the natural variance due to interaction of residual oil with gas.

These attribute and spectroscopic data show that in-reservoir fluid interactions contribute significant variance in the appearance of oil inclusion assemblages. It is necessary to separate the in-reservoir fluid interactions from

those due to generation-migration processes to enable accurate understanding of petroleum systems at the basin scale.

#### REFERENCES

- Bourdet, J. et al. (2014) Evidence for a paleo-oil column and alteration of residual oil in a gas-condensate field: integrated oil inclusion and experimental results, *Geochimica et Cosmochimica Acta*, 142, pp. 362-385.
- Bourdet, J. et al. (2012) Chemical changes of fluid inclusion oil trapped during the evolution of an oil reservoir: Jabiru-1A case study (Timor Sea, Australia). *Marine and Petroleum Geology*, 36, 118-139.
- Eadington, P.J. et al. (1996). Identifying oil well sites. United States Patent No. 5543616.
- Lisk, M., Eadington, P.J. (1994) Oil migration in the Cartier Trough, Vulcan Sub-basin. In P. G. Purcell, & R. R. Purcell (Eds.), *The Sedimentary Basins of Western Australia*. Perth, WA: Proceedings of the Petroleum Exploration Society of Australia, pp. 301–312.
- Lisk, M. et al. (1997) Gas displacement: an important control on oil and gas distribution in the Timor Sea? *The Australian Petroleum Production and Exploration Association Journal* 37, 259–271.
- Kempton, R.H. et al. (2011) Detection of Paleo-Oil Columns in the offshore northern Perth Basin: Extension of the effective Permo-Triassic Charge System. *The APPEA Journal* 51, 377–396.

## A new model for the solubility of common rock-forming minerals in saline aqueous fluids up to 1100 °C and 20 kbar

Hanna L. BROOKS, Matthew STEELE-MACINNIS

University of Alberta, Dept. of Earth and Atmospheric Sciences, Edmonton, Alberta, Canada

E-mail: steelema@ualberta.ca

Quantifying and predicting the dissolution of minerals in complex (multicomponent) aqueous fluids across wide ranges of  $P$ - $T$  space is critical for interpreting geologic processes that involve water-rock interactions in the Earth's crust and upper mantle. Transport of heat and materials as well as chemical reactions in geologic systems are driven and controlled by fluids. Natural geologic fluids are commonly rich in non-electrolyte (e.g.  $\text{CO}_2$ ,  $\text{CH}_4$ ,  $\text{N}_2$ ), and electrolyte solutes (e.g.  $\text{Na}^+$ ,  $\text{K}^+$ ,  $\text{Fe}^{2+}$ ,  $\text{Cl}^-$ ) (Galvez et al., 2015). High salinities strongly affect activity-composition relationships in thermodynamic modeling, and mixing high salt contents with gas-rich fluids (i.e., containing  $\text{CO}_2$  and other volatiles) expands the pressure-temperature limits of fluid phase immiscibility (Bowers and Helgeson, 1983) which partitions solutes and affects mineral stability relations. Here, we define a new thermodynamic model for mineral solubility in saline aqueous fluids. The model is based on the coupling of two previous models: one for the solubility of minerals in pure  $\text{H}_2\text{O}$  fluids as function of temperature and pressure (Dolejš and Manning, 2010), with the additional effects of fluid composition (salinity) modeled in part based on Akinfiiev and Diamond (2009), with some additional modifications.

Specifically, the new model adopts the approach of Akinfiiev and Diamond (2009) to incorporate the effect of reduced  $\text{H}_2\text{O}$  activity in saline brines for reactions that involve hydration, and also adds new expressions for the equilibrium constants of reactions involving explicit sodium and/or chloride species. As such, the generic model is applicable to the solubility of minerals that dissolve as hydrous species, sodium and/or chloride species, and combinations thereof. The model has been calibrated against experimentally determined solubilities for six common rock-forming minerals – quartz, calcite, corundum, fluorapatite, fluorite, and rutile – in  $\text{H}_2\text{O}$ - $\text{NaCl}$  solutions at temperatures up to 1100 °C and pressures up to 20 kbar. Data and trends observed in experimental measurements are well reproduced by our model predictions. In the case of pure  $\text{H}_2\text{O}$  fluids (zero salinity), the model is implicitly equivalent to the Dolejš and Manning (2010) model. The accuracy of the model is within both experimental uncertainties and accuracy ranges of the two models on which it is built.

Examining solubility ( $T$ - $x$ ) diagrams for each mineral show that, in general, increasing salinity, temperature, and/or pressure in the system leads to a corresponding increase in solubility (i.e. Figure 1). However, in-depth examination of these diagrams illustrates that the effect is dependent on temperature, pressure, the formation of solutes, and the electrostatic behavior of the solution (i.e. salting-in and salting-out).

Which of these variables dominates varies as a function of mineral properties and  $P$ - $T$ - $x$  conditions. Coupling multiple mineral solubility curves together allowed examination of the potential impact of an aqueous fluid at specific  $P$ - $T$ - $x$

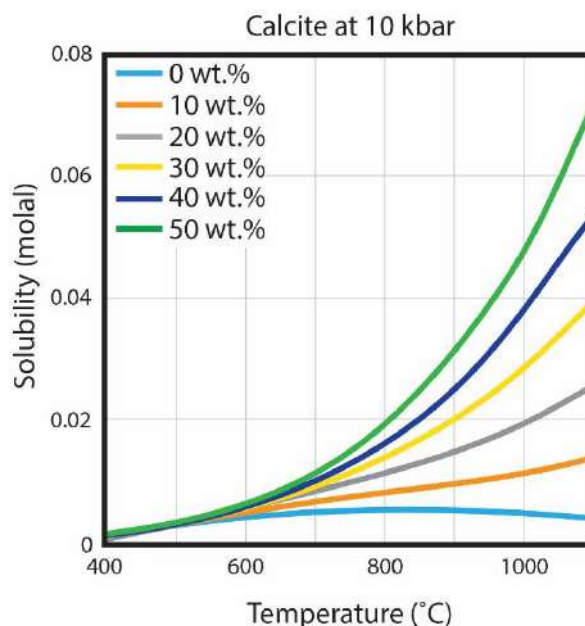


**Figure 1.**  $T$ - $x$  diagram illustrating the effect of temperature and salinity on calcite solubility in  $\text{H}_2\text{O}\pm\text{NaCl}$  fluids at 10 kbar. A clear salting-in behavior is visible, with solubility increases progressively with increasing salinity. Retrograde solubility trends are seen at pure  $\text{H}_2\text{O}$  conditions and grading to prograde trends by ~20 wt.% NaCl salinity.

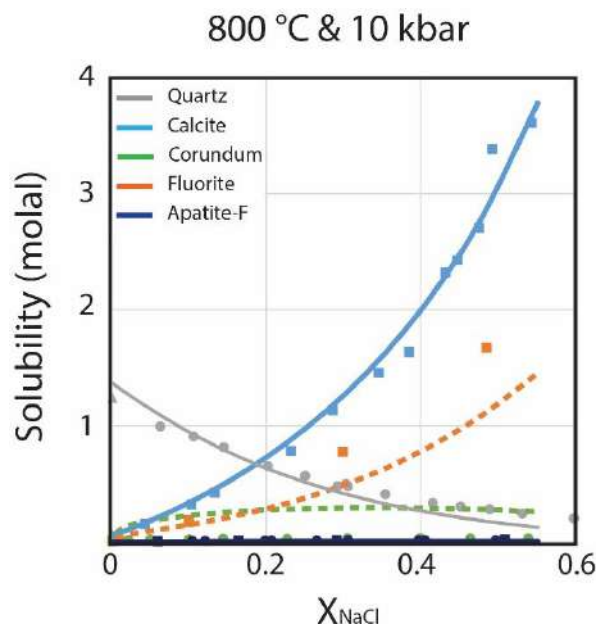


**Figure 2.** Mineral solubility in H<sub>2</sub>O-NaCl fluids at 800°C and 10 kbar. Density model predictions are shown with continuous curves; solid where well constrained with experimental data and dashed where extrapolated. Symbols indicate experimental data at the specified conditions, colored to match the mineral dissolving.

conditions on the solubility of common minerals (Figure 2). Depending on salt concentration, the identity of the most soluble mineral fluctuates; salting-in and salt-out behaviors were both noted depending on mineral type and *P-T* conditions.

Application of this new mineral solubility model to natural systems provides an increased capacity for understanding the impacts of fluid migration within the crust and upper mantle. This model encompasses H<sub>2</sub>O±NaCl fluids in a wide range of scientifically and societally important geologic settings (e.g. hydrothermal porphyries, sedimentary basins, and subduction zones). Due to the “simple” nature of the model, extrapolation and interpolation of data is possible with a high degree of accuracy over an extremely wide range of crustal to upper-mantle pressures and temperatures, and a large range of brine concentrations. This thermodynamic model, accounting for dissolution reactions in multi-component fluids over an extreme range of *P-T-x* conditions, will allow for robust modeling of reactions and mass transport in natural systems (i.e. sedimentary basins, subduction zones, hydrothermal ore deposits).

#### REFERENCES

- Akinfiyev, N.N., Diamond, L.W. (2009) A simple predictive model of quartz solubility in water–salt–CO<sub>2</sub> systems at temperatures up to 1000°C and pressures up to 1000 MPa, *Geochimica et Cosmochimica Acta* 73, 1597-1608.
- Bowers, T.S., Helgeson, H.C. (1983) Calculation of the thermodynamic and geochemical consequences of nonideal mixing in the system H<sub>2</sub>O-CO<sub>2</sub>-NaCl on phase relations in geologic systems: Equation of state for H<sub>2</sub>O-CO<sub>2</sub>-NaCl fluids at high pressures and temperatures, *Geochimica et Cosmochimica Acta* 47, 1247-1275.
- Dolejš, D., Manning, C.E. (2010) Thermodynamic model for mineral solubility in aqueous fluids: theory, calibration and application to model fluid-flow systems, *Geofluids* 10, 20-40.
- Galvez, M.E. et al. (2015) The solubility of rocks in metamorphic fluids: A model for rock-dominated conditions to upper mantle pressure and temperature, *Earth and Planetary Science Letters* 430, 486-498.

## 31 Years of PACROFI

Philip E. BROWN

Department of Geoscience, University of Wisconsin-Madison, Madison, Wisconsin, U.S.A.

E-mail: pebrown@wisc.edu

The idea for PACROFI was hatched by Ed Roedder and Dave Norman in April 1985 while attending the 8<sup>th</sup> European Current Research on Fluid Inclusions meeting in Germany. As explained by Dave Norman, "...later that year an *ad hoc* committee was formed consisting of E. Roedder, R.J. Bodnar, P.E. Brown, A.R. Campbell and D. Norman. We first decided to determine the interest in forming an American group (ACROFI). A brochure was sent to about 1400 people and, much to our surprise, over 250 replied." (GCA, 1988). As shown in the chart below the first meeting in January 1987 was a big success and the biennial tradition was born. ACROFI was quickly renamed PACROFI to be inclusive of the entire hemisphere and except for 3 meetings that did not come off for various reasons here we are 31 years later gathering for the XIV<sup>th</sup> edition. Nearly 850 abstracts have been submitted to the previous XIII meetings, roughly 2/3 oral and 1/3 posters.

ACROFI/ PACROFI	Year	Location	Main Organizers	# People	# Abst	# Oral	# Posters	Dinner/Banquet
I	1987	New Mexico Tech: Macey Center	Dave Norman Andy Campbell	140	65	45	20	On site - Macey Center
II	1989	Virginia Tech: Donaldson-Brown Conf Center	Bob Bodnar Many Students	>100	60	45	15	On site - Donaldson- Brown Conf Center
III	1990	U. Toronto: on campus	Ed Spooner Colin Bray	>100	81	51	30	Ontario Science Center
IV	1992	U.C. Riverside: Lake Arrowhead Conf Center	Michael McKibben Isabel Montanez Don Hall	108	95	51	44	On site
V	1994	Instituto de Investigaciones Electricas: Cuernavaca, Mexico	Georgina Izquierdo Tawn Albinson		85	48	37	On site
VI	1996	U. Wisc-Madison: Dept of Geoscience	Phil Brown Steffen Hagemann	~80	70	44	26	Spring Green - Frank Lloyd Wright Restaurant
VII	1998	UNLV Campus: Marjorie Barrick Museum	Jean Cline Dave Vanko		69	48	21	Lake Mead Cruise
VIII	2002	Halifax	Dan Kontak Alan Anderson		61	38	23	Harbour Queen I
IX	2008	USGS Reston National Center	Sean Brennan Harvey Belkin		64	41	23	Top of the Town, Arlington
X	2010	UNLV: on campus	Adam Simon Jean Cline		47	30	17	Walking Box Ranch
XI	2012	U. Windsor, Ontario	Ian Samson Joel Gagnon		52	35	17	Sprucewood Shores Estate Winery
XII	2014	USGS; Col State: Pingree Park	John Ridley Al Hofstra	48	39	25	14	On site - Pingree Park
XIII	2016	U. Missouri: on campus	Martin Appold Kevin Shelton Peter Nabelek	72	57	36	21	Les Bourgeois Vineyard
XIV	2018	Rice U.	Mike Smith Gary Gray					

Attendees have come from 36 (+?) countries (Argentina, Austria, Australia, Brazil, Canada, Chile, China, France, Germany, Hungary, India, Iran, Ireland, Israel, Italy, Japan, Mexico, Netherlands, New Zealand, Norway, Poland, Portugal, Romania, Russia, South Africa, South Korea, Spain, Sweden, Switzerland, Taiwan, Tajikistan, Turkey,

Ukraine, United Kingdom, USA, Uzbekistan). Prior to the fall of the wall, meeting organizers received abstracts from scientists in the USSR but the authors were generally unable to actually attend. This problem also regularly stymied the attendance of authors from China.

The 500+ oral presentations can be roughly grouped into the following “Topics”: Ore Deposits 28%, Methods/Techniques/Experiments 24%, Metamorphic/Igneous/Melt 16%, Sedimentary/Petroleum 12%, and Geothermal 6%. (9% of the total oral presentations came from the Cuernavaca meeting but the abstract volume doesn’t include a schedule.) The first 4 topics have been utilized in the table of contents of essentially all the meetings. Geothermal fluid inclusions were a common topic during the 1990s but are rarely seen in the last 15 years. Inclusions in metamorphic rocks were a common topic in the first 4-5 meetings but Melt inclusions are much more common as a subject of study in the last 20 years. Obviously, the techniques and technology changes that have changed the whole spread of the geosciences have dramatically affected fluid inclusion research as well.

Workshops have been a regular part of the meetings: At ACROFI I for example there were opportunities to learn about Raman Spectroscopy, Fluid Inclusions in Sedimentary/Petroleum Environments, and Inclusions in Mineral Exploration. In Toronto (1990) there was a Phase Equilibria workshop with several presentations.

Posters have been an integral part of all the meetings and many models have been used to effectively incorporate them into the heart of the meetings: have them up the whole meeting, have them clustered temporally and spatially with oral sessions on the same topics, and the tried and true poster session with “refreshments” either late in the afternoon or in the evening after dinner. PACROFI X set aside a half hour for 2-3-minute Poster Introductions immediately preceding the poster session. PACROFI IV and XII effectively used a modified Gordon Research Conference timetable with 2-4 hours of free time in the afternoons with the posters or oral sessions scheduled for the evenings.

Sponsorship has been quite varied through the years with Linkham Scientific, Horiba Scientific, and The McCrone Group, having contributed regularly. Various Petroleum (Exxon, Texaco, Amoco, Chevron) and Mining (Barrick, Homestake, Doe Run) companies have contributed to specific meetings. The USGS, NSF, and various professional societies (MSA, SEG, Geochemical Society, MAC) have made critical contributions to support speaker travel, reduced student fees, and abstract volume printing. And none of these meetings would have been possible without the support of the home academic institutions of the organizers providing meeting space and generally reduced costs for housing.

Field trips before or after the meetings have been a regular feature and have added greatly to the experiences of participants especially visitors from the other hemisphere. The conference Dinners/Banquets have provided some very special venues and lasting memories. Evening activities have generally remained under control although a couple of hot tub/pool events at PACROFI IV and V were ‘interesting’.

Two of the original organizers of this important series of meetings have passed on. Ed Roedder, the true ‘father’ of fluid inclusions in at least the western hemisphere died in 2006 after an incredible career mainly at the USGS. Dave Norman died unexpectedly in Africa in 2008 after having submitted several abstracts with students for the Reston meeting.

Abstract volumes for all of the previous XIII meetings will be available for examination during the meeting and I look forward to hearing other stories and recollections from the past helping to set the stage for future advances in this fascinating field.

#### REFERENCES

- GCA Vol 52, pp. 959-1076 (1988) Pan-American Current Research on Fluid Inclusions.
- GCA Vol 54, pp. 493-713 (1990) Current Research on Fluid Inclusions: PACROFI II.
- GCA Vol 56, pp. 1-302 (1992) Current Research on Fluid Inclusions: PACROFI III.
- Chemical Geology Vol 154, pp. 1-301 (1999) Pan-American Current Research on Fluid Inclusions VI

## Keynote – Quantitative Raman spectroscopy of single phase hydrocarbon gas-rich fluid inclusions

Robert C. BURRUSS

*U. S. Geological Survey, Reston, Virginia, U.S.A. (retired)*

*E-mail: bob.burruss@gmail.com*

For a number of years I have used Raman spectroscopy to quantify the composition of gas-rich hydrocarbon inclusions (HCFI) in the Appalachian basin for comparison with produced gases. Molecular compositions can be calculated in the system  $\text{CH}_4\text{-C}_2\text{H}_6\text{-C}_3\text{H}_8\text{-C}_4\text{H}_{10}\text{-CO}_2\text{-N}_2$  although some components may not be above detection limits in many inclusions. Initial comparison with produced gases shows that HCFI are richer in  $\text{C}_2+$  hydrocarbons and  $\text{CO}_2$  than produced gases. To eliminate the possibility that this difference is an analytical artifact, I have re-evaluated data acquisition routines, integration methods, and measured relative Raman scattering cross-sections (RRSC) up to 20 MPa in standard gas mixtures. To detect components at  $< 2$  mol %, Raman bands of  $\text{C}_2\text{H}_6\text{-C}_3\text{H}_8\text{-C}_4\text{H}_{10}\text{-CO}_2\text{-N}_2$  must be collected with long acquisition times and the highest spectral dispersion on the detector so that small peaks are well defined.  $\text{C}_4\text{H}_{10}$  is the most difficult to detect and quantify because it is the least abundant of the hydrocarbons in this system and the peaks overlap with a weak band in the quartz host. With careful baseline correction, either manual or algorithm driven integrations give comparable results. In some cases, the baseline of the  $\text{CO}_2$  Fermi diad may be affected by the presence of the polynuclear aromatic (“graphitic”) D band.

Relative Raman scattering cross-sections of gases in the literature are for gases at about atmospheric pressure and show some variation between publications. To test whether these variations are significant and whether there are variations in the RRSC at high pressure, I measured spectra on two standard gas mixtures at pressures up to 20 MPa in a high pressure optical cell. The results were reasonably consistent with published values with no variation with pressure. Therefore, molecular compositions of gas-rich HCFI can be reliably calculated from Raman spectra.

In addition to composition, it is possible to calculate the density of the  $\text{CH}_4$ -rich gas from the well calibrated shift of the  $\nu_1$  band ( $\sim 2915\text{ cm}^{-1}$ ) with density for pure  $\text{CH}_4$ . Combined with molecular composition, the density should allow calculation of the PVT properties of the trapped fluid. However some caution is required because we know from work on  $\text{CH}_4\text{-CO}_2$  mixtures that additional components in the gas can affect the correlation of methane peak position with the density of pure methane. These effects become significant when the methane content drops below 90 mol %. Based on experiments at CSIRO with Julien Bourdet on the system  $\text{CH}_4\text{-C}_6\text{H}_{14}$  in which  $\text{CH}_4$  peak position was measured for both the coexisting liquid and vapor phases, it appears that the peak position shifts with the density of mixture, such that the methane peak position is inconsistent with the calibration for pure methane. The shift in the  $\text{CH}_4$  peak position with hydrocarbon fluid composition and density needs to be studied further to establish the accuracy with which PVT properties of gas-rich HCFI can be calculated from Raman spectra.

It is clear that Raman spectroscopy can be used to calculate the molecular composition and density of  $\text{CH}_4$ -rich HCFI. Extending this approach to HCFI with compositions of condensates and oils has been impossible due to the overwhelming intensity of fluorescence of aromatic components in these fluids. Based on my experience to date, I believe it is unlikely that any Raman spectroscopic method will be successful in measuring the molecular composition of gases in fluorescent HCFI.



## Low-temperature phase equilibria of saline aqueous systems containing carbonate, bicarbonate and other anions

Michael H. DECINDIS<sup>1,2</sup>, Matthew STEELE-MACINNIS<sup>1</sup>

<sup>1</sup>Department of Earth & Atmospheric Sciences, University of Alberta, Edmonton, Alberta, Canada

<sup>2</sup>Department of Soil, Water, and Environmental Science, University of Arizona, Tucson, Arizona, U.S.A.

Email: steelema@ualberta.ca

Fluids in many geologic settings, ranging from sedimentary basins to magmatic-hydrothermal environments, are saline brines. Therefore, methods to determine salt concentrations in fluid inclusions are needed to interpret the record of fluids based on fluid inclusions. Several methods can be used for this purpose, and the main tool is microthermometry. Laser-ablation (LA) ICPMS analysis has revolutionized this field and allows quantification of major and trace elements in inclusions, but it is very challenging to apply to the analysis of *anions* in fluid inclusions. As such, analysis of data from LA-ICPMS generally assumes that chloride is the only anion present in an inclusion. However, we know that other anions may be present and, in some settings, these other anions can comprise a major portion of the composition. Sulfate, carbonate and bicarbonate are some of the key suspects, but others (hydroxide, fluoride, nitrate) may also be present in certain settings.

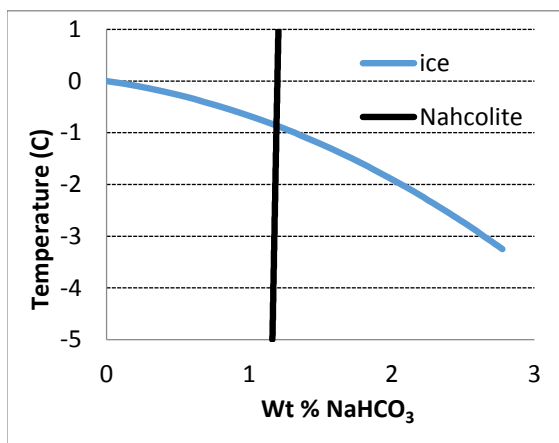


Figure 1. Liquidus diagram for H<sub>2</sub>O-NaHCO<sub>3</sub>

This study explores the low-temperature phase relations in systems containing anions other than chloride. Pitzer's ion interaction model (Pitzer, 1973) allows modeling the solid-liquid equilibria of saline aqueous systems over a range of temperature-pressure conditions and up to high liquid salinities. Steele-MacInnis et al. (2016) described the application of Pitzer's model to construct theoretical solidus-liquidus phase diagrams for different aqueous salt systems in the system H<sub>2</sub>O-Na-K-Ca-Mg-Fe-Cl. Walter et al. (2017) extended this analysis to sulfate-bearing fluids. Here, we extend this analysis to model the solidus-liquidus phase relations of a variety of other saline systems, particularly considering the additional anions bicarbonate and carbonate, although others are also tested for reconnaissance. We present new phase diagrams for binary water-salt systems as well as ternary and higher-order phase diagrams to explore the phase relations in

liquids containing multiple anions. Intersection of the ice liquidus and salt liquidus lines constrains the eutectic point of each system. Applications of these models will assist in interpreting the nuances of microthermometric properties of multi-component inclusions, particularly for those with exotic compositions such as in granitic pegmatites and in fluids related to evaporates.

### REFERENCES

- Pitzer, K.S. (1973) Thermodynamics of electrolytes. I. Theoretical basis and general equations. *J. Physical Chemistry* 77, 268-277.
- Steele-MacInnis et al. (2016) Application of Low Temperature Thermometric Data for Interpreting Multicomponent Fluid Inclusion Composition. *Earth-Science Reviews* 159 14-35.
- Walter, B.F. et al. (2017) Sulfate brines in fluid inclusions of hydrothermal veins: Compositional determinations in the system H<sub>2</sub>O-Na-Ca-Cl-SO<sub>4</sub>. *Geochim Cosmochim Acta* 209 184-203.



## Open system diagenesis in unconventional reservoirs of the Midland Basin, Howard County, Texas

Erich de ZOETEN and Robert H. GOLDSTEIN

Kansas Interdisciplinary Carbonates Consortium, Department of Geology, University of Kansas, Lawrence, Kansas, U.S.A.

E-mail: gold@ku.edu

Diagenetic alteration commonly controls reservoir quality in carbonates. Diagenetic alteration in basinal systems, with abundant fine-grained deposits, has been proposed to be relatively closed to new fluids and, therefore, relatively simple and predictable (Mazzullo and Harris, 1992; Mazzullo, 1994). Alternatively, open-system hydrothermal fluid flow in carbonates has been shown to be an important mechanism for creating reservoir porosity in conventional reservoirs (e.g. Hiemstra and Goldstein, 2015). This study evaluates the diagenetic history of the Wolfcamp A stratigraphic unit near the toe-of-slope in the eastern Midland Basin. The findings show that the Midland Basin fluid and thermal history was an open one, with reflux of residual evaporite brines during burial, and hydrothermal fluid flow during and after Laramide fracturing. This late stage of fracturing and hydrothermal fluid flow was important in localizing reservoir quality and thermal maturity. This finding should lead to new strategies for localizing the best reservoirs in the Permian Basin and other unconventional plays. Fluid inclusion, petrographic, and isotopic data are key in recognizing the complex history of fluid flow that controls the thermal history and diagenesis of this unconventional reservoir.

Transmitted-light microscopy, UV, cathodoluminescence, and SEM-EDS microscopy, as well as  $\delta^{18}\text{O}$ ,  $\delta^{13}\text{C}$ ,  $^{87}\text{Sr}/^{86}\text{Sr}$ , and fluid inclusion analyses are used to evaluate the history of fluid flow and thermal history as a means of determining controls on reservoir quality. The diagenetic history is divided into three stages: Early Stage, near the sediment-water interface; Burial Stage, during burial and before tectonic fracturing; and Fracturing Stage, with the onset of tectonic fracturing and overlapping with late events of hydrocarbon migration (Figure 1).

For the Burial Stage, Calcite Cement 2  $\delta^{18}\text{O}$  values lead to calculated precipitation temperature of about 73 °C. The  $^{87}\text{Sr}/^{86}\text{Sr}$  value is 0.707714, slightly more radiogenic than Mid - Late Permian (Guadalupian – Ochoan) seawater. Calcite Cement 3 reduced most of the remaining porosity in mud-poor packstones. Its  $T_h$  values are 68 – 83 °C;  $T_{m\text{ ice}}$  data indicate a high salinity fluid from 17.4 – 18.5 wt% NaCl eq. Calculated  $\delta^{18}\text{O}_{\text{water}}$  of 6.4 – 9.6‰ is consistent with a residual evaporite brine generated in the Leonardian and Guadalupian, that refluxed downward into the Wolfcamp A (Figure 2). Anhydrite cement yields fluid inclusion data indicating precipitation at low temperature (< 50 °C)

from a brine of 17.4 – 26.8 wt% NaCl eq. A potential explanation is that anhydrite precipitated during active reflux of highly evaporated late Ochoan seawater. This hypothesis is supported by a  $^{87}\text{Sr}/^{86}\text{Sr}$  value of 0.707491. The timing would have had to have been during the late Ochoan, or soon after in the Triassic, because the reflux of low-temperature brines penetrated a rock that had already been heated to 68 – 83 °C during burial (Figure 2).

The Fracturing Stage began with brittle failure of the rock to form planar, consistent aperture fractures. The Laramide orogeny and Basin and Range deformation are the only known post-Permian tectonic events capable of causing extensive fracturing. Calcite cement 5 yields  $T_h$  of 68 – 93 °C and  $T_{m\text{ ice}}$  salinity of 21.5 – 25.0 wt% NaCl eq.  $\delta^{18}\text{O}_{\text{water}}$  was 6.5 – 10.2‰ (Figure 2). Calcite cement 6 precipitated from a hot ( $T_h$  of 130 – 160 °C) high salinity (22.8 – 25.4 wt% NaCl eq) fluid. A separate gas phase was present during precipitation. For quartz cement 2, fluid inclusion  $T_h$  indicate precipitation at 76 – 113 °C, and  $T_{m\text{ ice}}$  indicate a brine of 22.5 – 27.0 wt% NaCl eq. Temperature for the

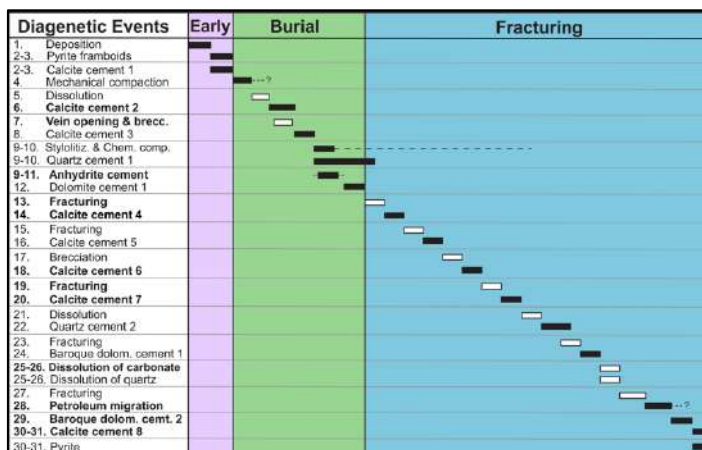
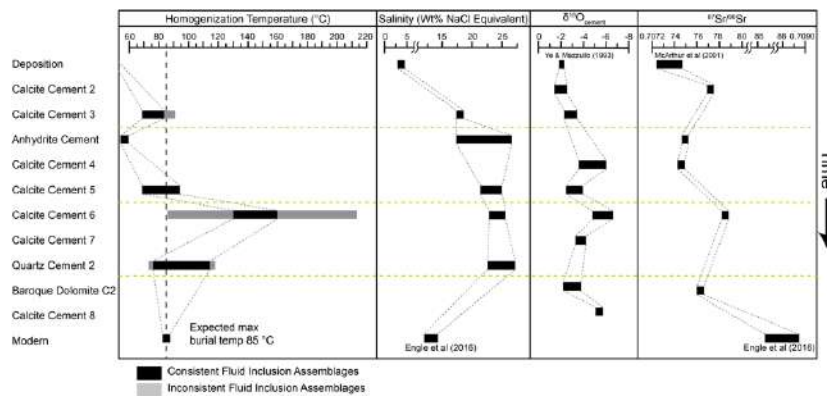


Figure 1. Paragenesis of Wolfcamp A, Midland Basin.

quartz cement fluctuated through time, and a correlation between  $T_h$  and  $T_m$  ice indicates events of fluid mixing between a lower temperature (~75 °C), higher salinity (~26.5 wt% NaCl eq) fluid and a higher temperature (~105°C), lower salinity (~23 wt% NaCl eq) fluid. Following a dissolution event and oil migration, baroque dolomite cement 2 precipitated. Temperature of precipitation calculated from  $\delta^{18}O_{\text{cement}}$  was somewhere between 125 – 181 °C. The  $^{87}\text{Sr}/^{86}\text{Sr}$  (0.707633) is relatively non-radiogenic. Later, calcite cement 8 precipitated at a temperature of 113 – 151 °C, calculated from  $\delta^{18}O_{\text{cement}}$ .



**Figure 2.** Summary of fluid inclusion and geochemical data from Wolfcamp A, Midland Basin

These data indicate that during the Burial Stage (Permian to Cretaceous), Permian evaporated seawater refluxed and displaced Leonardian connate water. Thermal conditions were at those predicted from burial history, or lower during times of active reflux. During the Fracturing Stage, Laramide (latest Cretaceous to Eocene) and later tectonism led to hydrothermal fluid flow, with northward migration of fluids out of the Val Verde Basin. This system would have been driven by hydraulic head in uplifted areas to the south. Hydrothermal fluids yielded localized thermal maturity, oil migration, and porosity in the Wolfcamp A, important for localization of the best reservoirs.

On the basis of observations made in this study of the Wolfcamp A in the eastern Midland Basin, predicting reservoir properties in unconventional reservoirs in the Midland Basin, and other distal foreland settings, must incorporate an open and thermally dynamic model, not a closed fluid system model in which thermal history is governed by burial history alone. The burial stage was dominated by vein-opening and calcite and anhydrite cementation. Fluid temperatures were consistent with those at and close to burial at the end of the Permian and also record some low temperatures consistent with active reflux from the surface. Fluid salinities increased to values consistent with Ochoan reflux of residual evaporite brines. Although facies had relatively low permeability, active and open fluid flow, caused by reflux from the surface, had a major impact on diagenesis and thermal structure. After fracturing from the Laramide orogeny, open-system diagenesis began once again and resulted in tectonically valved hydrothermal fluid flow. This resulted in late moldic dissolution, oil migration and generation, as well as calcite, quartz, and dolomite cementation. Based on burial history and Sr isotope values, the hydrothermal fluid flow was advective in nature, long distance, and came from the Val Verde Basin, not from basement or deeper parts of the Midland Basin. This study is consistent with others in the southern US Midcontinent and Delaware Basin. All show evidence of long-distance fluid migration of hydrothermal fluids from distant foreland areas, but the Midland Basin study shows the impact of open system reflux and hydrothermal fluid flow on unconventional reservoirs, traditionally hypothesized to act as closed systems to fluids.

REFERENCES

Hiemstra, E.J. and Goldstein, R.H., 2015, Repeated injection of hydrothermal fluids into downdip carbonates: a diagenetic and stratigraphic mechanism for localization of reservoir porosity, Indian Basin Field, New Mexico, USA: Geological Society, London, Special Publications 406, no. 1, p. 141-177.

Mazzullo, S. J. and Harris, P.M., 1992, Mesogenetic dissolution: Its role in porosity development in carbonate reservoirs: AAPG Bulletin, v. 76, p. 607-620.

Mazzullo, S. J., 1994, Lithification and porosity evolution in Permian periplatform limestones, Midland Basin, Texas: Carbonates and Evaporites, v. 9, p. 151-171.

## An Investigation of the phase behavior and composition of the surface and crust of Titan using Synthetic Fluid Inclusions combined with Raman spectroscopy

Hunter R. EDWARDS, D. Matthew SUBLETT, Robert J. BODNAR

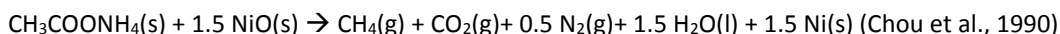
Fluids Research Laboratory, Department of Geosciences, Virginia Tech, Blacksburg, Virginia, U.S.A.

E-mail: ehunter5@vt.edu

Our knowledge of the physical and chemical properties of planetary bodies in the solar system is based mainly on studies of meteorites and data returned to Earth from orbiters and rovers. Accordingly, the Cassini mission (1997-2017) collected data in the Saturnian system, and the Huygens probe provided the first direct investigation of the composition of the atmosphere and surface of Titan (Niemann et al., 2005; Niemann et al., 2010). While these data provide information concerning the composition of planetary bodies, they do not provide details concerning the phase state at various locations on the surface and in the crust or mantle of these bodies. Here, we simulate the phase behavior of the Titan surface and crust using synthetic fluid inclusions (SFI) with Titan-like composition, combined with Raman spectroscopy.

Titan has an atmosphere that is rich in N<sub>2</sub> and CH<sub>4</sub>, a surface composed of CH<sub>4</sub>, C<sub>2</sub>H<sub>6</sub>, C<sub>2</sub>H<sub>2</sub>, C<sub>2</sub>N<sub>2</sub>, and CO<sub>2</sub> (Dalton, 2010; Niemann et al., 2005; Niemann et al., 2010), and a clathrate and ice crust (Fortes et al., 2007; Grindrod et al., 2008). The interior of Titan consists of a global (NH<sub>4</sub>)<sub>2</sub>SO<sub>4</sub> ocean, an ice VI shell, and a hydrated silicate core (Tobie et al., 2005; Fortes et al., 2007; Grindrod et al., 2008; Fortes, 2012; Sohl et al., 2014) (see Figure 1). Additionally, the surface temperatures on Titan ranges from -203°C to -73°C (Dalton, 2012). Using these data, SFI were created to replicate the compositions of the atmosphere, surface and crust on Titan.

The CH<sub>4</sub>-CO<sub>2</sub>-N<sub>2</sub>-H<sub>2</sub>O system was utilized because it is compositionally analogous to the surface and subsurface of Titan. Using the procedure from Sterner and Bodnar (1984), SFI were created by mixing CH<sub>3</sub>COONH<sub>4</sub>, NiO, and H<sub>2</sub>O, following the method outlined by Chou et al. (1990). This mixture was added to a platinum capsule containing a thermally-fractured, inclusion-free, Brazilian quartz core. The capsule was then welded and placed in a cold-seal pressure vessel and brought to experimental conditions of 600°C and 2 kbar. At these conditions the following reaction occurs:



At the experimental conditions, the fractured quartz core anneals and traps fluid inclusions with calculated compositions of 10.3 mol % CH<sub>4</sub> and CO<sub>2</sub>, 74.2 mol % H<sub>2</sub>O, and 5.2 mol % N<sub>2</sub>.

Every covalently-bonded molecule has a given vibrational energy that gives rise to a specific vibrational band (peak) in the Raman spectrum (Figure 2). The relative proportions of the different species can be estimated from the areas under the peaks using the Placzek equation. This method was used to determine relative abundances of CH<sub>4</sub>, CO<sub>2</sub>, and N<sub>2</sub> in the mixture.

A Raman microprobe and a TMS 92 Linkam stage are used to collect spectra of SFI at low temperatures. At room temperature, a liquid and vapor phase are present in the SFI. The fluid phase at room temperature is mostly H<sub>2</sub>O and the vapor phase at room temperature contains CH<sub>4</sub>, CO<sub>2</sub>, and N<sub>2</sub>. As the inclusion is cooled to -190°C, a

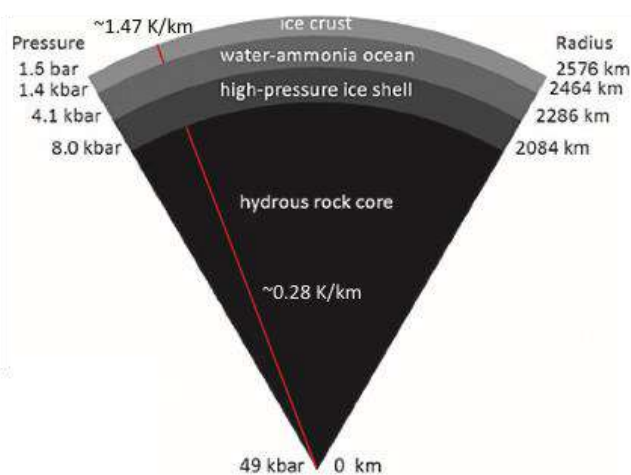


**Figure 1.** Cross section of Titan, with geothermal gradients in red, showing the interior structure of Titan. Modified from Sohl et al., 2014.

temperature that is analogous to the surface of Titan, clathrates form. At  $-50^{\circ}\text{C}$  spectra were collected of the vapor and clathrate phases. The vapor phase contains  $\text{CH}_4$ ,  $\text{N}_2$ , and lower proportions of  $\text{CO}_2$  compared to room temperature. Further, at this temperature  $\text{CO}_2$  clathrate is present. At  $-190^{\circ}\text{C}$  the clathrates that form near the vapor bubble contain abundant  $\text{CH}_4$ ,  $\text{N}_2$ , and  $\text{CO}_2$ , but only  $\text{CO}_2$  clathrate is detected further from the vapor bubble. Raman spectra of the vapor phase were collected at  $-190^{\circ}\text{C}$ , however no  $\text{CH}_4$ ,  $\text{N}_2$ , or  $\text{CO}_2$  are detected at this temperature. It is likely that these molecules are present within the vapor bubble, but at levels too low to be detected by Raman, with most of these species contained in clathrates. This study is continuing, with the goal to determine the phase behavior and composition at temperatures that are within the range of temperatures present on the surface of Titan.

Understanding the phase behavior for Titan provides useful information that can allow for a better understanding for the composition of Saturnian and Jovian satellites, as well as the formation and evolution of planetary bodies in the outer solar system.

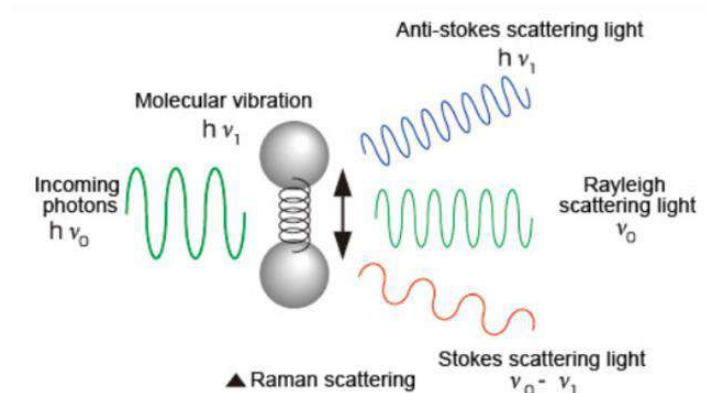


**Figure 2.** When the incident photon contacts the molecule, the molecule vibrates and scatters light from the photon. The light is either scattered elastically (Rayleigh scattering) or inelastically (Raman scattering). A “fingerprint” for the molecule scattering the photons is provided by the inelastic scattered light, which is proportional to the vibrational energy for that molecule. Image provided by [www.hamamatsu.com](http://www.hamamatsu.com).

#### REFERENCES

- Chou, I. M. et al. (1990) High-density volatiles in the system C-O-H-N for the calibration of a laser Raman microprobe, *Geochim. Cosmochim. Acta* 54, 535-543.
- Dalton, J. B. (2010) Spectroscopy of Icy Moon Surface Materials, *Space Sci. Rev.* 153, 219-247.
- Fortes, A. D. et al. (2007) Ammonium Sulfate on Titan: Possible origin and role in cryovolcanism, *Icarus* 188, 139-153.
- Fortes, A. D. (2012) Titan’s internal structure and the evolutionary consequences, *Planet. Space Sci.* 60, 10-17.
- Grindrod, P. M. et al. (2008) The long-term stability of a possible aqueous ammonium sulfate ocean inside Titan, *Icarus* 197, 137-151.
- Niemann, H. B. et al. (2005) The Abundances of constituents of Titan’s atmosphere from the GCMS instrument on the Huygens probe, *Nature* 438, 779-784.
- Niemann, H. B. et al. (2010) Compositions of Titan’s lower atmosphere and simple surface volatiles as measured by the Cassini Huygens probe gas chromatograph mass spectrometer experiment, *J. Geophys. Res.* 115, 1-22.
- Sohl, F. et al. (2014) Structural and tidal models of Titan and inferences on cryovolcanism, *J. Geophys. Res. Planets* 119, 1013-1036.
- Tobie, G. et al. (2005) Titan’s internal structure inferred from a coupled thermal-orbital model, *Icarus* 175, 496-502.
- Stern, S. M. and Bodnar, R. J. (1984) Synthetic Fluid Inclusions in natural quartz I. Compositional types synthesized and applications to experimental geochemistry, *Geochim. Cosmochim. Acta* 48, 2659-2668.

## Diagenesis and fluid-rock interactions in the Upper Lacq carbonate petroleum reservoir (Southwestern France)

Alexy ELIAS BAHNAN<sup>1</sup>, J. PECQUEUR, J. PIRONON<sup>1</sup>, C. CARPENTIER<sup>1</sup>, E. C. GAUCHER<sup>2</sup>, S. CALASSOU<sup>2</sup>, A. VIRGONE<sup>2</sup>

<sup>1</sup>CNRS-CREGU, GeoRessources Lab, Université de Lorraine, Nancy, France

<sup>2</sup>TOTAL, CSTJF, Pau, France

E-mail: alexy.elias-bahnan@univ-lorraine.fr

Fluids circulating in foreland basins can have strong impacts on petroleum systems and reservoir properties. This applies to the Upper Cretaceous Lacq reservoir of the Aquitaine Basin in southwestern France located north of the Pyrenean Mountains. In this area, dolomitic reservoirs were considered for a long time the result of an early dolomitization process in a context of shallow evaporitic carbonate platforms. However, a recent revisiting of the geodynamic model of the Pyrenean and South Aquitaine domain involving Early Cretaceous hyperextension with mantle exhumation led to suppose the impact of deeply sourced hydrothermal fluids on the diagenesis of reservoirs (Jammes et al., 2010, 2009; Lagabrielle et al., 2010; Vacherat et al., 2016; Salardon et al., 2017; Corre et al., 2018). The targeted 650m-deep oil reservoir is part of a salt-core anticline located in a complex area marked by hyper-extension during Early Cretaceous and compression during Late Cretaceous and Paleogene Pyrenean orogeny (Vacherat et al., 2014, 2016). Productive reservoirs include fractured Coniacian - Campanian limestones and dolomites unconformably overlying Albian-Cenomanian reefs while seals are provided by Upper Senonian marls and Paleocene shales (Biteau, 2006). However, little is known about the nature, origin and timing of fluid circulation in the basin. Aims of this work are to (1) revisit and reconstruct the diagenetic history of the Lacq field, (2) test the impact of fluid-rock interactions and thermochemical sulphate reduction (TSR) on reservoir properties and (3) link the involved fluids to the geodynamic history of the basin.

Petrographic observations on core samples from the Lacq reservoir reveal a paragenetic sequence of 19 phases. Bacterial activity in the eogenetic realm is represented by micrite coatings and framboidal pyrites produced by bacterial sulphate reduction (BSR). These phases are cross-cut by silica-rich microfractures that feed cm-scale chert nodules. Fluctuations in redox conditions are witnessed by the cathodoluminescence of zoned dog-tooth early calcites that hint towards changes in iron contents. These changes in redox states mark the transition to the mesogenetic realm. Minor phases of ferroan calcites indicate a dominance of reducing conditions. The main diagenetic modifications are recorded by pervasive dolomitization episodes that resulted in planar porphyrotropic (P), euhedral (E) and subhedral (S) dolomites. These phases were later affected by brecciation and fracturing coupled with saddle dolomite cementation. A minor phase of talc replaced some of the matrix and saddle dolomites. These episodes occurred before the maximum burial as bedding-parallel stylolites cut across all the dolomite phases. The stylolites are then reopened and infilled by non-ferroan blocky calcite cements with abundant oil and aqueous inclusions. Return to oxidizing conditions is suggested by the non-luminescent behavior of these calcite. The main pulse of oil migration continued till after the calcite cements and stopped before the precipitation of the final sulphate and sulphide phases.

$\delta^{18}\text{O}$  and  $\delta^{13}\text{C}$  isotopes were obtained from the dolomitized host rocks, i.e. matrix dolomites, saddle dolomites and the final blocky calcite phases.  $\delta^{13}\text{C}$  of the host rocks are in the range of +2.49‰ to +3.23‰ PDB and  $\delta^{18}\text{O}$  between -2.25‰ to -7.00‰ PDB. Saddle dolomites show a similar range of  $\delta^{13}\text{C}$  with values between +0.51‰ to +2.83‰ PDB but a more depleted  $\delta^{18}\text{O}$  range of -8.21 to -9.09‰ PDB. Blocky calcites are slightly more depleted with a  $\delta^{13}\text{C}$  range of -1.48 to +1.53‰ PDB while  $\delta^{18}\text{O}$  vary between -10.38 and -12.38‰ PDB. Host rocks precipitating in equilibrium with Upper Cretaceous seawater have a  $\delta^{13}\text{C}$  range of +1 to +3‰ PDB and a  $\delta^{18}\text{O}$  range of -2.5 to -4.7‰ PDB. The  $\delta^{13}\text{C}$  of the studied phases are within the same range to that of Upper Cretaceous seawater. The more depleted  $\delta^{13}\text{C}$  of the blocky calcites is likely due to contamination by oil inclusions and the input of  $\delta^{13}\text{C}$  from the organic hydrocarbons.  $\delta^{18}\text{O}$  data show a negative trend with increasing depletion from the host rocks to the saddle dolomites then to the blocky calcites.

Microthermometry data were obtained from fluid inclusions (FIs) in matrix dolomites, saddle dolomites and calcite phases. FIs in matrix dolomites have a  $T_h$  mode range of 80-90°C and salinities of 0-6 eq. wt% NaCl. Higher  $T_h$  mode of 140°C and salinities of 2-10 eq. wt% NaCl are recorded in the saddle dolomites, while blocky calcites have colder FIs with a  $T_h$  mode of 80°C and salinities of 0-3 eq. wt% NaCl. Oil inclusions in blocky calcites have  $T_h$  values

between 56 and 63°C. The first approximation the data set shows is a gradual increase in temperature from the matrix dolomite to the saddle dolomite phases before cooling with the blocky calcites. Salinities however are relatively low with a very similar range among the studied phases. Raman spectroscopy on the gas phase of fluid inclusions in blocky calcites indicates that the only detectable gas is H<sub>2</sub>O vapor.

Using the fractionation curves of Friedman and O'Neil (1977) and the fractionation equation between dolomite and water (Horita, 2014), the fluids precipitating the matrix dolomite have  $\delta^{18}\text{O}$  values plotting in the domain of formation waters that were buffered by the host rocks. Similarly, saddle dolomite precipitated from fluids whose  $\delta^{18}\text{O}$  is also in agreement with formation fluids but at higher temperatures and close to the domain of magmatic waters. Using the fractionation equation between calcite and water (O'Neil, 1969), parent fluids of the blocky calcite have a  $\delta^{18}\text{O}$  value indicative of a mixture between formation and meteoric fluids.

This preliminary data set indicates that fluids participating in the diagenesis of Upper Lacq carbonate petroleum reservoir were involved in high rates of fluid-rock interactions leading to the buffering of the  $\delta^{13}\text{C}$  signature. Depletion of the  $\delta^{18}\text{O}$  isotope is linked to thermal fractionation during burial diagenesis at elevated temperatures. Analyses of fluid origins reveal that the matrix dolomites are sourced from formation fluids whose salinities were probably lowered by dilution with water from clay dehydration reactions. The same reasoning applies to saddle dolomites but with higher temperature. These results are not in agreement with an early dolomitization model but rather suggest the impact of hot hydrothermal fluids. Fluids precipitating blocky calcites could be a mixture between formation and meteoric fluids that percolated downward and retained the  $\delta^{13}\text{C}$  of the host rocks upon buffering. The presence of oil inclusions next to aqueous inclusions in calcites can be explained by co-existence of mixed fluids and hydrocarbons during crystallization.

However, to better constrain the salinities and origin of cement phases, more microthermometry and Raman measurement are needed. LA-ICPMS will also be utilized to observe changes in the chemistry of fluids across different cement phases. Confocal laser scanning microscopy is necessary to reveal trapping pressure conditions of hydrocarbons. To understand sulfur sources and the possible involvement of TSR reactions in the diagenesis, multiple sulfur isotope measurements on anhydrite and pyrite will be performed.

#### REFERENCES

- Biteau, J.-J. et al. (2006). The Aquitaine Basin. *Petroleum Geosciences* 12(3), pp. 247-273.
- Corre, B. et al. (2018). Fluid circulations in response to mantle exhumation at the passive margin setting in the north Pyrenean zone, France. *Mineral. Petrol.* 0, 1–24
- Friedman, I., O'Neil, J. R. (1977). Compilation of stable isotope fractionation factors of geochemical interest. In M. Fleischer (Ed.), *Data of Geochemistry* (Sixth Ed., Washington) 440.
- Horita, J. (2014). Oxygen and carbon isotope fractionation in the system dolomite–water–CO<sub>2</sub> to elevated temperatures. *Geochimica et Cosmochimica Acta*, 129, 111–124.
- Jammes, S. et al. (2009). Tectonosedimentary evolution related to extreme crustal thinning ahead of a propagating ocean: Example of the western Pyrenees. *Tectonics* 28
- Jammes, S. et al. (2010). Extreme crustal thinning in the Bay of Biscay and the Western Pyrenees: From observations to modeling. *Geochemistry, Geophys. Geosystems* 11.
- Lagabrielle, Y. et al. (2010). Mantle exhumation, crustal denudation, and gravity tectonics during Cretaceous rifting in the Pyrenean realm (SW Europe): Insights from the geological setting of the lherzolite bodies. *Tectonics* 29
- O'Neil, J. R., et al. (1969). Oxygen Isotope Fractionation in Divalent Metal Carbonates. *J. of Chem. Phys.* 51, 5547–5558.
- Salardon, R. et al. (2017). Interactions between tectonics and fluid circulations in an inverted hyper-extended basin: Example of mesozoic carbonate rocks of the western North Pyrenean Zone (Châinons Béarnais, France). *Mar. Pet. Geol.* 80, 563–586.
- Vacherat, A. et al. (2014). Thermal imprint of rift-related processes in orogens as recorded in the Pyrenees. *Earth Planet. Sci. Lett.* 408, 296–306.
- Vacherat, A. et al. (2016). Rift-to-collision transition recorded by tectonothermal evolution of the northern Pyrenees. *Tectonics* 35, 907–933.

## Constraining the history of fluid events using the fluid inclusion assemblage (FIA) method for collecting, displaying and interpreting microthermometric data

Andr s FALL<sup>1</sup>, Robert J. BODNAR<sup>2</sup>

<sup>1</sup>Bureau of Economic Geology, Jackson School of Geosciences, The University of Texas at Austin, Austin, Texas, U.S.A.

<sup>2</sup>Fluids Research Laboratory, Department of Geosciences, Virginia Tech, Blacksburg, Virginia, U.S.A.

E-mail: andras.fall@beg.utexas.edu

Fluid inclusion microthermometric data provide information on the Pressure-Temperature-Composition (PTX) fluid history associated with geological processes. However, microthermometric data can be used to infer the original trapping conditions only if the inclusions obey Roedder's Rules (Bodnar, 2003), the assumptions stating that the inclusion trapped a single, homogeneous fluid, nothing is added to or lost from the inclusion after trapping, and the inclusion is isochoric. The only way to test these rules is by obtaining the data from Fluid Inclusion Assemblages (FIA), that represent the finest (shortest time duration) geologic event that can be constrained using fluid inclusions (Diamond, 1990; Goldstein and Reynolds, 1994; Bodnar, 2003). Homogenization temperature ( $T_h$ ) data obtained from fluid inclusions is often used to reconstruct temperature history of a geologic event. The precision with which fluid inclusions constrain the temperatures of a fluid events depends on the precision with which the temperature of an FIA can be determined. Though the methodology for the rigorous collection of fluid inclusion data has been accepted for many years, acceptable ranges in data for individual FIAs in various geologic environments has not been scientifically defined. The goal of this study is to determine ranges in  $T_h$  for well characterized FIAs from different geologic environments. This approach allows researchers to test the quality and reliability of fluid inclusion data, to maximize the amount of information that can be extracted from those data, and place rigorous constraints on fluid evolution and P-T history of geologic systems.

$T_h$  variations within FIAs depend on many factors that vary within different geological environments, and in order to determine minimum and acceptable temperature ranges for FIAs formed in different environments we investigated FIAs in several geologic environments, including sedimentary, metamorphic, and magmatic hydrothermal systems. The samples analyzed in this study include FIAs from quartz cement bridges in natural fractures from tight-gas sandstones of the Piceance Basin, Colorado (Fall et al., 2015), fluorite from the Cave-in-Rock fluorspar district in southern Illinois, (Richardson and Pinckney, 1984), sphalerite from the Creede, Colorado, Ag-Pb-Zn-Cu epithermal vein deposit (Roedder, 1974), quartz from the Marble Canyon Pegmatite, California, hydrothermal quartz in veins from the Bingham porphyry Cu-Au-Mo deposit, Utah (Roedder, 1971; Landtwing et al., 2005)

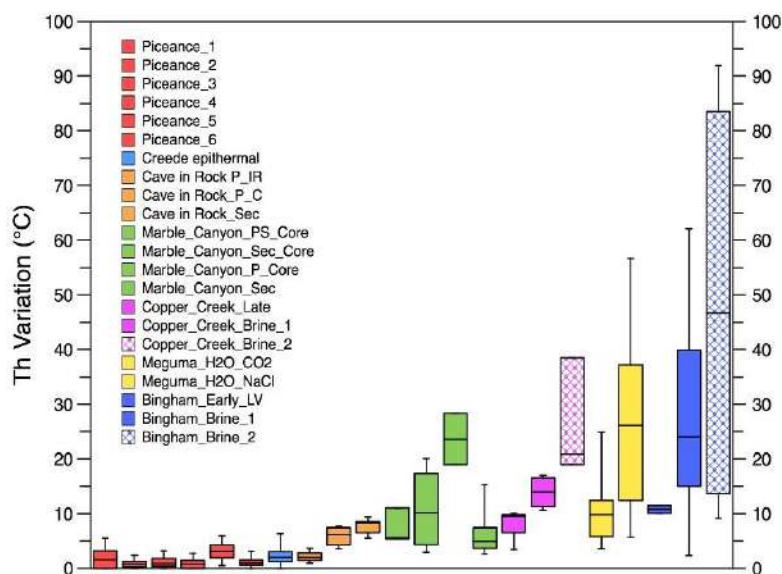


**Figure 1.** Box and whisker plots showing the range in  $T_h$  within individual FIAs sorted according to geologic environment. Shown are the complete range in observed  $T_h$  ranges, the 25<sup>th</sup> and 75<sup>th</sup> percentiles of the ranges and the median range for a given environment. Position along the X-axis is arbitrary and is arranged approximately according to the scatter in observed  $T_h$  range.

and the Copper Creek, Arizona, porphyry copper system, and quartz veins from the Meguma orogenic gold deposit in Nova-Scotia, Canada (Kontak et al., 2001).  $T_h$  variation within individual FIAs range from 0 to 6 °C in the Piceance Basin, from 1 to 9 °C in fluorites from Cave-In-Rock, from 0 to 6 °C in the Creede sphalerite, from 3 to 75 °C in quartz from Copper Creek and Bingham deposits, from 3 to 28 °C in quartz from the Marble Canyon pegmatite, and from 6 to 125 °C in quartz from the Meguma metamorphic terrane (Fig. 1). Data from this study were combined with literature data reported from well-characterized FIAs in the various environments to assess the achievable ranges in  $T_h$  for individual FIAs (Figure 2). We will also show examples that illustrate the precision with which the temperature of a geologic event can be constrained when data are obtained from FIAs that can be placed into a well-defined structural-digenetic.

#### REFERENCES

- Diamond, L.W., (1990) Fluid inclusions evidence for P-V-T-X evolution of hydrothermal solutions in late-alpine gold-quartz veins at Brusson, Val D'Ayas, Northwest Italian Alps. *Am. J. Sci.* 290, 912-958.
- Goldstein, R.H., Reynolds, T.J. (1994) Systematics of fluid inclusions in diagenetic minerals: SEPM Short Course 31, 199 p.
- Bodnar, R.J. (2003) Introduction to fluid inclusions, in: Samson, I., Anderson, A., Marshall, D. (Eds.), *Fluid Inclusions: Analysis and Interpretation*. Mineral. Assoc. Can. Short Course 32, 81-99.
- Fall, A., Eichhubl, P., Bodnar, R.J., Laubach, S.E., Davis, J.S. (2015) Natural hydraulic fracturing of tight-gas sandstone reservoirs, Piceance Basin, Colorado. *Geol. Soc. A Bull.* 127, 61-75.
- Kontak, D.J., Horne, R.J., Smith, P.K., 2001. Meguma gold deposits, Nova Scotia: overview of past work with implications for future work. *The Gangue, Geol. Assoc. Can., Min. Dep. Div. Newslett.* 71, 1-9.
- Landtwing, M.R., Pettke, T., Halter, W.E., Heinrich, C.A., Redmond, P.B., Einaudi, M.T., Kunze, K., 2005. Copper deposition during quartz dissolution by cooling magmatic-hydrothermal fluids: the Bingham porphyry. *Earth Planet. Sci. Lett.* 235, 229-243.
- Richardson, C.K., Pinckney, D.M., 1984. The chemical and thermal evolution of the fluids in the Cave-in-Rock fluorite District, Illinois: mineralogy, paragenesis, and fluid inclusions. *Econ. Geol.* 79, 1833-1856.
- Roedder, E., 1971. Fluid inclusion studies on the porphyry-type ore deposits at Bingham, Utah, Butte, Montana, and Climax, Colorado. *Econ. Geol.* 66, 98-120.
- Roedder, E., 1974. Changes in ore fluid with time, from fluid inclusion studies at Creede, Colorado. 4th Inter. Assoc. Gen. Ore Dep. (IAGOD) Symp., Varna, Bulgaria, *Proceed.* 2, 179-185.

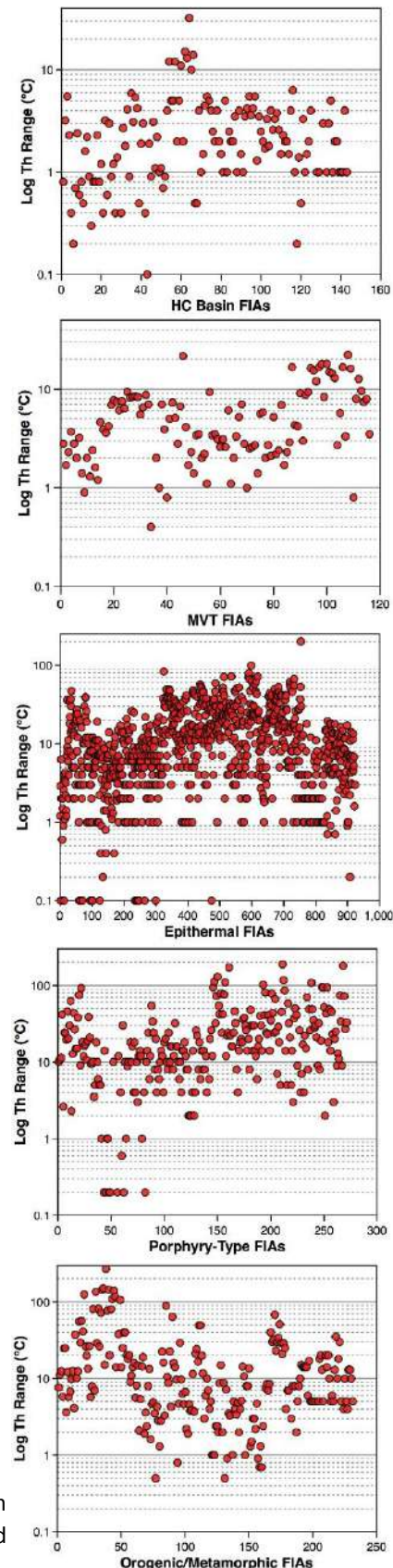


**Figure 2.** The log of the total range in  $T_h$  within individual FIAs from tight-gas basins, MVT-, epithermal-, porphyry-, and orogenic gold deposits obtained in this study and reported in the literature.

## Evolution of deformation in the Buck Mountain Fault damage zone, Cambrian Flathead Sandstone, Teton Range, Wyoming

Stephanie R. FORSTNER, Stephen E. LAUBACH, András FALL

Bureau of Economic Geology, Jackson School of Geosciences, The University of Texas at Austin, Austin, Texas, U.S.A.  
 E-mail: stephanie.forstner@beg.utexas.edu

The Teton Range is a normal fault block that contains older reverse faults (Love et al., 1992). Although generally considered to be Late Cretaceous to early Tertiary structures, the timing, kinematic style, and history of these faults is conjectural. Faults include the Forellen Peak Fault to the north, the Buck Mountain Reverse Fault (BMRF) to the west and south, and the Teton normal fault to the east (Love et al., 1992). The BMRF is rooted in Precambrian crystalline rocks and dips steeply to the east about 60°. The fractured Cambrian Flathead sandstone, an orthoquartzite (90%+ quartz), rests nonconformably on the Precambrian. Its stratigraphic position and relative isotropic mineralogy make the Flathead an ideal horizon for studying brittle deformation.

Oriented Flathead hand samples were collected from the footwall of the BMRF along a partially overturned syncline (Figure 1). Continuous SEM-Cathodoluminescence (SEM-CL) scanlines of these samples allow for a systematic kinematic analysis of the cemented opening-mode fractures. We quantify attributes such as; geometry, spacing, orientation, and cross-cutting relationships. In isotropic rock, mode-I fractures primarily propagate along the plane perpendicular to  $S_{hmin}$ ; therefore, microfractures can be used to indicate paleostress trajectories, strain, and relative fracture timing (Anders et al., 2014; Hooker et al. 2018). Since fracture cements appear synkinematic, we've determined the temperatures, pressures, and fluid compositions present during fracturing by conducting a high-resolution fluid inclusion assemblage (FIA) petrographic and microthermometric analysis. Our kinematic and geochemical analysis of diagenetic damage zone features provides spatial and temporal constraints on the conditions present during fracture development, the evolution of the local tectonics, and paleohydrology.

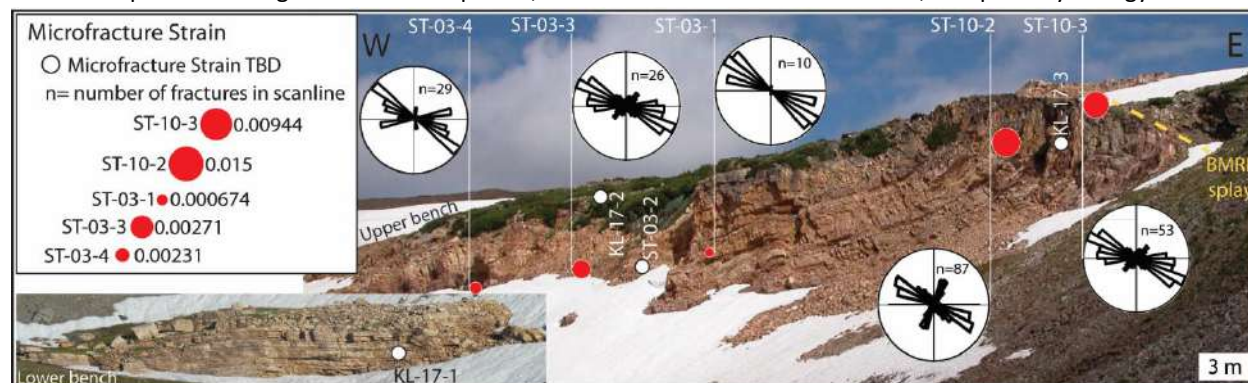


**Figure 1:** Flathead Sandstone syncline and fault at Kit Lake (43.716, -110.832). Sample locations, length-weighted fracture strike rose diagrams, and calculated total microfracture strain.

Steeply dipping fractures strike WNW, NW, and NE (Figure 1). In general, opening-mode fracture strain increases towards the fault and is highest near the fold axis. The strain calculation does not include the WNW and NE opening-mode fractures, prevalent nearest to the BMRF, which have undergone shear displacement. Fractures have opening displacements ranging from ~0.5  $\mu\text{m}$  to 3 mm. A few NW fractures contain quartz bridges and have preserved porosity. SEM-CL images of diagenetic cements reveal alternating light and dark luminescing textures; overgrowths are syntaxial and zoned whereas fractures contain wall-parallel crack-seal and wall-perpendicular fibrous textures, an indication of synkinematic cementation (Lander & Laubach, 2015). Fracture cements luminesce different colors under Color-SEM-CL, suggesting variation in fluid source and composition (Figure 2). Quartz overgrowths are crosscut by fractures and, therefore, formed early. The relative evolution of each brittle deformation period is supported by cross-cutting relationships and FIAs which reveal; WNW fractures formed first, followed by NW fractures, and lastly NE fractures.

The fluids present during overgrowth and fracture cementation are preserved in primary two-phase aqueous FIAs. Initial ice melting temperatures suggest cements precipitated from a  $\text{H}_2\text{O-NaCl-CaCl}_2(\pm\text{MgCl}_2)$ -type

fluid; however, only  $T_{mice}$  was observed. Therefore, we calculated salinity (expressed as wt% NaCl equivalent) assuming a H<sub>2</sub>O-NaCl fluid model (Steele-MacInnis et al., 2012). Within petrographic context, minimum trapping temperatures ( $T_h$ ) and salinity provide temporal

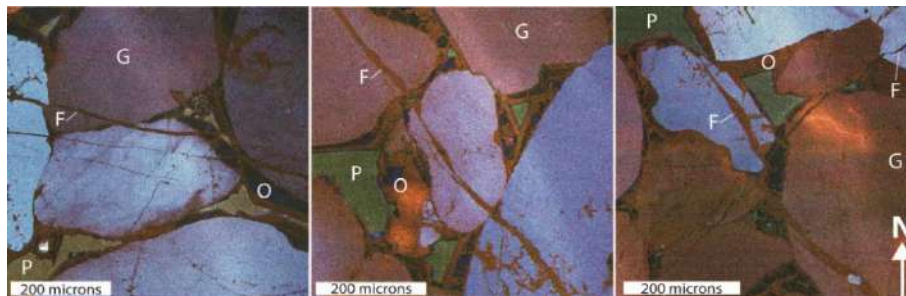


**Figure 2:** Color-SEM-CL images of WNW, NW, and NE striking fractures in sample ST-03-1A. G-grain; P-porosity; O-quartz overgrowth; F-fracture.

geochemical trends of deformation (Figure 3). Quartz overgrowths;  $T_h$ : 135-209°C and salinity: 4 to 7.5 wt.%. WNW-fractures;  $T_h$ : 140-170°C and salinity: 2.0-6.9 wt.%. NW fractures;  $T_h$ : 136-160°C and salinity: 11.7-13.5 wt.%. NE fractures;  $T_h$ : 110-191°C and salinity: 4.8-5.1 wt.%. On average,  $T_h$  ranges by 16.5°C within a single FIA.

Diagenetic cements precipitated from a wide range of fluid conditions. However, we can begin to temporally constrain fracture kinematics and fluid conditions present during diagenesis. Temperatures in quartz overgrowths show a heating trend which is compatible with progressive burial to maximum burial conditions. Cross-cutting relations and temperatures in fractures show a general cooling trend and suggest brittle deformation occurred after maximum burial, probably during uplift. Assuming fractures formed during tectonic shortening, orientations and cross-cutting relations suggest  $S_{Hmax}$  rotated from WNW to NW and finally to NE.

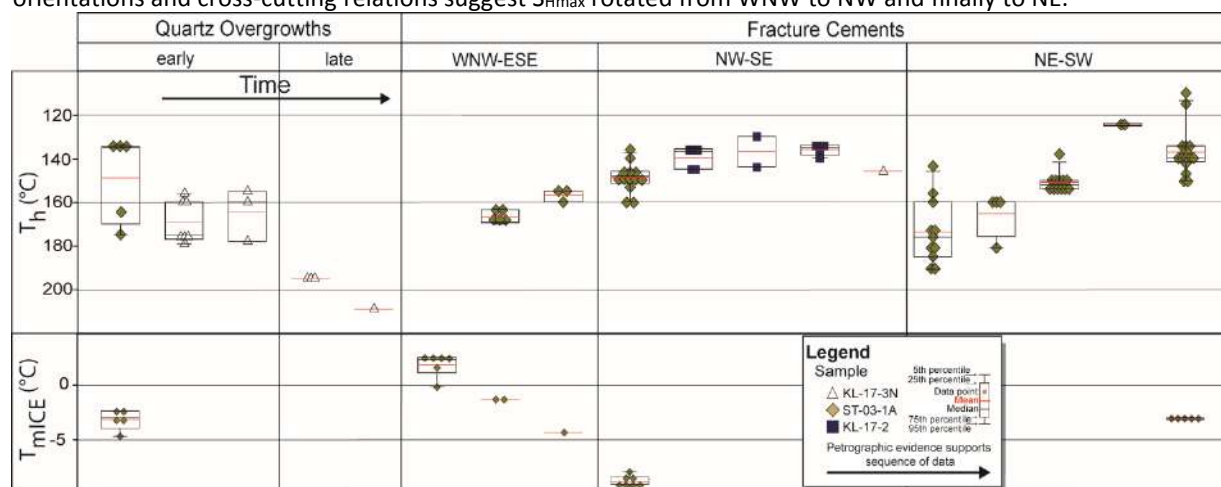


**Figure 3:** Fluid inclusion assemblage microthermometry results from quartz overgrowths and fractures. Cross-cutting relationships support the relative sequence (timing) of each diagenetic feature.

#### ACKNOWLEDGEMENTS

We are grateful to Grand Teton National Park for permission to sample under National Park Service permits GRTE-2014-SCI-0021 and GRTE-2017-SCI-0072.

#### REFERENCES

- Anders, M.H., Laubach, S.E., Scholz, C.H., 2014, Microfractures: a review. *J. Struct. Geol.* 69B, 377-394.
- Hooker, J.N., Laubach, S.E., Marrett, R., 2018, Microfracture spacing distributions and the evolution of fracture patterns in sandstones, *J. Struct. Geol.* 108, 66-79.
- Lander R.H., Laubach, S.E., 2015, Insights into rates of fracture growth and sealing from a model for quartz cementation in fractured sandstones. *Geol. Soc. Amer. Bull.* 127(3-4), 516-538.
- Love, J.D., Reed, J.C., Christiansen, A.C., 1992, Geologic map of Grand Teton National Park, Teton County, Wyoming; 1:62,500, USGS.
- Steele-MacInnis, M., Lecumberri-Sanchez, P., & Bodnar, R.J., 2012, HokieFlincs H<sub>2</sub>O-NaCl: A Microsoft Excel spreadsheet for interpreting microthermometric data from fluid inclusions based on the PVTX properties of H<sub>2</sub>O-NaCl, *Comp. Geosci.* 49, 334-337.

## **Invited – A new approach to understand natrocarbonatite formation based on melt and fluid inclusions from the Kerimasi volcano, Tanzania**

Tibor GUZMICS<sup>1</sup>, Márta BERKESI<sup>1</sup>, Ralf MILKE<sup>2</sup>, Csaba SZABÓ<sup>1</sup>

<sup>1</sup>*Lithosphere Fluid Research Lab, Eötvös Loránd University, Budapest, Hungary*

<sup>2</sup>*Institute of Geological Sciences, Freie Universität, Berlin, Germany*

*E-mail: tibor.guzmics@gmail.com*

The origin and evolution of natrocarbonatites at Oldoinyo Lengai volcano in East Africa has been the subject of debates for many years among petrologists, and there are still many questions left unanswered. A possible model for the formation of natrocarbonatite is by fractionation of calcite+apatite from a Ca-rich carbonate melt. However, no calciocarbonatite rocks have been found at Oldoinyo Lengai. A different model relates the formation of natrocarbonatites from a condensed fluid phase without the presence and contribution of any carbonate melt. In order to understand the genesis of this system we analyzed melt and fluid inclusion (MI and FI) from nephelinite, as these inclusions are the only direct means to study the carbonate melt and the fluid condensate potentially responsible for the formation of natrocarbonatites.

The Kerimasi volcano is located adjacent to Oldoinyo Lengai, where the nepheline phenocrysts from a nephelinite rock used in our study were collected from. The MI and FI occur along growth zones in nepheline, supporting their primary origin. Microthermometry and furnace experiments of the MI show entrapment temperature at ~850 °C. MI and FI petrography of the quenched material revealed the co-existence of an immiscible silicate melt, carbonate melt, and a fluid phase at this temperature, showing the typical appearance of heterogeneous entrapment (e.g., wide range in the volume percentages of the three phases in the inclusions).

As a consideration, composition of the three immiscible phases was estimated in our samples to see which one(s) could be the precursor of natrocarbonatite. Exposed silicate glasses and carbonate melts have been analyzed by electron microprobe. Concentrations of H<sub>2</sub>O and CO<sub>3</sub> have been calculated based on their Raman spectra. The FI have been analyzed by Raman spectroscopy combined with heating experiments. We also carried out FIB-SEM-EDS analyses on a previously Raman-imaged FI.

It is noteworthy to mention that none of the observed phases is dominated by H<sub>2</sub>O, even though many studies suggest that a H<sub>2</sub>O-rich environment is essential to attain natrocarbonatite composition. However, the carbonate melt is highly enriched in fluorine; both the silicate glass and the CO<sub>2</sub>-rich fluid contain significant amount of F. Fluorine could possibly be a key factor in understanding the carbonatite volcanism as the presence of this element suppresses the calcite liquidus, and maintains the carbonate melt in a liquid state near the eruption temperature of Na-carbonatites. This is supported by the lack of primary calcite in the rock. If so, then calcite fractionation cannot be responsible to reach natrocarbonatite composition in our samples. However, the carbonate melt alone is not a natrocarbonatitic melt.

The FI contains CO<sub>2</sub> vapor, natrite and nahcolite, as observed by detailed Raman spectroscopic imaging (Fig. 1). The natrite and nahcolite are assumed to be the result of fluid condensation. In addition, nahcolite is thought to be formed via sub-solidus chemical reaction of Na<sub>2</sub>CO<sub>3</sub> (natrite) + H<sub>2</sub>O + CO<sub>2</sub> = 2NaHCO<sub>3</sub> (nahcolite) at < 120 °C during cooling. This was

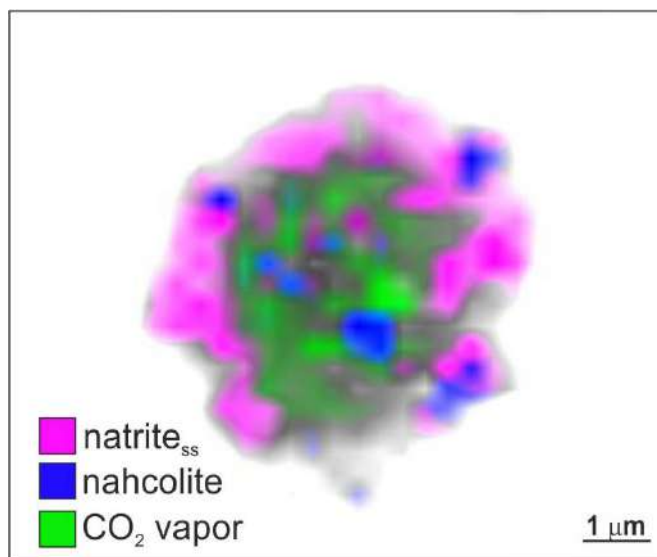


**Figure 1.** Raman-image of a nephelinite-coexisting fluid inclusion quenched from 850 °C. Natrite<sub>ss</sub> – natrite solid solution.

demonstrated by heating experiments on FI observed with Raman spectroscopy, where nahcolite dissociated < 200 °C, resulting in formation of natrite and CO<sub>2</sub>+H<sub>2</sub>O vapor phase within the FI. Upon further heating, natrite crystals melt forming a liquid phase, suggested by the rapid increase of the FWHM (Full Width at Half Maximum) of the highest intensity Raman band at around 1078 cm<sup>-1</sup>.

FIB-SEM-EDS analyses combined with Raman spectroscopy-based imaging of fluid condensates show an alkaline composition much like that of natrocarbonatites. Based on the composition of the MI and FI it is unlikely that the natrocarbonatite magma is originated from either the fluid or the carbonate melt equilibrated with nephelinite. We presume that once CO<sub>2</sub> and H<sub>2</sub>O outgassing takes place, the carbonate melt subsequently became miscible with a natrite-rich liquid. Therefore, the formation of the natrocarbonatite is likely due to the hybrid mixing of the degassed fluid and carbonate melt “endmembers”.

#### REFERENCES

- de Moore et al. (2013) Volatile-rich silicate melts from Oldoinyo Lengai volcano (Tanzania): Implications for carbonatite genesis and eruptive behavior, *Earth Planet. Sci. Let.*, 361, 379-390.
- Jago, Gittins. (1991) The role of fluorine in carbonatite magma evolution, *Nature*, 349, 56-58.
- Nielsen, Veksler. (2002) Is natrocarbonatite a cognate fluid condensate? *Contrib. Mineral. Petrol.*, 142, 425-435.
- Weidendorfer et al. (2017) A common origin of carbonatite magmas, *Geology*, 45, 507-510.

## Microthermometric and LA-ICP-MS measurements of hematite-hosted fluid inclusions reveal the temperature and composition of ore-forming fluids, Buckskin-Rawhide Mountains, western Arizona, USA

Jordan JENSEN<sup>1</sup>, Paulo COUTINHO<sup>1</sup>, Oscar LAURENT<sup>2</sup>, Jon SPENCER<sup>1</sup>, Matthew STEELE-MACINNIS<sup>3</sup>

<sup>1</sup>Department of Geosciences, University of Arizona, Tucson, Arizona, U.S.A.

<sup>2</sup>Institute for Geochemistry and Petrology, ETH, Zürich, Switzerland

<sup>3</sup>Department of Earth & Atmospheric Sciences, University of Alberta, Edmonton, Alberta, Canada

E-mail: [jljensen@email.arizona.edu](mailto:jljensen@email.arizona.edu)

The Buckskin-Rawhide detachment system in western Arizona, USA, hosts voluminous deposits of Fe and Mn oxides, including specular hematite. The presence of minor Cu and Fe sulfides suggests that mineralization occurred along redox interface that separated shallow, oxidizing fluids from deeper-seated, reducing fluids. Rapid exhumation along the main detachment fault during the Miocene likely provided the reducing, metal-bearing fluids a pathway for ascent toward more oxidizing conditions above (Spencer and Welty, 1986; Evenson et al., 2014). Wilkins et al. (1986) estimated that these fluids were ~225-325 °C. These temperature estimates were provided by microthermometry of quartz-hosted fluid inclusions, which are assumed to be coeval with nearby specular hematite mineralization. However, this assumption is not always valid, considering that quartz-hosted fluid inclusions can easily be modified by later recrystallization events (Lüders, 2016). In this contribution, we constrain the temperature and salinity of the Fe-bearing parent fluids by directly analyzing fluid inclusions hosted within hematite using infrared light (Fig. 1). Additionally, we use laser ablation inductively coupled plasma mass spectrometry (LA-ICP-MS) of hematite-hosted fluid inclusions to quantify the composition of Fe-bearing fluids. Hematite-hosted fluid inclusions yield minimum trapping temperatures of 284 °C to 315 °C, which overlap with homogenization temperatures from quartz-hosted fluid inclusions, implying that quartz and hematite mineralized concurrently. Hematite-hosted fluid inclusions indicate that mineralizing fluids were moderately saline, which is broadly consistent with microthermometric data from quartz-hosted fluid inclusions. Major solutes include Na, K, and Cl, with minor amounts of Cu, Zn, Sr, and Rb. Overall, these data provide the first quantitative estimate of ore-forming fluids that mobilized through the Buckskin-Rawhide detachment system.



**Figure 1.** Infrared light photomicrograph of two-phase fluid inclusions within Buckskin-Rawhide hematite.

### REFERENCES

- Evenson, N.S., Reiners, P.W., Spencer, J.E., and Shuster, D.L., 2014, Hematite and Mn oxide (U-Th)/He dates from the Buckskin-Rawhide detachment system, Western Arizona: Gaining insights into hematite (U-Th)/He system: *American Journal of Science*, v. 314, p. 1373–1435, doi: 10.2475/10.2014.01.
- Lüders, V., 2016, Contribution of infrared microscopy to studies of fluid inclusions hosted in some opaque ore minerals: possibilities, limitations, and perspectives: *Mineralium Deposita*, v. 91, p. 1462–1468, doi: 10.1007/s00126-016-0694-4.
- Spencer, J.E., and Welty, J.W., 1986, Possible controls of base- and precious- metal mineralization associated with Tertiary detachment faults in the lower Colorado River trough, Arizona and California (USA): *Geology*, v. 14, p. 195–198, doi: 10.1130/0091-7613(1986)14<195:PCOBAP>2.0.CO;2.



Wilkins, J., Beane, R. E., and Heidrick, T. L., 1986, Mineralization related to detachment faults: a model, in Beatty, B., and Wilkinson, P. A. K., editors, *Frontiers in geology and ore deposits of Arizona and the southwest*: Arizona Geological Society Digest, v. 16, p. 108–117.

## Liquid hydrocarbons in intracellular mineral precipitates in the vertebrae of a Jurassic marine reptile – animal or petroleum origin?

Jan Braly KIHLE<sup>1</sup>, Jørn Harald HURUM<sup>2</sup>, Lene LIEBE<sup>2</sup>

<sup>1</sup>Institute for Energy Technology, Kjeller, Norway

<sup>2</sup>Natural History Museum, University of Oslo, Oslo, Norway

E-mail: Jan.Kihle@ife.no

Two samples of a vertebra and a jawbone from two specimens of the Upper Jurassic carnivorous marine reptile *Pliosaurus funkei* from Spitsbergen have been described with respect to findings of fluorescing inclusions of liquid hydrocarbons (HCFI) hosted in mineral precipitates representing a former primary skeletal porosity (Fig. 1). Analyses were undertaken to elucidate potential animal and/or petroleum derivation(s) of the fluid(s) and possibly the timing of infilling with respect to the burial history of the hosting *Pliosaurus*. The HCFI temperature of homogenization ranges from 47 to 117°C. The earliest trapped fluids are primary aqueous inclusions occurring in calcite and barite close to the boundary to the skeletal matrix, followed by (or pene-contemporaneously with) isolated, bluish-fluorescing, primary petroleum inclusions in vicinity of the aqueous fluid inclusions in barite. These inclusions homogenize at the highest measured temperatures. Subsequently trapped hydrocarbons homogenize at lower temperatures as their density increases. Such observations of decreasing API (increasing density) with decreasing temperature may be related to secondary changes in migrated petroleum during earlier documented uplift at Spitsbergen. Biomarkers reflect a depositional condition for the Upper Jurassic shales, i.e., the source rock expelling petroleum was potentially the rock occurring just below the *Pliosaurus*-bearing strata. In addition to inclusions validating a petroleum origin, a few low-viscosity, reddish-brown colored inclusions, not likely to represent a bituminous liquid, are observed, potentially of an *animal* origin.



Figure 1. Representative images (white light and 365 nm UV) of samples and inclusions observed within.

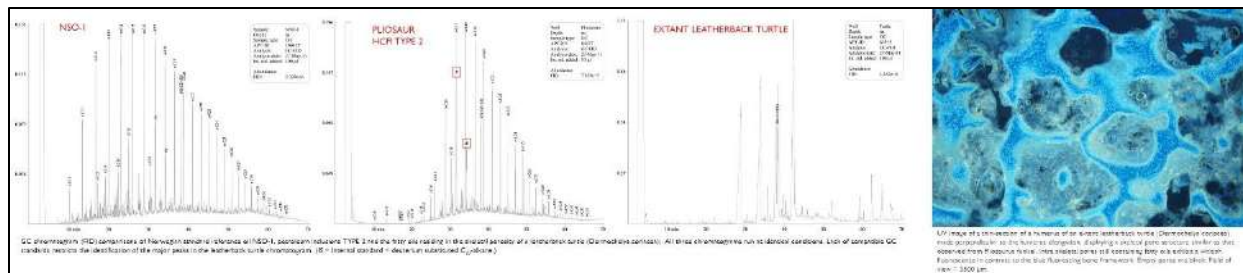


**Figure 2.** GC FID chromatograms of the extracted Pliosaurus fluid and two reference hydrocarbon fluids, including an UV micrograph of the skeletal porosity of a present-day leatherback turtle.

The combined applications of micro-thermometry and fluorescence spectroscopy on liquid hydrocarbons discovered as fluid inclusions trapped in Calcite and Barite crystals of the reptile backbone reveals a continuous lowering of minimum trapping temperature conditions as entrapment of denser petroleum progresses, indicative of a prolonged uplift scenario. The fluid composition of the most prominent type of trapped petroleum (TYPE 2) is indicative of an Upper Jurassic source rock buried to a maximum of 2300-2500 m depth. The presence of the Phytane biomarker in this GC chromatogram (Fig. 2) however exclude a marine origin of the TYPE 2 hydrocarbons, since this biomarker originates from chlorophyllic precursors only.

The presence of a few anomalous hydrocarbon fluid inclusions TYPE 3 differing from commonly occurring TYPE 1 or TYPE 2 petroleum inclusions *may* nevertheless contain remnants of an animal origin. A careful preparative isolation of fluid inclusion chips containing TYPE 3 inclusions should be made, to be followed by controlled fluid inclusion decrepitation directly into a GC-MS. Chromatograms and biomarker analysis of TYPE 3 fluid inclusions may subsequently be compared to the signatures of leatherback turtles, the closest living relative to the Pliosaurus, bearing in mind that biomarkers are de-functionalized and not identical to what is found in living matter. An absence of the biomarker Phytane in the TYPE 3 GC-MS chromatograph would hence point towards the fact that these anomalous inclusions represent the oldest oil or fat from *an animal origin* yet known to man.

REFERENCES

Coghlan, A. (2009) Fossil of 'ultimate predator' unearthed in Arctic.  
<https://www.newscientist.com/article/dn16785-fossil-of-ultimate-predator-unearthed-in-arctic>  
 Knutsen, E.M., Druckenmiller, P.S. & Hurum, J.H. (2012) A new species of Pliosaurus (Sauropterygia: Plesiosauria) from the Middle Volgian of central Spitsbergen, Norway. Norwegian Journal of Geology, Vol 92, pp. 235-258.

## P-T paths of H<sub>2</sub>O-NaCl fluid inclusions during heating to the homogenization temperature

Yury I KLYUKIN, Robert J. BODNAR

Fluids Research Laboratory, Department of Geosciences, Virginia Tech, Blacksburg, Virginia, U.S.A.

E-mail: yury84@vt.edu

One of the fundamental properties of fluid inclusions (FI) is the homogenization temperature ( $T_H$ ). The homogenization temperature represents the minimum temperature of trapping of fluid inclusions, and also represents the starting PT point of the isochore (line of constant density or volume) corresponding to the FI density. While the PT path followed by the FI following homogenization is straightforward and is constrained to lie along the isochore, some confusion exists concerning the PT path followed by the FI during heating from ambient temperature to  $T_H$ . Because FI represent constant volume, constant composition systems, the PT path followed by the FI during heating to the homogenization temperature may be constrained based on mass balance calculations involving the PVTX properties of the appropriate fluid system, as described by Bodnar (1983). Here, we describe the path followed by FI represented by the system H<sub>2</sub>O-NaCl.

The bulk density of the FI ( $\rho_{BLK}$ ) is calculated at the homogenization temperature ( $T_H$ ) and the pressure on liquid + vapor curve ( $P_{L+V}$ ) corresponding to the salinity of the FI ( $X_{BLK}$ ). The total mass of H<sub>2</sub>O plus NaCl in a FI ( $m_{BLK}$ ) of unit volume is then defined as  $m_{BLK} = \rho_{BLK} \cdot V_{BLK}$  (eq. 1), where  $V_{BLK}$  represents the unit volume of the FI. The mass fraction of NaCl in the FI ( $X_{BLK}$ ) is calculated from the known salinity as is defined as  $m_{NaCl} = m_{BLK} \cdot X_{BLK}$  (eq. 2). At temperatures,  $T_x$ , below  $T_H$ , the FI contains a low salinity vapor phase and a higher salinity liquid phase with masses  $m_V$  and  $m_L$ , respectively, and salinities  $X_V$  and  $X_L$  for each phase. The bulk mass of the FI can be expressed as  $m_{BLK} = m_L + m_V$  (eq. 3), while the mass of NaCl in the FI is defined as  $m_{NaCl} = m_L \cdot X_L + m_V \cdot X_V$ , (eq. 4). The mass of the liquid phase can be expressed from Eq. 4 as  $m_L = (m_{NaCl} - m_V \cdot X_V) / (X_L - X_V)$  (eq. 5), where  $(m_{BLK} - m_L)$  represents the substitution of  $m_V = m_{BLK} - m_L$  (eq. 6) from eq. 3. After rearrangement, the mass of the liquid phase can be calculated according to:  $m_L = (m_{NaCl} - m_{BLK} \cdot X_V) / (X_L - X_V)$  (eq. 7). The mass of the vapor phase then can be calculated from eq. 6.

The volume of the FI,  $V_{BLK}$ , remains constant and can be calculated according to:  $V_{BLK} = m_L / \rho_L + m_V / \rho_V$  (eq. 8), where  $\rho_L$  and  $\rho_V$  are the density of liquid and vapor phases, evaluated at temperature  $T_x$ , the salinity of  $X_L$  and  $X_V$  and pressure in FI  $P_x$ . To maintain a constant volume,  $V_{BLK}$ , at all temperatures  $T_x < T_H$ , the pressure  $P_x$  must be less than the pressure on the liquid-vapor curve for the FI bulk salinity,  $P_{L+V}$ , calculated at each temperature,  $T_x$ , and salinity,  $X_{BLK}$ . At each temperature,  $T_x$ , the pressure,  $P_x$ , is decreased incrementally, starting at the pressure on the liquid-vapor coexistence curve. At each new pressure,  $P_x$ , the salinities and densities of the liquid and vapor phases are calculated, and this information is used to estimate  $V_{BLK}$  at each pressure,  $P_x$ , until the appropriate pressure at which the salinities and densities of the coexisting liquid and vapor phases satisfy the mass balance constraints described above.

The approach described above is illustrated using an example FI with 10 wt. % NaCl salinity, with  $T_H$  of 350 °C and unit volume,  $V_{BLK}$ , of 1 cm<sup>3</sup> (Note that the actual volume assumed for the FI does not affect the results). Properties of H<sub>2</sub>O-NaCl fluid phases, calculated using the SoWat model of Driesner (2007) and Driesner & Heinrich (2007), were combined in an MS Excel VBA macro (Klyukin et. al, in prep). The  $T_x$  range for the model varies from 101 °C to  $T_H$ , due to the 1 bar lower pressure limit of the SoWat model.

The liquid + vapor curve for 10 wt. % NaCl is shown in Fig. 1A, with homogenization temperature  $T_H$  and isochore for the FI shown by the dashed line labeled  $\rho_{FI}$ . At pressures below the L+V curve, two phases exist in equilibrium. The difference  $P_x - P_{L+V}$ , defined as LV pressure decrement, is shown in Fig. 1B. The decrease in the size of the bubble in the FI with each degree of temperature change is larger at higher temperatures, as shown by the relative change in bubble volume with temperature (Fig. 1C). The vapor phase salinity,  $X_V$ , increases with increasing temperature, while the salinity of liquid phase,  $X_L$ , reaches a maximum at about 300 °C and then asymptotically approaches 10 wt. % NaCl as the mass of fluid in the vapor phase approaches zero at low temperatures (Fig. 1D). The absolute masses of the liquid ( $m_L$ ) and vapor ( $m_V$ ) phases show opposite trends, with an inflection point at ~300 °C (Fig. 1E). Figures 1F and 1G show variations in density and volume for both phases in the FI at various temperatures.

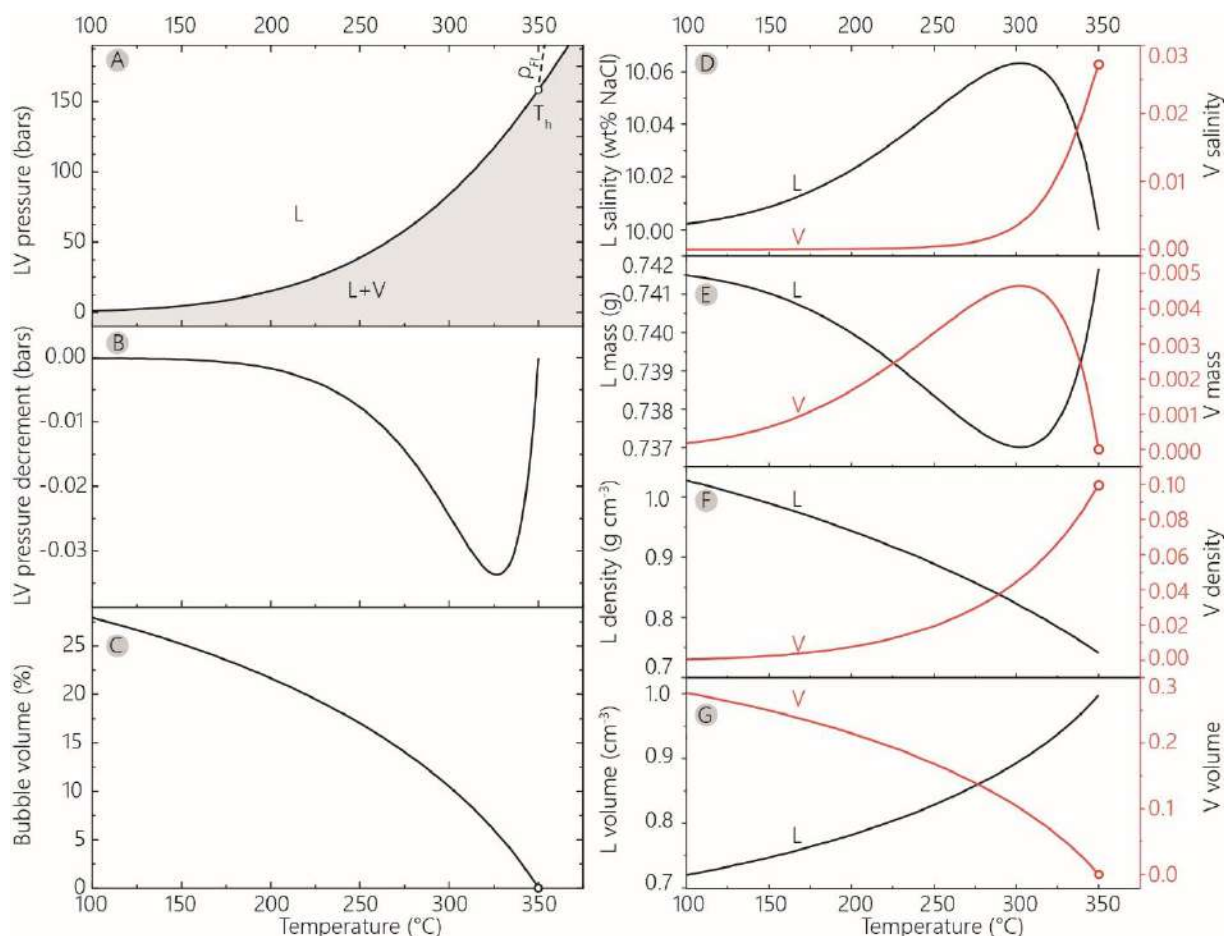


**Figure 1.** Variations in liquid (L) and vapor (V) phases of a fluid inclusion as a function of temperature for an inclusion that homogenizes to the liquid phase at 350 °C and has a salinity of 10 wt. % NaCl. A) L+V phase diagram for 10 wt. % NaCl, indicating homogenization point ( $T_H$ ) and isochores ( $\rho_{FI}$ ) of the FI. Grey area indicates PT region where only L+V phases can coexist in equilibrium. B) difference between pressure in FI ( $P_x$ ) and pressure on the L+V curve at that same temperature; C) volume percent vapor in FI; salinity (D), mass (E), density (F) and volume (G) of L and V phases at temperatures  $T_x \leq T_H$ .

#### REFERENCES

- Bodnar, R. J. (1983). A method of calculating fluid inclusion volumes based on vapor bubble diameters and P-V-T-X properties of inclusion fluids, *Economic Geology*, 78(3), 535-542.
- Driesner, T. (2007). The system H<sub>2</sub>O-NaCl. II. Correlations for molar volume, enthalpy, and isobaric heat capacity from 0 to 1000 °C, 1 to 5000 bar, and 0 to 1 X-NaCl, *Geochimica et Cosmochimica Acta*, 71(20), 4902-4919.
- Driesner, T., & Heinrich, C. A. (2007). The system H<sub>2</sub>O-NaCl. I. Correlation formulae for phase relations in temperature-pressure-composition space from 0 to 1000 °C, 0 to 5000 bar, and 0 to 1 XNaCl, *Geochimica et Cosmochimica Acta*, 71(20), 4880-4901.

## Invited – Rates of serpentinization in pyroxene micro-reactors

Hector LAMADRID, Zoltán ZAJACZ

Department of Earth Sciences, University of Toronto, Toronto, Ontario, Canada

E-mail: hm.lamadrid@utoronto.ca

Serpentinization is a critical geologic process that occurs when ultramafic minerals (mantle rocks) interact with aqueous fluids. The chemical and petrological processes that accompany serpentinization and the interactions between the ocean and the oceanic lithosphere have become some of the most important subjects in the scientific literature, and are key to understand the physical, chemical and biological evolution of the Earth's system (Kelley et al. 2001). They are also central to current origin of life hypotheses (Martin et al. 2008), as well as the search for microbial life on the icy moons of Jupiter and Saturn (Vance et al. 2016).

Despite the pivotal role that serpentinization plays in a number of geological and biological processes, few experimental studies have attempted to determine the rates of serpentinization reactions, and the rates that have been reported diverge widely (McCollom et al. 2016). Moreover, the specifics on how the environmental factors (like temperature, fluid composition,  $fO_2$ , salinities, etc.) control the serpentinization reactions of olivine are not completely understood, and in the case of pyroxene almost nonexistent. Recent studies on rates of serpentinization using a novel *in situ* experimental technique using micro-reactors (Lamadrid, 2016; Lamadrid et al. 2017; Lamadrid et al., *in prep.*) have shown that the serpentinization reaction of olivine is sensitive to the fluid composition and salinity and even small increases in salinity and addition of  $Mg^{2+}$  and  $CO_2$  to the fluid slows down the reaction by several orders of magnitude.

Here we show partial results on the application of the micro-reactor technique on gem quality enstatite crystals as a function of temperature and salinity using piston cylinder experiments to trap synthetic fluid inclusions (SFI).

The micro-reactors are synthetic fluid inclusions (SFI) used to monitor the hydration reaction (hydrolysis) of ultramafic minerals by measuring changes in the internal composition of the fluid. The experimental technique uses two steps. First, we trapped SFI with aqueous fluids with different salinities ( $H_2O$ -NaCl 3.5 and 10 wt% eq. NaCl) in pyroxene at elevated P-T where the minerals were in equilibrium with the fluids. The P-T selected to trap the SFI (12 to 5 Kbar at 1000 °C) was such that the internal pressure of the inclusion at the serpentinization temperature of pyroxene (200 to 450 °C) would be ~500 bars. Then, after detailed petrographic investigation, wafers of the crystals were set at temperatures allowing serpentinization of pyroxene and monitored every 5 to 20 days. After a few days of reaction time, small clusters of secondary minerals (serpentine + talc ± magnetite) formed inside the SFI (Figure 1). Reaction progress was monitored by low temperature microthermometry measuring the changes in the salinity of the SFI as a proxy of the amount of  $H_2O$  consumed by the reaction  $enstatite + H_2O = serpentine + talc$ .

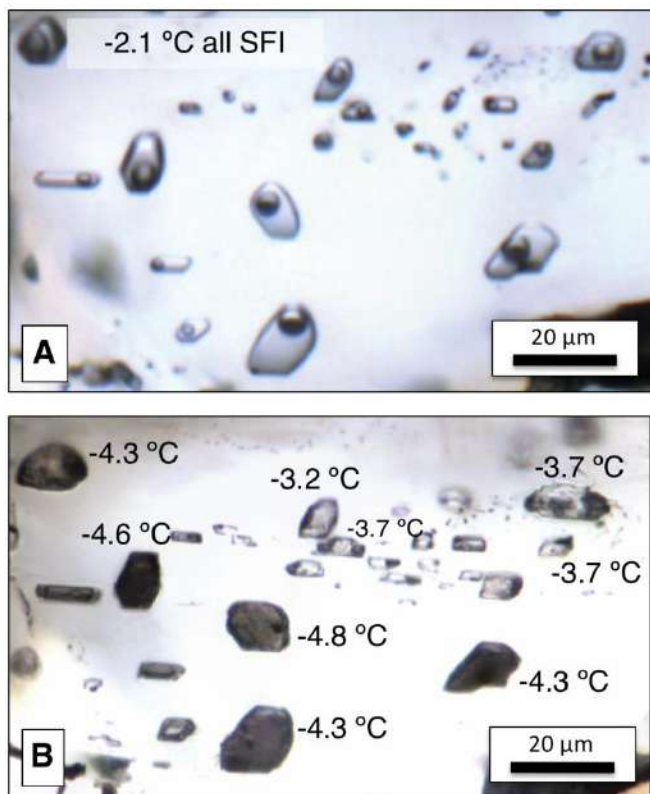


**Figure 1.** Photomicrograph of SFI in pyroxene before (A) and after (B) 10 days of the serpentinization experiment. The reaction products inside the inclusions are serpentine (brown-green), talc (white) and magnetite (black).

Preliminary results show that the serpentinization rates of pyroxene are faster than those of olivine at higher temperatures (300-400 °C) where serpentinization of olivine becomes sluggish. The maximum rates obtained at 400 °C which represents an offset of 150 °C with the maximum serpentinization rates of olivine (Figure 2). The micro-reactor technique used in this study is a powerful tool to monitor fluid-rock reactions *in situ* and in real time and can be applied to a wide variety of host minerals, reaction products, temperatures and different starting fluid compositions.

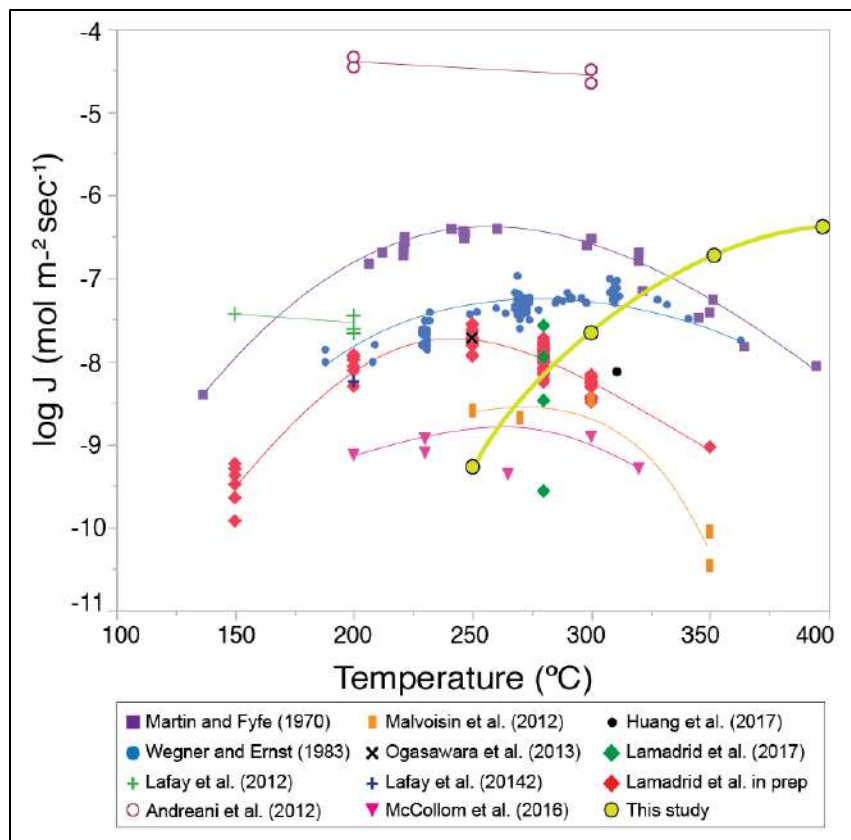


**Figure 2.** Comparison of the serpentinization rates of olivine with the preliminary results of this study (light green).

#### REFERENCES

- Kelley D. et al. (2001) An off-axis hydrothermal vent field near the Mid-Atlantic Ridge at 30 degrees N. *Nature* 412, 145–149.
- Martin W. et al. (2008) Hydrothermal vents and the origin of life. *Nat Rev Microbiol* 6, 805.
- Vance S. D. et al. (2016) Geophysical controls of chemical disequilibria in Europa. *Geophys Res Lett* 43, 4871–4879.
- McCollom et al. (2016) Temperature trends for reaction rates, hydrogen generation, and partitioning of iron during experimental serpentinization of olivine. *Geochim Cosmochim Acta* 181, 175–200.
- Lamadrid H.M. (2016) Published Ph.D. Dissertation, Virginia Tech.
- Lamadrid H.M. et al. (2017) Effect of water activity on rates of serpentinization of olivine. *Nat Commun.* 8, 16107.
- Lamadrid H.M. et al. Effect of temperature and fluid composition on rates of serpentinization of olivine. In preparation.

## Keynote – Genetic relationship between mineral paragenesis, fluid chemistry and fluid source in a tungsten vein deposit: Panasqueira

Pilar LECUMBERRI-SANCHEZ<sup>1</sup>, Christoph A. HEINRICH<sup>2</sup>, Markus WÄLLE<sup>2,3</sup>, Marta CODEÇO<sup>4</sup>, Phillip WEIS<sup>4</sup>, Marta SOŚNICKA<sup>4</sup>, Filipe PINTO<sup>5</sup>

<sup>1</sup>Department of Earth & Atmospheric Sciences, University of Alberta, Edmonton, Alberta, Canada

<sup>2</sup>Institute für Geochemie und Petrologie, ETH Zurich, Switzerland

<sup>3</sup>Earth Sciences Department, Memorial University of Newfoundland, Canada

<sup>4</sup>Inorganic and Isotope Geochemistry, GFZ German Research Centre for Geosciences, Potsdam (Germany)

<sup>5</sup>Institute of Earth Sciences (ICT), Pole of University of Porto, Portugal

E-mail: lecumber@ualberta.ca

Panasqueira is a world-class tungsten-vein deposit. Several paragenetic stages have been proposed (Polya et al., 2000) including two pre-ore stages (crack-seal quartz-seam, and muscovite selvages); and four ore stages (main oxide-silicate stage, main sulfide stage, pyrrhotite alteration stage, and late carbonate stage).

In this study, compositions of the mineralizing fluids at Panasqueira have been determined through combination of detailed petrography, microthermometric measurements and LA-ICP-MS analyses. We have identified the fluids related to several mineralizing stages in the system.

Three fluid generations recorded in pseudo-secondary to secondary fluid inclusions have been identified at Panasqueira and their chemical composition has been characterized. The first fluid generation identified in quartz and wolframite consists of CO<sub>2</sub>-bearing fluid inclusions with homogenization temperatures ranging between 260 and 320 °C and salinities between 5 and 8 eq. wt% NaCl. Petrographic constraints indicate that this first generation (1) is paragenetically related to the main oxide-silicate stage. This stage (1) was likely trapped under high pressures and lithostatic conditions. Two lower-temperature CO<sub>2</sub>-absent fluid generations (2a and 2b) have been identified in quartz and are represented by secondary fluid inclusions postdating the main oxide-silicate stage. Generation (2a) consists of high-salinity (20-30 eq. wt% NaCl) fluids with homogenization temperatures ranging between 180°C and 250°C. Generation (2b) consists of low-salinity (<2 wt %) low homogenization temperature (100-150°C) fluid inclusions. Conclusive petrographic evidence of the relationship between these two late-stage fluid generations and specific late mineral stages are scarce. However, fluid compositions suggest that generation (2a) is related to the main sulfide stage and generation (2b) is related to the late carbonate stage.

The fluids at Panasqueira show a PTX evolution from an early magmatic-like chemical signature in good agreement with isotopic data (Codeço et al., 2017) to a signature that seems to indicate an influx of non-magmatic fluids at least in the latest stages of mineralization (late carbonate stage).

### REFERENCES

- Codeço, M. et al. (2017) Chemical and boron isotopic composition of hydrothermal tourmaline from the Panasqueira W-Sn-Cu deposit, Portugal, *Chemical Geology* 468, 1-16
- Polya, D.A. et al. (2000) Evolution and paragenetic context of low  $\delta$ D hydrothermal fluids from the Panasqueira W-Sn deposit, Portugal: New evidence from microthermometric, stable isotope, noble gas and halogen analyses of primary fluid inclusions, *Geochimica et Cosmochimica Acta* 64, 3357-3371.



## Fluid inclusion characteristics at the El Hammam REE-rich fluorite deposit

Pilar LECUMBERRI-SANCHEZ<sup>1</sup>, M. BOUABDELLAH<sup>2</sup>, O. ZEMRI<sup>2</sup>

<sup>1</sup>*Department of Earth & Atmospheric Sciences, University of Alberta, Edmonton, Alberta, Canada*

<sup>2</sup>*Department of Geosciences, Mohammed Premier University, Oujda, Morocco*

*E-mail: lecumber@ualberta.ca*

Low-temperature (100–160 °C) hydrocarbon-bearing brines mobilize REE at concentrations up to several thousand ppm total rare earth elements ( $\Sigma$ REE) at El Hammam, Morocco. The major element chemistry (Na, Ca, Mg) and temperature of the fluids in this system are consistent with those of oil field brines. In contrast, REE concentrations in the fluid suggest a significant element input from a magmatic source. Spatially related lamprophyres predating the formation of El Hammam share a similar trace element signature. Therefore, hydrocarbon-bearing basinal brines seem to have leached some of these elements through fluid–rock interaction from the lamprophyres, supporting the ability of oil-field brines to mobilize not only base metals (as in Mississippi Valley Type [MVT] deposits), but also rare earth elements.

The stability constants of REE aqueous complex at temperatures of 100–160 °C, the chemistry of oil-field brines worldwide, and the partitioning behavior of REE between fluorite and water at El Hammam indicate that acetate ( $\pm$  carbonate and fluoride) are likely to be major contributors to REE mobilization in these settings. The direct implications of the low temperature transport of REE by oil-bearing brines is that, in systems where these kind of fluids occur, the REE signature observed may not reflect the source of the fluid as much as a combination of fluid source and fluid–rock interaction. In addition, oil-field brines can efficiently scavenge, transport, and deposit REE leading to anomalously high accumulations such as the El Hammam fluorite deposit and may also contribute to REE mobilization and concentration in other systems.



## Application of fluid inclusions to study low-temperature diagenesis in Miocene carbonates, La Molata, SE Spain

Zhaoqi LI<sup>1,2</sup>, Robert GOLDSTEIN<sup>2</sup>, Evan FRANSEEN<sup>2,3</sup>

<sup>1</sup>CGG, Houston, Texas, U.S.A.

<sup>2</sup>Department of Geology, the University of Kansas, Lawrence, Kansas, U.S.A.

<sup>3</sup>Kansas Geological Survey, Lawrence, Kansas, U.S.A.

E-mail: zhaoqili83@gmail.com

Carbonate rocks are susceptible to diagenetic alterations, which could significantly modify the pore system and rock properties. As carbonate platforms commonly aggrade into shallow water, early influx of meteoric fluids is to be expected. The introduction of meteoric waters into carbonate systems can form two distinct diagenetic low-temperature environments, including mixing-zone and freshwater environments. This study investigated the diagenetic effect on porosity and permeability in an Upper Miocene carbonates in SE Spain, by integrating petrography, core analysis, fluid inclusions, and stable isotopes of carbon and oxygen.

Mixing of fluids from freshwater and seawater has been proposed as one of the mechanisms for dolomitization since previous studies of low-temperature dolomites (Hanshaw et al. 1971; Land 1973). After their initial work, many researchers invoked mixing-zone dolomitization model to explain dolostones that lack evaporates association (e.g., Land et al. 1975; Humphrey 1988). Criticisms of this model, however, have continued since the 1980s (Machel and Mountjoy 1986). Reexamination of some of the classic examples of mixing-zone dolomite have shown that they did not form in mixing zones, but either formed from seawater followed by partial alteration (recrystallization) in freshwater, or resulted from hydrothermal fluids (Land 1991; Machel and Burton 1994). In addition, numerous studies have shown that modern and ancient mixing zones lack pervasive dolomite. In light of these studies, many have suggested that the mixing-zone dolomitization model should no longer be considered viable. This study proposed a new model of dolomitization from mixing by ascending freshwater with mesohaline marine waters. In Study area, dolomitization occurred at the end of the Miocene, but before Pliocene deposition. Dolomite occurs as replacement and cement; both have well-preserved CL zonations. Fluid inclusion Tm ice values range from -0.2 to -2.3 °C (Fig. 1), indicating fluid mixing of freshwater and evaporated seawater.  $\delta^{18}\text{O}$  and  $\delta^{13}\text{C}$  are characterized by positive covariation, with +0.9 to +6.0‰ VPDB for  $\delta^{18}\text{O}$ , and -4.5 to +3.0‰ VPDB for  $\delta^{13}\text{C}$ . Lower stratigraphic units are more depleted in  $\delta^{18}\text{O}$  and  $\delta^{13}\text{C}$  compared to upper stratigraphic units.  $^{87}\text{Sr}/^{86}\text{Sr}$  values (0.70866 to 0.70904) range from less than to greater than that of late Miocene seawater values. All data are consistent with injection of freshwater into the carbonates from below. Upward flow of meteoric waters, driven by hydraulic head from the hinterland, creates fluid mixing and leads to loss of pressure and degassing of  $\text{CO}_2$ . This ascending freshwater-mesohaline mixing is responsible for dolomitization at La Molata, and may be applicable to Miocene dolomitization around the western Mediterranean. The model can also be applied to carbonate systems adjacent to paleotopographic highs, where freshwater discharges into slightly evaporated seawater.

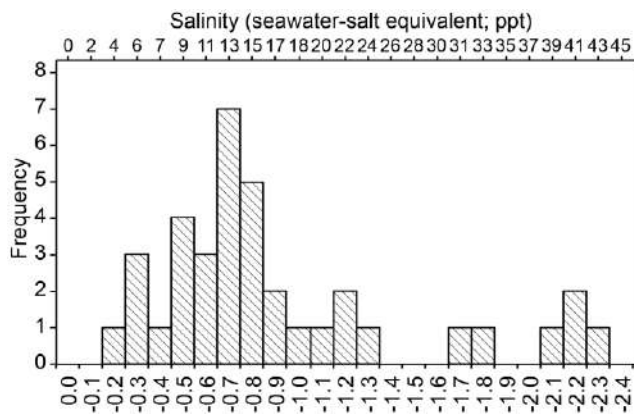


**Figure 1.** Frequency histogram showing distribution of Tm-ice measurements of primary fluid inclusions in dolomite. Tm-ice below -1.9° indicates evaporation, and above -1.9° indicates involvement of freshwater.

After dolomitization, long periods of subaerial exposure have resulted in extensive calcite cementation. While modern carbonate sediments typically have high porosity values of 40 to 70% (Enos and Sawatsky, 1981), ancient carbonate rocks commonly only have a few percent porosity (Choquette and Pray, 1970). Though porosity could be reduced from mechanical compaction during burial, many studies have shown that reduction of porosity and permeability can be attributable to early meteoric cementation (e.g., Goldstein, 1988; Moss and Tucker, 1995). Few studies, however, provide quantitative data on the controls that determine where meteoric calcite cementation

is important, and what effect it has on porosity and permeability. The second purpose of this work is to investigate calcite cementation in study area. This study shows the carbonate succession has an upper and a lower zone of extensive calcite cementation; each zone boundary cuts across the stratigraphy. Cement textures suggest phreatic conditions. Cement in each of the two zones has a unique cathodoluminescence signature. Cement in the upper cemented zone has two meteoric calcite lines with  $\delta^{18}\text{O}$  at -5.1 ‰ and -5.8 ‰ VPDB, whereas the lower cemented zone is at -6.7 ‰ VPDB.  $\delta^{13}\text{C}$  for both are predominantly negative values, ranging from -10 to +2 ‰ PDB, suggestive of soil-gas. Measurements of  $T_m$  ice in primary fluid inclusions yield a mode of 0.0 °C in both zones, indicating calcite cementation from fresh water (Fig. 2). The upper cemented zone pre-dated the lower cemented zone on the basis of known relative sea-level history. These two zones are associated with the positions of two different paleo-water tables of different ages that formed during relative sea-level fall and erosional downcutting of the landscape during the Plio-Pleistocene. Meteoric calcite cementation reduced porosity and permeability, but measured values are inconsistent with simple filling of open pore space. There are different relationships between percent calcite cement and porosity/permeability for each lithofacies. Distribution of cements may be predictable on the basis of known sea-level history. The cementation can be incorporated into subsurface geomodels by defining surfaces that separate cemented zones from uncemented zones, and applying lithofacies specific relationships between cementation, porosity and permeability.

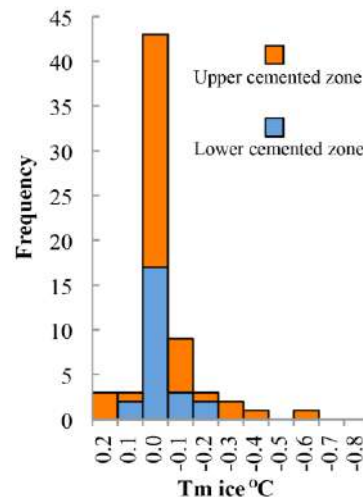


**Figure 2.** Frequency histogram showing distribution of  $T_m$ -ice measurements of primary fluid inclusions in calcite cements.

#### REFERENCES

- Choquette, P.W., and Pray, L.C., 1970, Geologic nomenclature and classification of porosity in sedimentary carbonates: AAPG bulletin, v. 54, p. 207-250.
- Enos, P., and Sawatsky, L., 1981, Pore networks in Holocene carbonate sediments: Journal of Sedimentary Research, v. 51, p. 961-985.
- Goldstein, R.H., 1988, Cement stratigraphy of Pennsylvanian Holder Formation, Sacramento Mountains, New Mexico: AAPG Bull, v. 72, p. 425-438.
- Hanshaw, B.B., Back, W., and Deike, R.G., 1971, A geochemical hypothesis for dolomitization by ground water: Economic Geology, v. 66, p. 710-724.
- Humphrey, J.D., 1988, Late Pleistocene mixing zone dolomitization, southeastern Barbados, West Indies: Sedimentology, v. 35, p. 327-348.
- Land, L., 1991, Dolomitization of the Hope Gate Formation (north Jamaica) by seawater: reassessment of mixing-zone dolomite, in Taylor, H.P., O'Neil, J.R., and Kaplan, I.R., eds., Stable Isotope Geochemistry: A Tribute to Samuel Epstein: The Geochemical Society (London), Special Publication 3, p. 121-130.
- Land, L., Salem, M., and Morrow, D., 1975, Paleohydrology of ancient dolomites: geochemical evidence: American Association of Petroleum Geologists Bulletin, v. 59, p. 1602-1625.
- Land, L.S., 1973, Holocene meteoric dolomitization of Pleistocene limestones, North Jamaica: Sedimentology, v. 20, p. 411-424.
- Machel, H.G., and Burton, E.A., 1994, Golden Grove dolomite, Barbados; origin from modified seawater: Journal of Sedimentary Research, v. A64, p. 741-751.
- Machel, H.G., and Mountjoy, E.W., 1986, Chemistry and environments of dolomitization - a reappraisal: Earth-Science Reviews, v. 23, p. 175-222.
- MOSS, S., and TUCKER, M.E., 1995, Diagenesis of Barremian-Aptian platform carbonates (the Urgonian Limestone Formation of SE France): near-surface and shallow-burial diagenesis: Sedimentology, v. 42, p. 853-874.

## Origin of CO<sub>2</sub>-rich Zechstein-2-Carbonate-hosted gas reservoirs in the Lower Saxony Basin, NW Germany

Volker LÜDERS<sup>1</sup>, Johannes SCHOENHERR<sup>2</sup>, Marta SOŚNICKA<sup>1</sup>

<sup>1</sup> GFZ German Research Centre for Geosciences, Potsdam, Germany

<sup>2</sup> ExxonMobil Production Deutschland GmbH, Hannover, Germany

E-mail: volue@gfz-potsdam.de

Uneconomically high CO<sub>2</sub> contents (up to nearly 100%) have been encountered by some exploration wells in the southern Zechstein-2-Carbonate (Ca<sub>2</sub>) fairway of the LSB. This part of the LSB is characterized by unusual high maturity of organic matter and Upper Carboniferous coals suggesting an abnormal high paleo heat-flow. The origin of high heat-flow during the Jurassic/Early Cretaceous has given rise for much debate during the past decades and is still discussed controversy. Several authors favor intrusions of deep-seated magmatic bodies (Bramsche-, Vlotho-, Uchte Massif, etc.) of Lower Cretaceous age in order to explain the thermal overprint of organic matter which differs significantly in R<sub>o</sub> values (up to 6%) from similar facies in other parts of the LSB (e.g. Stadler and Teichmüller 1971). In this context, a magmatic origin of CO<sub>2</sub> in some reservoirs the Uchte study area was discussed. Quite contrary numeric modeling relates high maturation to a model that invokes deep burial from the Upper Jurassic to Lower Cretaceous followed by inversion and subsequent erosion of a thick sediment column during the Late Cretaceous through Tertiary. However, there is a considerable uncertainty how thick the eroded column really was. Numeric modeling (e.g. Petmecky et al. 1999; Bruns et al. 2015) suggests several thousand meters of erosion in the central part of the LSB. Following this idea, Fischer et al. (2006) proposed a model for the formation of high CO<sub>2</sub> Zechstein-2 carbonate gas reservoirs that proposes pressure-induced CO<sub>2</sub> release from Ca<sub>2</sub> reservoir rocks during stages of deep burial and mixing with early organic-derived CO<sub>2</sub>. However, as pointed out by Brown (1999) decarbonation of carbonates (excluding calcite) requires temperatures >300°C and even higher temperatures for thermal decomposition of calcite in the absence of aluminosilicates.

The aim of this study was to trace the origin of CO<sub>2</sub> in the so-called “CO<sub>2</sub> province” in the southern Zechstein-2 carbonate (Ca<sub>2</sub>) fairway in of the Lower Saxony Basin (LSB) and to attempt predicting the migration pathways and the occurrence of high CO<sub>2</sub> accumulations in so far undrilled Ca<sub>2</sub> reservoir blocks. This was done by the combination of studies of fluid inclusion hosted in fracture-fill mineralization and structural analyses.

For this purpose, more than 370 fracture-fill mineralization (quartz, fluorite, carbonates, anhydrite) hosted by Devonian, Upper Carboniferous strata or Zechstein carbonate were sampled from 54 wells and inspected for fluid inclusion inventory. Besides highly-saline aqueous 2-phase (L+V) and 3-phase (L+V+H) many samples also contain differently composed gaseous inclusions. CO<sub>2</sub>-rich inclusions are abundant in fracture filling calcite hosted by Devonian limestone. CH<sub>4</sub>-CO<sub>2</sub>-(N<sub>2</sub>) inclusions (locally with CO<sub>2</sub> content of more than 80 mol%) are common in quartz and carbonate fracture fillings within the Upper Carboniferous strata. Gaseous inclusions in fracture filling minerals hosted by Ca<sub>2</sub> carbonate are highly variable in composition; besides pure or nearly pure CO<sub>2</sub> inclusions that were trapped under high P-T conditions (Fig. 1), complex mixtures of CO<sub>2</sub>, CH<sub>4</sub>, H<sub>2</sub>S and ± N<sub>2</sub> are very frequent in many studied samples. These gas mixtures were trapped in inclusions at lower P conditions compared to CO<sub>2</sub>-rich inclusions (Fig. 1). Secondary trails of CH<sub>4</sub>-rich inclusions are indicative for a late migration of methane that locally significantly increased the quality of reservoir gas from formerly CO<sub>2</sub>-rich to CH<sub>4</sub>-dominated.

Fluid inclusion studies and REE distribution in fluorite have shown that CO<sub>2</sub> ascended along with hydrothermal fluids through faults into the reservoirs at temperatures between 200 °C and up to 315 °C and at near-lithostatic pressures, presumably liberated in phases of co-seismic ruptures and fault failure by shear in the context of tectonic inversion during the Late Cretaceous.

Integration of these data with core re-orientation techniques shows that most mineralized vein fillings that host CO<sub>2</sub>-rich fluid inclusions have a dominant NE-SW strike direction. This is parallel to the maximum (horizontal) stress orientation during the inversion phase, which allowed rapid and focused fluid flow along opening mode I direction. Those structural data has then been up-scaled from core to seismic interpretation, which showed that only very few NE striking far-reaching faults are actually connecting the ultra-deep Devonian through the Carboniferous with the Ca<sub>2</sub> reservoir. The migration model is that large volumes of CO<sub>2</sub>, together with hydrothermal fluids were ascending along the NE-striking faults until these fluids have been laterally injecting into the first available

permeable rock unit, which is a seismically definable downthrown (hanging wall) fault block of the Ca2 reservoir – similar to the concept of Mississippi-Valley-Type deposits. All existing high CO<sub>2</sub> content wells are located within such downthrown blocks, which are bounded by at least one of the NE-striking fault conduits and top-sealed by overlying Zechstein evaporites.

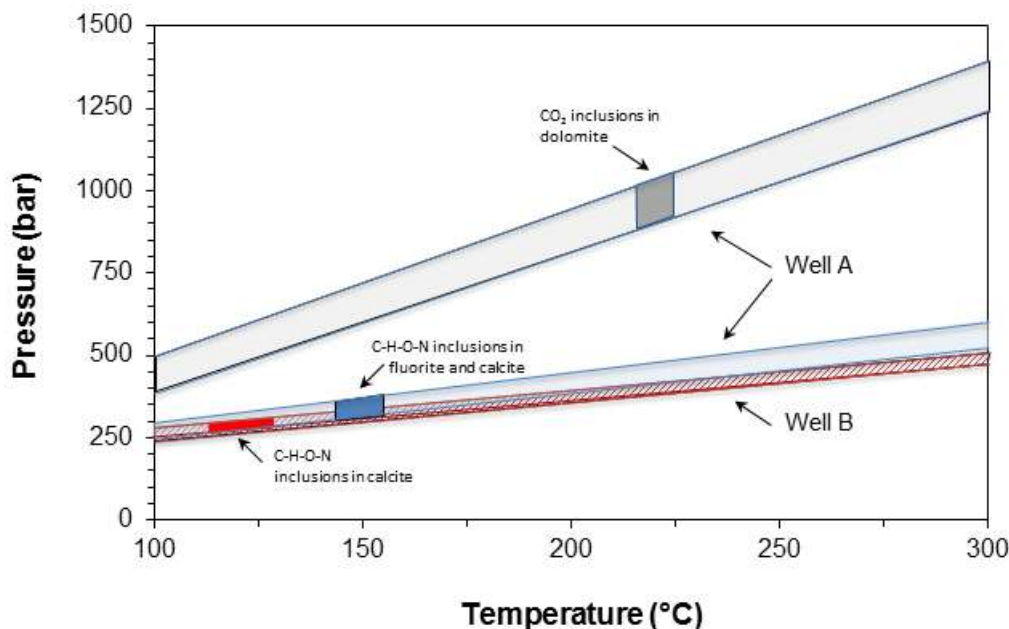


**Figure 1.** P-T diagram showing isochores of gaseous inclusions hosted in fracture-fill carbonate and fluorite in Zechstein Ca<sub>2</sub> carbonate from 2 wells located close to each other in the Uchte area. The colored fields show the P-T conditions of entrapment of cogenetic aqueous 2-phase and gaseous fluid inclusions derived from homogenization temperatures or crossing isochores of aqueous and gaseous inclusions.

The results of studies of carbon isotopic compositions of reservoir and fluid inclusion gases as well as  $\delta^{13}\text{C}$  values of fracture-fill carbonates suggest an inorganic origin of CO<sub>2</sub> in Zechstein Ca<sub>2</sub> reservoirs in the LSB. Proportions of TSR-derived CO<sub>2</sub> cannot be excluded but do not account for high CO<sub>2</sub> content in the reservoir gas since CO<sub>2</sub>-rich gaseous inclusions are also present in fracture filling minerals hosted by Palaeozoic rocks. A magmatic origin of fluids and/or CO<sub>2</sub> is unlikely in the light of the results of  $\delta\text{D}$  and  $\delta^{18}\text{O}$  isotopic composition of fluid inclusion waters, noble gases ratios and  $\delta^{13}\text{C}$  isotopic compositions of fluid inclusion gases. We conclude that decarbonation of deeply buried massive Devonian limestone is the most likely source for high CO<sub>2</sub> content in some Ca<sub>2</sub> reservoirs in the LSB.

#### REFERENCES

- Brown A.A. (1999) Distinguishing mantle CO<sub>2</sub> from decarbonation CO<sub>2</sub> in high CO<sub>2</sub> gases. AAPG Hedberg Research Conference "Natural gas formation and occurrence", Durango, Colorado, p. Abstract.
- Bruns B. et al. (2013) Petroleum system evolution in the inverted Lower Saxony Basin, northwest Germany: A 3D basin modeling study. *Geofluids* 13, 246-271.
- Fischer M. et al. (2006) Origins of CO<sub>2</sub> in Permian carbonate reservoir rocks (Zechstein, Ca<sub>2</sub>) of the NW-German Basin (Lower Saxony). *Chem. Geol.* 227, 184-213.
- Petmecky S. et al. (1999) High thermal maturity in the Lower Saxony Basin: inversion or deep burial? *Tectonophysics* 304, 317-344.
- Stadler G., Teichmüller M. (1971) Zusammenfassender Überblick über die Entwicklung des Bramscher Massivs und des Niedersächsischen Tektogens. *Fortschr. Geol. Rheinland und Westfalen* 18, 547-564.

## **Keynote – Stable isotope disequilibrium in zoned emerald precipitated from a two-phase fluid at chemical equilibrium?**

**Daniel D. MARSHALL<sup>1</sup>**, Gaston GIULIANI<sup>2</sup>, Lara L. LOUGHREY<sup>3</sup>

<sup>1</sup>*Earth Sciences, Simon Fraser University, Burnaby, Canada*

<sup>2</sup>*Centre national de la recherche scientifique, Nancy, France*

<sup>3</sup>*Teck Resources Limited, Vancouver, Canada*

*E-mail: marshall@sfu.ca*

This study concentrates on zoned emerald samples from two emerald occurrences: the Emmaville-Torrington deposit in Australia and the Byrud emerald deposit near Eidsvoll in Norway. Both deposits (Loughrey et al., 2012; 2013) are the more common igneous-related emerald deposit (Groat et al., 2014). The emeralds are zoned (Fig. 1) and display alternating bands of emerald green and clear growth zones within individual crystals at the millimeter scale. The zoning is seen optically but can also be observed via other imaging techniques such as backscattered electron, cathodoluminescence (CL), and chemically via electron microprobe or LA-ICP-MS analyses. Additionally, there is a correlation between the prevalence of a population of primary vapor-rich fluid inclusions within the optically clear (CL-dark) growth zones and a second population of primary highly-saline three-phase (liquid+vapor+halite) fluid inclusions in the colored (CL-bright) growth zones.

The two fluid inclusion populations appear to represent conjugate sets of a boiling system with the three-phase highly saline fluid inclusions having relatively high-salinities at NaCl saturation or greater. This population undergoes total homogenization into the liquid and probably represents fluids trapped in the liquid system of a two-phase (boiling) system. The vapor-rich population of fluid inclusions comprise a dilute aqueous fluid with average salinities of a few mass percent NaCl equivalent. These inclusions homogenize into the vapor phase at higher temperatures. Both fluid inclusion populations exist as secondary and pseudosecondary inclusions with the highly-saline population being more abundant.

The correlation of color versus clear growth zones corresponding to highly-salinity liquid-dominant and vapor-dominant low-salinity primary fluid inclusions, respectively, indicates that the color banding within the Emmaville-Torrington and Byrud emerald is related to emerald precipitation in the liquid or vapor portion of a boiling fluid system.

Chemical traverses parallel to growth zones via LA-ICP-MS and electron microprobe indicates similar compositions along growth zones. Traverses perpendicular to growth zones yields consistent correlation between CL light production with respect to Cr and V concentrations. Stable isotope traverses perpendicular to growth zones do not show consistent  $\delta^{18}\text{O}$  with respect to chemistry or Cl emission. This would indicate that isotopic equilibrium occurs at a slower rate than chemical equilibrium in the examined samples.

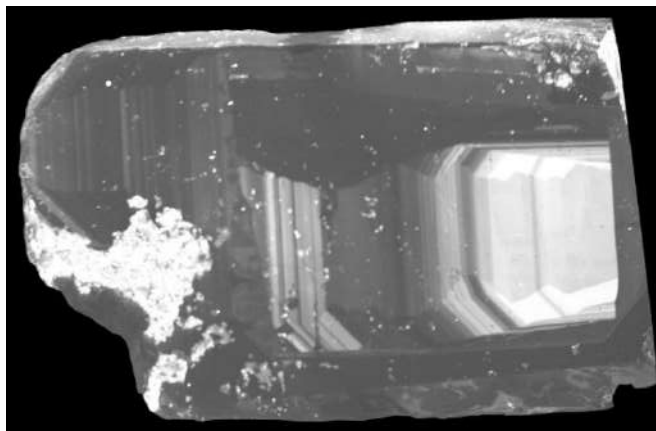


**Figure 1.** Cathodoluminescence (CL) image of a zoned emerald crystal from the Byrud deposit, Norway.

### REFERENCES

- Groat, L. et al. (2008) Emerald deposits and occurrences: A review. 2008, *Ore Geol. Revs.* 34, 87-112.
- Loughrey, L. et al. (2012) Pressure-temperature-fluid constraints for the Emmaville-Torrington emerald deposit, New South Wales, Australia: fluid inclusion and stable isotope studies, *Central Eur. J. Earth Sci.*, 4, 287-299.
- Loughrey, L. et al. (2013) Boiling as a mechanism for colour zonations observed at the Byrud emerald deposit, Eidsvoll, Norway: fluid inclusion and stable isotope and Ar-Ar studies, *Geofluids*, 13, 542-558.



## Invited – Metal and volatile budgets of rhyolite magmas coincident with Nevada’s world-class Carlin-type gold deposits

Celestine N. MERCER<sup>1</sup>, Kathryn E. WATTS<sup>2</sup>, Albert H. HOFSTRA<sup>1</sup>, Zoltán ZAJACZ<sup>3</sup>, Matthew A. COBLE<sup>4</sup>

<sup>1</sup>U.S. Geological Survey, Denver, Colorado, U.S.A.

<sup>2</sup>U.S. Geological Survey, Menlo Park, California, U.S.A.

<sup>3</sup>Department of Earth Sciences, University of Toronto, Toronto, Ontario, Canada

<sup>4</sup>Stanford University, Stanford, California, U.S.A.

E-mail: cmercer@usgs.gov

Nevada’s Carlin-type gold deposits (USA) collectively represent the second largest Au endowment on Earth. With historic production and reserves of >6000 tons, mining of these deposits dominates Au production in the United States and accounts for ~9% of world production [1]. These deposits formed over a relatively short interval of time (42-34 Ma) coinciding with profuse magmatism that swept southwestward across Nevada [2]. Magmatism was initiated by a shift from compressional, flat-slab subduction to extensional tectonism due to foundering of the Farallon slab and upwelling of asthenospheric mantle into subduction-metasomatized subcontinental lithosphere [2]. Carlin-type Au deposits are structurally and stratigraphically controlled sediment-hosted ore bodies characterized by enrichments in Au, As, Sb, Hg, Tl, (Te, and W), high ratios of Au/Cu (~0.1-10) and Au/Ag (~10), and a paucity of Ag and base metals (e.g., Cu, Pb, Zn, Ni; e.g., [3]).

Despite over 50 years of mining and research, finding a smoking gun to unify the current models proposed for these deposits remains elusive because the source of heat, fluids, and metals is still debated. The magmatic-hydrothermal model suggests that nearby intrusions provided heat and exsolved S- and Au-bearing fluids from parental magmas with high initial Au/Cu ratios [e.g., 4, 5, 6]. The metamorphic model favors lower crustal metamorphic fluids that ascended along basement-penetrating extensional faults and scavenged Au from pre-enriched metasediments [e.g., 1]. The sedimentary-source model suggests that meteoric fluids driven by extension-generated heat and permeability leached Au from pre-enriched sediments [e.g., 7, 8, 9]. Economically important Au deposits with similarities to Carlin-type deposits are located in the West Qinling belt and Dian-Qian-Gui area of southern China [e.g., 10]. Given that the various conceptual models will lead exploration geologists to different geologic environments in search of new Au discoveries, the debate about the origin of Carlin-type Au deposits is beyond merely academic.

We present high-sensitivity, high-spatial resolution microanalyses of silicate and sulfide melt inclusions, providing the first direct evidence of the pre-eruptive metal (Au, As, Sb, Tl, Te, W, Cu, Mo, Ag, Pb, An, Sn, Co, Ni) and volatile (H<sub>2</sub>O, CO<sub>2</sub>, S, F, Cl) budgets of magmas coincident in time and space with Carlin-type Au deposits. Data were acquired using SHRIMP-RG ion microprobe and laser ablation mass spectrometry, FTIR spectroscopy, electron beam microscopy. Melt inclusions provide the best measure of Au and Cu budgets (among other metals) in parental magmas compared to whole rock analysis because metals like Au and Cu partition into the magmatic fluid phase upon rock solidification [e.g., 11, 12]. The melt inclusion data we present provide “snapshots” of pre-eruptive magma compositions at shallow crustal levels (≤~5 km depth). Using these data, we test the hypothesis that Eocene felsic magmas in the shallow crust had high Au/Cu ratios and could have contributed S- or metals critical to the formation of Carlin-type Au deposits.

Our sample suite includes pre-, syn-, and post-mineralization porphyritic intrusions and tuffs (42-34 Ma) in close proximity (~0-5 km) to known Carlin-type Au

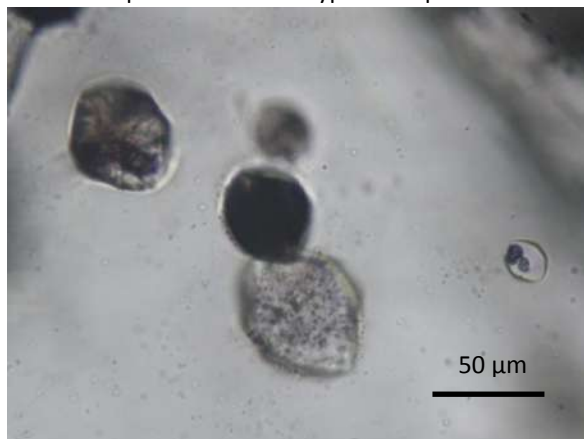


**Figure 1.** Photomicrograph of quartz-hosted, variably crystalline silicate melt inclusions from the Beast dike (Carlin Trend).

districts in the Carlin (Beast, Genesis), Battle Mountain-Eureka (Cortez Hills Complex, Archimedes/Ruby Hill), and Alligator Ridge (Galaxy/Horseshoe/Saga) trends, and the newly recognized Long Canyon trend.

Silicate melt inclusions are rhyolite to high-silica rhyolite (~8-17 wt% Al<sub>2</sub>O<sub>3</sub>, ~4-11 wt% Na<sub>2</sub>O+K<sub>2</sub>O, ASI~0.9-1.4) and overlap with the most evolved Eocene igneous whole rock samples from the region. They span a range in (1) tectonic affinity (volcanic-arc to within-plate), (2) temperature (~670-770°C), (3) volatile contents (up to 4.3 wt% H<sub>2</sub>O, 950 ppm CO<sub>2</sub>, 490 ppm Li, 140 ppm S, 2.3 wt% F, and 1920 ppm Cl), (4) oxidation state (*f*O<sub>2</sub> dominantly ~NNO-2.0 to NNO+1.5, with the two most arc-like samples ranging from NNO+2 to NNO+4), (5) eruptive volume (dikes to ignimbrites), (6) degree of melt fractionation (Rb/Sr~0.6-70, Eu/Eu\*~0.02-1.2, Nb/Nb<sup>0</sup>~1.1-6.0), (7) degassing style (ascent-driven vs. crystallization-driven), and (8) degree of marine sediment contamination (subduction and/or crustal; (La/Sm)<sub>CN</sub>~1-11). The broad diversity amongst the rhyolites in our suite reflects their evolution within the dynamic tectonic setting of north central Nevada during the Eocene epoch. Carlin-type metal concentrations are low to moderate in silicate melts (≤~3-280 ppb Au, ~0.5-22 ppm As, ~0.2-2.2 ppm Sb, ≤~0.2-6.3 ppm Tl, ≤~16-44 ppb Te, ~0.5-7.3 ppm W), while base metal and other potential ore-forming metal concentrations range from low to high (≤~0.05-1.0 ppm Ag, ≤~0.1-9 ppm Mo, ≤~0.1-40 ppm Cu, ~1-80 ppm Pb, ~10-150 ppm Zn, ~4-17 ppm Ni, ~0.2-2.3 ppm Co, ~0.6-25 ppm Sn). Pyrrhotite melt inclusions in one sample contain homogeneous and low Au concentrations (0.9 ppm) and more heterogeneous concentrations of other metals (100-30,000 ppm Cu, 5-8,000 ppm As, 200-4,000 ppm Ni, 0-100 ppm Sb, 0-20 ppm Te). Electron microprobe analyses of pyrrhotite indicate molar Fe/S ratios of 0.84-0.89, corresponding to NFeS=0.91-0.95, and log *f*S<sub>2</sub>= 0 to -3 at magmatic temperatures of 800-850 °C.

Melt inclusions have notably lower Au/Cu (~≤0.0005-0.1), Au/Ag (~0.05-5), and Au/Tl (~0.001-0.3) ratios than do high-grade Carlin-type ore samples, however, to effectively evaluate the true mineralization potential of these magmas, we must consider (1) the effect of magmatic sulfide saturation on the metal budget of silicate melts and (2) the efficiency of metal removal from a silicate melt during fluid exsolution. We will present results from modeling of hypothetical exsolved fluid compositions [e.g., 13], taking as many of the relevant magmatic physiochemical variables into account as possible (e.g., alumina saturation index, alkalinity, salinity, S contents, Cl/H<sub>2</sub>O, *f*O<sub>2</sub>, temperature, pressure, and the presence or absence of suspended magmatic sulfides).

## REFERENCES

- [1] Cline J.S. et al. (2005) Carlin-type gold deposits in Nevada: critical geologic characteristics and viable models. *Econ. Geol.*, 451–484.
- [2] Best M.G. et al. (2016) Slab-rollback ignimbrite flareups in the southern Great Basin and other Cenozoic American arcs: A distinct style of arc volcanism. *Geosphere* 12, 1097–1135.
- [3] Hofstra A.H., Cline J.S. (2000) Characteristics and models for Carlin-type Au deposits, *Rev. Econ. Geol.*, 163-220.
- [4] Kesler S.E. et al. (2005) Evidence for a magmatic origin for Carlin-type gold deposits: isotopic composition of sulfur in the Betze-Post-Screamer Deposit, Nevada, USA. *Miner Deposita* 40, 127–136.
- [5] Muntean J.L. et al. (2011) Magmatic–hydrothermal origin of Nevada's Carlin-type gold deposits. *Nature* 4, 1–6.
- [6] Large S.J.E. et al. (2016) Trace elements in fluid inclusions of sediment-hosted gold deposits indicate a magmatic-hydrothermal origin of the Carlin ore trend. *Geology*, 1–6.
- [7] Ilchik R.P., Barton M.D. (1997) An amagmatic origin of Carlin-type gold deposits. *Econ. Geol.*, 269-288.
- [8] Emsbo P. et al. (2006) The giant Carlin gold province: a protracted interplay of orogenic, basal, and hydrothermal processes above a lithospheric boundary. *Miner. Deposita* 41, 517–525.
- [9] Large R.R. et al. (2011) A carbonaceous sedimentary source-rock model for Carlin-type and orogenic gold deposits. *Economic Geology*, 331-358.
- [10] Hofstra A.H., Christensen O.D. (2002) Comparison of Carlin-type Au deposits in the United States, China, and Indonesia: implications for genetic models and exploration, USGS Open File Report, 1-94.
- [11] Heinrich C.A. (2006) How Fast Does Gold Trickle Out of Volcanoes? *Science* 314, 263–264.
- [12] Zajacz Z. et al. (2017) The partitioning of Cu, Au and Mo between liquid and vapor at magmatic temperatures and its implications for the genesis of magmatic-hydrothermal ore deposits. *Geochim. Cosmo. Acta* 207, 81–101.
- [13] Zajacz Z. et al. (2010) Alkali metals control the release of gold from volatile-rich magmas. *EPSL* 297, 50–56.

## The volatile budget of Haleakala (Maui): new insights from melt inclusions

Lowell R. MOORE<sup>1</sup>, Esteban GAZEL<sup>2</sup>, Robert J. BODNAR<sup>1</sup>

<sup>1</sup>Fluids Research Laboratory, Department of Geosciences, Virginia Tech, Blacksburg, Virginia, U.S.A.

<sup>2</sup>Department of Earth and Atmospheric Sciences, Cornell University, Ithaca, New York, U.S.A.

E-mail: moorelr@vt.edu

Volcanic activity in the Hawaiian Islands evolves through a sequence of volcanic stages that include 1) a low-volume, alkaline pre-shield stage, 2) a high-volume, tholeiitic shield stage, 3) a low-volume, alkaline post-shield or “capping” stage, and 4) a very low volume, alkaline rejuvenated or “post-erosional” stage (Clague & Sherrod, 2014). While the shield stage has been thoroughly studied, the transition from post-shield to rejuvenated stage is poorly understood – especially regarding the relationship between mantle source composition and magma volatile budgets. Haleakala (Maui) represents the end of the post-shield stage, and it is an ideal location to study this enigmatic transition in volcanic behavior. To determine the pre-eruptive volatile content of the melt and estimate the volatile content of the melting source material, we sampled glassy melt inclusions from Haleakala.

Fresh tephra samples were collected from basaltic cinder cones at the summit of Haleakala, and lava samples were collected from the periphery of the island. Bulk lava and tephra compositions were determined using X-ray fluorescence (XRF) and laser ablation inductively coupled plasma mass spectrometry (LA-ICP-MS). Olivine crystals containing glassy melt inclusions (MI) were removed from the tephra samples and polished to expose the glass without breaching shrinkage bubbles. The amount of CO<sub>2</sub> contained in vapor bubbles was estimated using Raman spectroscopy. MI glasses were analyzed using secondary ion mass spectrometry (SIMS) and electron probe microanalysis (EPMA). Petrolog3 and MELTS software were used to correct MI compositions for Fe-loss and post-entrapment crystallization (PEC) and to determine the conditions and extent of fractional crystallization of melts trapped by MI. The volatile solubility model of Iacono-Marziano et al. (2015) was used to calculate volatile-melt saturation pressures.

MI contain approximately 0.5 to 1 wt% of both CO<sub>2</sub> and H<sub>2</sub>O, which corresponds to trapping pressures of up to 8-9 kbar. This amount is consistent with the amount predicted for ~10 kbar saturation pressures estimated for pyroxene phenocrysts erupted from Kula volcanics (Hammer et al., 2016) given ~1.5 kbar of uncertainty associated with both pressure estimates and suggests that the MI trapped melts that were volatile-undersaturated. MI and whole rock major element compositions are mutually consistent with fractional crystallization trends originating from the composition of the most MgO-rich inclusion and 50-100 bar/°C decompression from 10 kbar to 500 bar, followed by isobaric crystallization (Fig. 2). Observed olivine host compositions (Fo 86-73) compared with MELTS models (Fig. 2a) indicate that melts experienced ~20-60% crystallization before inclusions were trapped (Fig 2a inset).

To determine the extent of volatile loss to degassing before melt inclusions were trapped, relative concentrations of variably soluble volatile elements in MI were compared (Figure 2b). Our results indicate negligible loss of Cl and F, moderate loss of S and H<sub>2</sub>O, and major loss of CO<sub>2</sub> to degassing. After correcting for PEC, CO<sub>2</sub> exsolution into fluid bubbles, and fractional crystallization, primary melts supplying Haleakala contain approximately 0.15 wt% S, 0.7 wt% H<sub>2</sub>O, and 0.7 wt% CO<sub>2</sub>. However, because it is not clear whether any of the melt inclusions analyzed in this study were trapped before CO<sub>2</sub> began to degas, the CO<sub>2</sub> concentration of the primary melt that we report represents a minimum estimate.

We used a batch melting approach to estimate the volatile content of the melting source material associated with Haleakala. Compared to the shield stage, post-shield-stage magmas are generated from a lower degree of partial melting as a result of their relative distance from the center of the hot spot. Estimated melt fractions for post-shield volcanism vary from ~1-3 % depending on the composition of the source material, which is consistent with whole rock trace element concentrations obtained in this study. Using the maximum melt fraction (3%) and a batch melting calculation, melts from Haleakala could be derived from a source material containing 45 ppm S, 210 ppm H<sub>2</sub>O, and 210 ppm CO<sub>2</sub>. Source volatile concentrations could be lower if the melt fraction is lower, and the CO<sub>2</sub> concentration of the source may be higher if some unknown amount of CO<sub>2</sub> was lost to degassing before the MI were trapped.

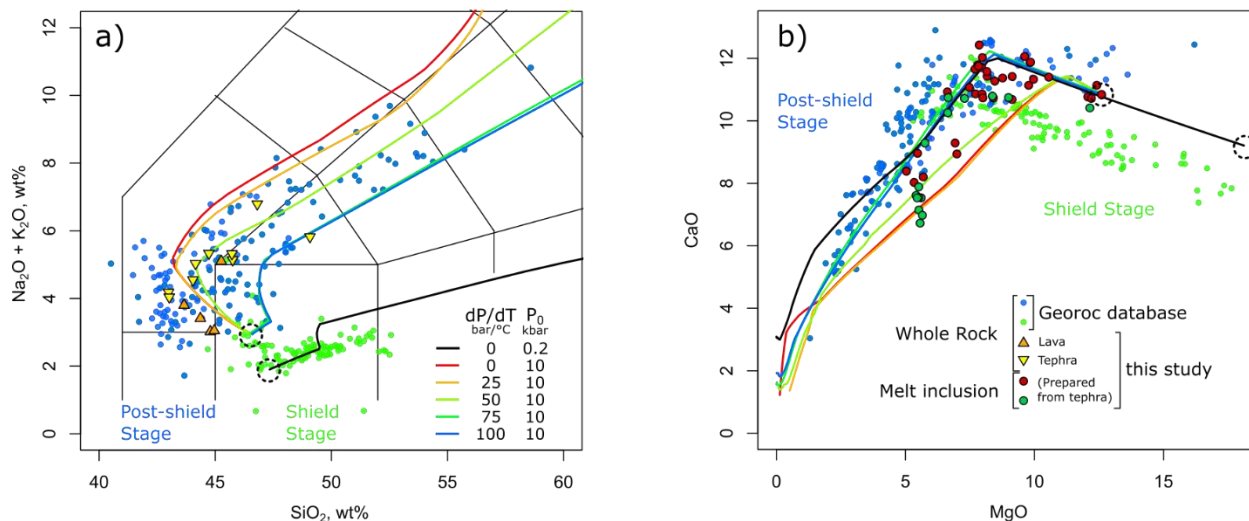


**Figure 1.** Whole rock (a) and melt inclusion (b) compositions compared with MELTS models. Dashed circles indicate parental melt compositions from the most MgO-rich inclusion analyzed and a Kilauea primary melt composition calculated by Sobolev et al. (2005). Haleakala shield and post-shield whole rock compositions from Geocor database (<http://geocor.mpch-mainz.gwdg.de/geocor/>) are shown for comparison.

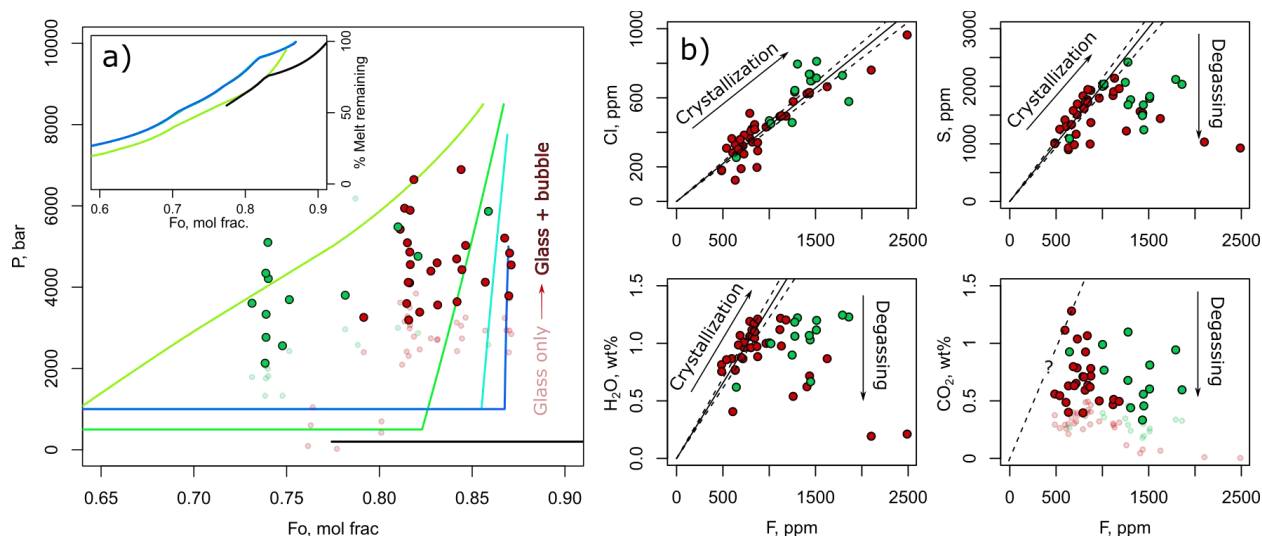


**Figure 2.** (a) Volatile-melt saturation pressures and MI host compositions compared with MELTS model results. Inset shows remaining melt fraction during fractional crystallization. (b) MI volatile concentrations with linear regression of presumably undegassed volatile concentrations indicating fractional crystallization. Light-colored symbols indicate MI glass compositions not corrected to include CO<sub>2</sub> exsolved into bubbles.

REFERENCES

Clague, D.A., Sherrod, D.R. (2014) Growth and Degradation of Hawaiian Volcanoes, U.S. Geological Survey Professional Paper 1801, 97-146.  
 Sobolev, A.V., Hofmann, A.W., Sobolev, S.V., Nikogosian, I.K. (2005) An olivine-free mantle source of Hawaiian shield basalts, *Nature*, 434, 590-597.  
 Iacono-Marziano, G., Morizet, Y., Le Trong, E., Gaillard, F. (2012) New experimental data and semi-empirical parameterization of H<sub>2</sub>O–CO<sub>2</sub> solubility in mafic melts, *Geochimica et Cosmochimica Acta*, 97, 1-23.  
 Hammer, J., Jacob, S., Welsch, B., Hellebrand, E., Sinton, J. (2016) Clinopyroxene in postshield Haleakala ankaramite: 1. Efficacy of thermobarometry, *Contrib. Min. Pet.*, 171:7.

## **Invited – The melt inclusion record of the countdown to eruptions**

**Megan E. NEWCOMBE<sup>1</sup>, Alexander S. LLOYD<sup>1</sup>, David FERGUSON<sup>2</sup>, Anna BARTH<sup>1</sup>, Erik HAURI<sup>3</sup>, Terry A. PLANK<sup>1</sup>**

<sup>1</sup>Lamont-Doherty Earth Observatory of Columbia University, Palisades, New York, U.S.A.

<sup>2</sup>University of Leeds, Leeds, U.K.

<sup>3</sup>Department of Terrestrial Magnetism, Carnegie Institution of Washington, DC, U.S.A.

E-mail: [newcombe@ldeo.columbia.edu](mailto:newcombe@ldeo.columbia.edu)

Olivine-hosted melt inclusions are valuable petrologic tools. They are traditionally exploited for their ability to shield small quantities of magma from the myriad of crustal processes (e.g. degassing, crystallization, magma mixing, assimilation) that act to obscure the compositions of primary melts feeding a given magmatic system. It is widely acknowledged that the compositions of olivine-hosted melt inclusions can be altered from the original trapped melt composition via post-entrapment processes such as diffusive re-equilibration, post-entrapment crystallization and vapor bubble formation. Recent studies have found that some of these post-entrapment processes operate on short timescales (seconds to hours) and reflect the rapid and extreme physical and chemical changes that the melt inclusions experience during the final stages of magma ascent, eruption, and deposition. Chemical zonation inside olivine-hosted melt inclusions and across their olivine hosts leaves a record of syneruptive conditions in the volcanic conduit. Characterization of this chemical zonation can be used to constrain the nature and timing of conduit processes.

We have constrained syneruptive pressure-temperature-time (P-T-t) paths of olivine-hosted melt inclusions and their host magmas using a combination of short-timescale cooling and decompression chronometers. Recent work has shown that the thermal histories of crystals in the last few seconds to hours of eruption can be constrained using concentration gradients of MgO inside olivine-hosted melt inclusions, produced in response to syneruptive cooling and crystallization of olivine on the inclusion walls (Newcombe et al. 2014). We have applied this technique to the study of melt inclusions erupted by arc and ocean island volcanoes, including the subplinian 1974 eruption of Fuego volcano; the 1977 fire-fountain eruption of Seguam volcano; and three eruptions of Kilauea volcano (episode 1 of the 1959 Kilauea Iki fire-fountain eruption, the Keanakākoʻi basal reticulate of the 1500 CE vigorous fire-fountain eruption, and the Keanakākoʻi layer 6 deposit of the 1650 CE subplinian eruption).

Of the eruptions studied so far, melt inclusions from the 1959 Kilauea Iki fire fountain eruption record the highest syneruptive cooling rates ( $\sim 10^3$ – $10^4$  °C/hr) and the shortest cooling durations ( $\sim 10^0$ – $10^1$  s). The largest melt inclusions (radii up to 170  $\mu\text{m}$ ) from the Kilauea and Seguam fire fountain eruptions exhibit long plateaus of approximately constant MgO across their centers, suggestive of ascent through the conduit at an approximately constant temperature (or a period of shallow magma stalling) prior to fragmentation. Melt inclusions from Fuego record the lowest cooling rates ( $\sim 10^2$ – $10^3$  °C/hr) and longest cooling durations ( $\sim 10^2$ – $10^3$  s) of the studied eruptions.

The average cooling rates of melt inclusions from the studied eruptions are negatively correlated with magma decompression rates (as determined from volatile gradients in melt embayments). Division of our calculated cooling rates by decompression rates for each eruption allows us to estimate the amount of cooling as a function of magma decompression. Our estimate of  $\sim 30$  °C/kbar for Fuego is consistent with adiabatic ascent of a magma containing  $\sim 60$  vol. % vapor. The high cooling rates inferred for Seguam and Kilauea Iki are consistent with air quenching over 10s of seconds upon fragmentation and eruption. Preliminary results of this approach are in agreement with thermodynamic models that show that the dominant driver of cooling in the conduit is adiabatic expansion of a vapor phase. A corollary of these models is that, in order to drive syneruptive cooling, the magma must ascend rapidly enough to prevent significant melt-vapor separation.

### REFERENCE

Newcombe ME, Fabbriozio A, Zhang Y, Ma C, Le Voyer M, Guan Y, Eiler JM, Saal AE, Stolper EM (2014) Chemical zonation in olivine-hosted melt inclusions. *Contributions to Mineralogy and Petrology* 168 (1):1-26. doi:10.1007/s00410-014-1030-6



## Characteristics and significance of fluid inclusions in the Longmaxi Shale in the Jiaoshiba area, Eastern Sichuan Basin, China

Guangxi OU<sup>1,2</sup>, Min ZHANG<sup>1,2</sup>, Tieguan WANG<sup>2</sup>, Di WU<sup>1</sup>, Qiong LI<sup>1</sup>, Jian MA<sup>2</sup>

<sup>1</sup> CNNC Beijing Research Institute of Uranium Geology, Beijing, China

<sup>2</sup> College of Geosciences, China University of Petroleum, Beijing, China

E-mail: 1508716884@qq.com

The Jiaoshiba shale gas field is located in the Fuling National Shale Gas Demonstration Zone. It is part of the Jiaoshiba structure in the southeast of eastern Sichuan fold belt and to the west of the Qiyueshan fault belt, which is a special positive structural unit in the Wanxian Synclinorium. Different from the NE-trending or near NS-trending narrow and high-dipping anticlines in two sides, the Jiaoshiba structure controlled by NE-trending and SW-trending faults is a broad box-shaped faulted anticline with NE-trending axial, which is divided by fault uplift, fault depression and Qiyueshan fault. The main body of Jiaoshiba structure was weakly deformed with uniform upper and lower structure that is characterized by box-like faulted anticline with gentle and wide top, small dip angle, and dipping wings.

Most Palaeozoic can be found in the Jiaoshiba structure without Devonian and only Huanglong Formation in the carboniferous, while the Middle-Triassic Jialingjiang Formation is exposed. The black and gray black marine shale primarily occurs at the lower section of Lower Silurian Longmaxi Formation with stable thickness of 89-102m and type I and II1 kerogen. Vitrinite reflectance ( $R_o$ ) indicates high-over high mature shale. Pressure coefficients from over 100 wells range from 1.0 to 1.55, while values of main structure unit is in a range of 1.30 to 1.55, indicating the occurrence of overpressure in shale reservoir. Longmaxi shale in the JYB-5 and JYA-4 wells is interbedded with argillaceous siltstone of 2~5cm, where high-angle and wide (3~5mm) fracture commonly occurs with calcite and quartz fill.

Microscopic observation of fluid inclusions shows that considerable methane-rich fluid inclusions occur in the quartz particles and quartz-calcite veins in the thin siltstone interlayer, coexisting with brine inclusions with hydrocarbon. The hydrocarbon inclusions are generally gray and dark gray, while brine inclusions with hydrocarbon are colorless or gray. Methane-rich fluid inclusions are commonly distributed in zonal or linear pattern in the microfracture across quartz grains and enlarged edges, while they are mostly distributed in group and belt in the quartz-calcite veins.

Microthermometry analyses indicate that brine inclusions with hydrocarbon from Longmaxi shale in the Jiaoshiba area have homogenization temperatures ( $T_h$ ) ranging from 100 to 220°C. Specifically,  $T_h$  of inclusions in the microfractures varies from 100 to 170 °C with peak value of 130-140 °C and 160-170 °C, indicating two episodes of gas accumulation, while the  $T_h$  of inclusions in the quartz-calcite veins is 130-220 °C with peak value of 180-200 °C, representing temperature of shale gas being destroyed during tectonic activities.

A large number of experiments from home and abroad proved that Laser Raman shift (wave number) of methane inclusions positively correlated with temperature under certain pressure, whereas, it negatively correlated with pressure under certain temperature. Fluid inclusions identified from argillaceous siltstone in the JYA-4 well and JYB-5 well are commonly methane-saturated inclusions. Fluid inclusion petrography and Laser Raman microprobe analyses further evidence that fluid inclusions are dominated by methane-saturated inclusions, which provides qualified samples to restore pressure.

This study measured the Laser Raman shift (wave number) of methane-saturated inclusions under different trapping temperature based on the variation of the Laser Raman shift with temperature and pressure, which can be used to calculate methane density. Consequently, the internal pressure of these inclusions was determined using the equations from Duan et al (1992) and homogenization pressures with value ranging from 54 to 75 MPa.

Rb-Sr isotopic dating and K-Ar isotopic dating were used to identify enrichment period of Longmaxi shale gas. Rb-Sr isotopic dating indicates the hydrocarbon generation and expulsion in the siltstone occurred during Early-Middle Jurassic (187.8±8.9Ma), while it was 189-191 Ma determined by K-Ar isotopic dating, which agree well with

each other. We therefore conclude that gas accumulating in the Longmaxi thin siltstone interlayers was mainly during Early- Middle Jurassic.

Parameters of fluid inclusions, including homogenization temperature, component, pressure, etc., are important to investigate hydrocarbon enrichment. This study employed thermal-burial-history to analyze the geological significance of these data and dating data. The temperature plotted in the thermal-burial-history indicates the gas filling in the Longmaxi reservoir mainly occurred during Early-Middle Jurassic, which is consistent with the conclusion of isotopic dating. Corresponding pressure coefficient of Longmaxi shale determined by the internal pressure of fluid inclusions (54-75MPa) and burial depth (4250-4800m) was 1.27-1.56, suggesting overpressured shale during hydrocarbon generation and expulsion. Drilling data confirmed the occurrence of overpressure in the Longmaxi shale with pressure coefficient of 1.30-1.558[11]. Previous study suggested that overpressure was a good indicator of preservation condition. Therefore, the high pressure coefficient during gas enrichment period (Early-Middle Jurassic) indicated good preservation condition for Longmaxi shale gas in the Jiaoshiba area. Meanwhile, overpressure fluid contributed to the pores preservation in shale reservoir. Therefore, high-quality source rocks, reservoirs, preservation condition and high gas saturation make the Longmaxi shale in the Jiaoshiba area potential gas reservoir.

Conclusions:

(1) Fluid inclusion petrography and microthermometry analyses suggest that the peak temperatures of coeval aqueous inclusions in the argillaceous siltstone are 130-140 °C, 160-170 °C, representing two episodes of gas accumulation. And the homogenization temperatures of brine inclusions with hydrocarbon in the quartz-calcite veins are corresponding temperature during the gas loss from initial gas reservoir.

(2) Hydrocarbon inclusions can be widely found in the Longmaxi shale, which were primarily methane-saturated inclusions. The fluid pressure determined by the methane-saturated inclusions with the Laser Raman microprobe analyses was about 54-75 MPa during the shale gas enrichment.

(3) Rb-Sr isotopic dating and K-Ar isotopic dating with fluid inclusions in the siltstone interlayer shows that peak period of gas filling in the Longmaxi shale was Early-Middle Jurassic, which matches well with the time derived from burial and thermal history.

(4) The pressure coefficients of Longmaxi shale in the Jiaoshiba area were 1.27-1.56, 1.63-2.18 and 1.30- 1.55, respectively, during the early stage (Early-Middle Jurassic), middle stage (Yanshan- himalayan period) and later stage (present), indicating the occurrence of overpressure and thereby high-quality source rock and favorable preservation conditions. Therefore, high-quality source reservoir cap assemblage and high gas saturation make the Longmaxi shale in the Jiaoshiba area potential gas reservoir.

## Keynote – Hydrocarbon inclusions: the story

Jacques PIRONON

CNRS-CREGU, GeoRessources Lab, Université de Lorraine, Nancy, France

E-mail: jacques.pironon@univ-lorraine.fr

Fluid inclusions, located inside diagenetic minerals, are the precious witnesses of paleo-fluids when they are unchanged in volume and composition with time. The hydrocarbon inclusions are proxies of temperature and pressure and they act as efficient tools for basin modelling, geodynamical reconstruction and then for oil & gas prospection. Hydrocarbon inclusions are tracked in very old sedimentary basins as the witnesses of the beginning of life. They are also frequently described in Mississippi Valley Type deposits, in metamorphic and in hydrothermal environments where they constitute indices of sediment contaminations. But hydrocarbon inclusions are also the witnesses of the modern history of mineralogy.

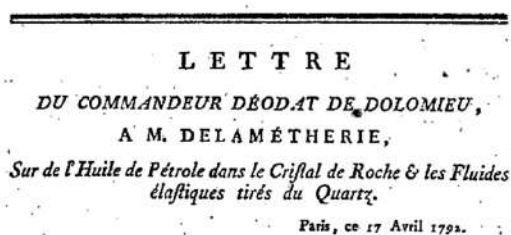


**Figure 1.** The first scientific publication about hydrocarbon inclusions by D. de Dolomieu in *Journal de Physique* (1792).

The hydrocarbon inclusions were at the heart of the first discoveries of fluid inclusions in minerals. It is not a surprise to find traces of hydrocarbon inclusions in the remarkable papers of the first mineralogists who were fascinated by impurities in gems. Sir David Brewster in Edinburgh (1826) described liquid inclusions in topaz crystals from Brazil, Scotland, and Australia, in quartz crystals from Quebec (Figure 2), and in amethysts from Russia. He described the volumetric changes of the fluid phases with temperature and discussed about the fluid chemistry using the measurement of the refractive indices. He described three main fluid phases in inclusions. He assigned the two first to gas and water and the third to a new phase he did not characterize. In 1850, J.D. Dana reinterpreted Brewster descriptions suggesting the presence of water, liquid CO<sub>2</sub> and possibly another kind of liquid he named "brewsterinite" or "cryptoline". Van Nordenskjöld (1886) suggested this other kind of liquid was hydrocarbon.

The first use of UV-fluorescence to detect the presence of hydrocarbon inclusions is assigned to C. L. Reese (1898) who observed inclusions in quartz. The fluorescence technique has been generalized and some authors used it to approximate the fluid density (Bodnar, 1990) or to detect palaeo Oil-Water contacts (Eadington et al., 1996). It was necessary to wait the middle of the twentieth century to re-discover the hydrocarbon inclusions with the development of new techniques. The works of W. Wahler (1955) were the archetype of the transition between the nineteenth and the twentieth century. He used the refractive index technique after calibration with artificial inclusions created by sealing silica microcapillaries. He decrepitated the inclusions by heating and measured the escaped fluid by fractional combustion and/or by condensation, by spectrographic photographs, and quantitatively by measurement of pressure differences. R. C. Murray in 1957 acquired the first complete analysis of an individual hydrocarbon inclusion by mass spectrometry on

Déodat Guy Sylvain Tancrède de GRATET de DOLOMIEU was probably the first how revealed the existence of hydrocarbon inclusions in minerals. He published in 1792 in the *Journal of Physics* in France one page of contribution (Figure 1) that was in fact the extract of a letter received from his friend, Felice Fontana, Director of the Cabinets of Physics and Natural History in Florence since 1766. F. Montana described two quartz crystals containing small cavities filled by a yellowish fluid. He opened some of them and smelt the typical odor of liquid bitumen which burned on contact with a flame. These crystals belonged to Dr. Giovanni Targioni Tozzetti, physician and naturalist, who was in charge in 1763 of the catalogue of the natural specimens housed in the Galleria Imperiale in Florence.

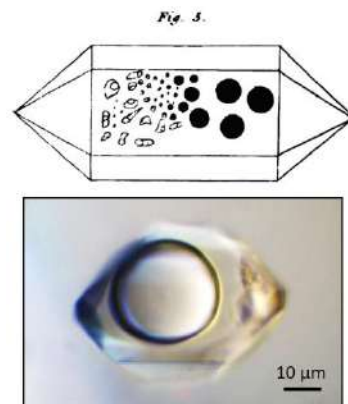


**Figure 2.** Quartz of Quebec (Canada). Top: decrepitation of inclusions producing dark droplets described by D. Brewster in 1826. Bottom: Photomicrograph of a fluid inclusion containing gas condensate analyzed by FT-IR (Pironon et al., 2001)

a 2 mm cavity in a quartz crystal from the Mississippian Rundle formation in Alberta (Canada). This remarkable analysis, not reproduced to date, showed a composition of gas condensate with an extremely high accuracy. Mass spectrometry was intensively used after for bulk analysis of hydrocarbon inclusions after crystal heating or crushing (several references in George et al., 2012). A widespread screening technique called the fluid inclusion stratigraphy was applied to cleaned core chips or cuttings that are crushed using pneumatic rams (Smith, 1994, Barclay et al., 2000). Dereppe et al. (1994) applied  $^1\text{H}$  NMR technique to around  $1\text{ cm}^3$  of isolated natural and synthetic crystals and demonstrated it was possible to differentiate and quantify  $\text{CH}_4$ , water and hydrocarbons. The development of computers was probably responsible for the development of techniques applied to individual inclusions. It was the case of FT-IR applied to hydrocarbon inclusions of more than  $10\text{ }\mu\text{m}$  in size (Pironon et al., 2001), of Confocal Scanning Laser Spectroscopy (Pironon et al., 1998) and X-Ray tomography (Richard et al., 2017) to reconstruct in 3D the volume of tiny inclusions. ToF-SIMS combining 3D and chemical analysis was applied by Siljeström et al. (2010) whereas Volk et al. (2010) and Demange et al. (2011) developed laser ablation coupled with GC-MS and ICP-MS respectively.

#### REFERENCES

- Barclay S.A., Worden R.H., Parnell J., Hall D.L., Sterner S.M. (2000) Assessment of fluid contacts and compartmentalization in sandstone reservoirs using fluid inclusions: an example from the Magnus oil field, North Sea. *American Association of Petroleum Geologists Bulletin*, 84, 489 - 504.
- Bodnar, R.J. (1990) Petroleum migration in the Miocene Monterey Formation, California, U.S.A. : Constraints from fluid-inclusion studies. *Mineralogical Magazine*, 54, 295-304.
- Brewster D. (1826) On the refractive power of the two new fluids in minerals, with additional observations on the nature and properties of these substances. *Royal Soc. Edinburgh Trans.*, vol. 10, 407-427.
- Dana J. D. (1850) *System of Mineralogy* 3rd edn, p. 559
- De Dolomieu D. (1792) Sur de l'huile de pétrole dans le cristal de roche et les fluides élastiques tirés du quartz. *Observations sur la Physique*, v. 42, 318-319
- Demange C., Banks D, Boiron MC, Dubessy J., Michels R. (2011) LA-ICP-MS analysis of trace metals in hydrocarbon fluid inclusions associated with ore deposits. *ECROFI-XXI Leoben, Austria*, 9–11 August, Abstracts, p. 60
- Dereppe J. M., Pironon J., Moreau C. (1994) Characterization of the composition of fluid inclusion in minerals by  $^1\text{H}$  NMR. *The American Mineralogist*, 79, 712-718.
- Eadington P., Cadman S., Fellows M. (1996) Late Tertiary fluid migration in the Timor Sea. A key control on thermal and diagenetic histories? *APEA Journal*, 36, 399-427.
- George S. C., Volk H. and Dutkiewicz A. (2012) Chapter 30. Mass Spectrometry Techniques for Analysis of Oil and Gas Trapped in Fluid Inclusions. *In Mass Spectrometry Handbook*, Mike S. Lee Editor. 647-673.
- Murray R. C. (1957) Hydrocarbon fluid inclusions in quartz [Alberta]. *AAPG Bulletin*, 41, 950-952
- Pironon J., Canals M., Dubessy J., Walgenwitz F., Laplace-Builhe C. (1998) Volumetric reconstruction of individual oil inclusion by confocal scanning laser microscopy. *European Journal of Mineralogy*, 10, 1143-1150.
- Pironon J., Thiery R., Ayt Ougougdal M., Beaudoin G., Walgenwitz F. (2001) FT-IR measurements of petroleum fluid inclusions: methane, n-alkanes and carbon dioxide quantitative analysis. *Geofluids*, 1, 2-10.
- Reese C. L. (1898) Petroleum inclusion in quartz crystals. *J. Am. Chem. Soc.*, 20, 795–797.
- Richard A., Morlot C., Penteley S., Giuliani G., Dyja-Person V., Pignatelli I., Beaudoin N., Legros H., Sterpenich J., Pironon J. (2017) Advances in 3D imaging and volumetric reconstruction of fluid inclusions by high resolution X-ray computed tomography. *ECROFI meeting, Nancy, France*, 23-29 June.
- Siljeström S., Lausmaa J., Sjövall P., Broman C., Thiel V., Hode T. (2010) Analysis of hopanes and steranes in single oil-bearing fluid inclusions using time-of-flight secondary ion mass spectrometry (ToF-SIMS). *Geobiology*, 8, 37–44.
- Smith M. (1994) Inclusion composition mapping of Earth's subsurface using collective fluid inclusion volatile compositions. *US patent #5,328,849*, 25 p.
- Volk H., Fuentes D., Fuerbach A., Miese C., Koehler W., Bärsch N., Barcikowski S. (2010) First on-line analysis of petroleum from single inclusion using ultrafast laser ablation. *Organic Geochemistry*, 41, 74–77.
- Von Nordenskjöld N. (1886) Vorläufige Mitteilungen über erneuerte Untersuchungen der Flüssigkeitseinschlüsse im brasilianischen Topas. *N Jahrb Mineral I*:242.
- Wahler W. (1956) Über die in Kristallen eingeschlossenen Flüssigkeiten und Gase. *Geochimica et Cosmochimica Acta*, 9, 105-135.

## Different modes of fluid phase separation in a single hydrothermal fluid?

John RIDLEY

Department of Geosciences, Colorado State University, Fort Collins, Colorado, U.S.A.

E-mail: jridley@colostate.edu

Figure 1 shows how a low- to moderate salinity aqueous fluid that includes a minor component of carbonic gas ( $\text{CO}_2$ ,  $\text{CH}_4$ ) can undergo phase separation at magmatic or near magmatic temperatures and at 'mesothermal' temperatures. Although our knowledge from experimental data and their extrapolation to equations of state of phase relations and vapour-liquid equilibrium in this generic three-component system is far from complete, it is apparent that the products of phase separation in the two scenarios will be very different. At near-magmatic temperatures, tie lines across the two-phase field join high and low salinity fluids, whereas at mesothermal temperatures in contrast the two fluids are high and low  $X_{\text{CO}_2}$ , but with little difference in aqueous phase salinity.

If we assume hydrothermal fluid flow is broadly upwards, a low-salinity aquo-carbonic fluid most likely enters the two-phase field at high temperatures through pressure drop, whereas loss of temperature and/or pressure may cause phase separation at mesothermal temperatures. Following the arguments and constructions of Ramboz et al (1982), we determine that at high temperatures a high-salinity brine would condense from the mixed fluid with little change in  $X_{\text{CO}_2}$  of the dominant fluid, whereas at mesothermal temperatures progressive temperature or pressure drop would cause a gas-rich fluid with  $X_{\text{CO}_2}$  between about 0.5 – 1.0 to exsolve and the dominant fluid would evolve to lower  $X_{\text{CO}_2}$  with little change in salinity.

These principles are applied to understanding relations between and implications of multiple fluid types in the mid-Cretaceous gold deposits of the Tintina Gold Province (TGP) of interior Alaska and adjacent Yukon Territory. The deposits in the Province include: Intrusion Related Gold Deposits (IRGD's) which comprise sheeted quartz vein sets in and around cupolas of penecontemporaneous granitic intrusions (Fort Knox, Scheelite Dome), and; 'orogenic' gold quartz veins in brittle-ductile to ductile shear zones in metamorphic rocks, along the contacts between metamorphic rocks and intrusions, or within intrusions (Pogo, Estes Dome). A magmatic-hydrothermal fluid source is universally proposed for the IRGD's, whereas a metamorphic fluid source is implied for the 'orogenic' deposits in metamorphic host rocks, and the origins of the fluids in the shear zones spatially associated with intrusions are debated. All deposits are however chemically and mineralogically similar, all apparently formed within a restricted time period of a few million years, and veins contain similar types of fluid inclusions

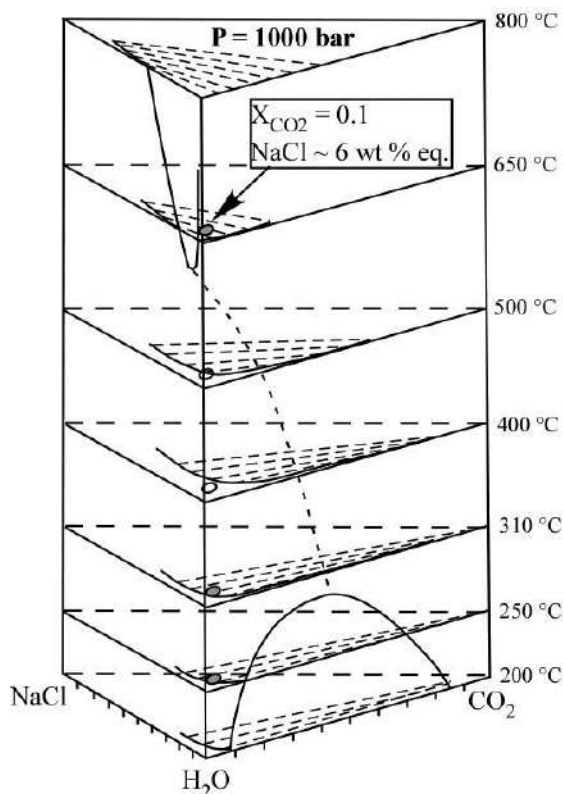


**Figure 1.** Two-phase field and tie lines (long dashes) across the solvus in the system  $\text{H}_2\text{O}-\text{CO}_2-\text{NaCl}$  at different temperatures and 1 kbar, after Duan et al (1995). Solvi for the two-phase systems are shown on prism faces; consolute curve as dashed line. A low-salinity aqueous fluid with minor  $\text{CO}_2$  may fall in the two-phase field at near magmatic temperatures and at mesothermal temperatures, but will separate into markedly different end-members at these P-T conditions.

Low-salinity aquo-carbonic fluids are dominant as interpreted primary or pseudosecondary fluid inclusions at essentially all the gold deposits. The composition of the fluid inclusions of this type varies somewhat systematically across the different settings, and what additional fluid inclusion types are recorded also varies. The aquo-carbonic fluids in shear-zone hosted deposits that formed at relatively low temperatures and pressures have lower  $X_{\text{CO}_2}$  at similar  $X_{\text{NaCl}}$  and are in many cases two-phase ( $\text{L}_{\text{H}_2\text{O}}\text{-V}_{\text{CO}_2}$ ) rather than three-phase ( $\text{L}_{\text{H}_2\text{O}}\text{-L}_{\text{CO}_2}\text{-V}_{\text{CO}_2}$ ). Carbonic-rich aquo-carbonic fluids are almost universally recorded except in some higher-temperature vein deposits. Saline fluids, with or without a carbonic vapor phase, are recorded in some IRGD's (not Fort Knox), and in a few shear-zone hosted deposits that are in or near to granitic intrusions. Based on co-existence in fluid-inclusion assemblages, both low- and high  $X_{\text{CO}_2}$  fluid pairs and pairs of high salinity fluids and low-salinity carbonic fluids have been invoked as immiscible fluid pairs at different deposits (e.g. McCoy et al., 1997; Baker and Lang, 2001).

In view of the tie-lines across the solvus in the  $\text{H}_2\text{O-CO}_2\text{-NaCl}$  system at different temperatures, both proposals for immiscible fluid pairs can be valid. We do not need to invoke either different 'source' fluid, or variable source composition with variable pressure of formation (Baker and Lang, 2001). Rather, we can explain the range of fluid types in the veins as being results of different P-T pathways of a single low-salinity aquo-carbonic fluid derived from a source at magmatic or near magmatic temperatures at a few kilobars pressure, in a similar fashion as proposed for fluid variability in porphyry-epithermal ore systems by Heinrich (2007). Fluid that rises through the crust with little loss of temperature may intersect the solvus at near magmatic temperatures and exsolve a brine. Fluids that thermally equilibrate with wallrock on migration would meet the solvus only at mesothermal temperatures. On reaching the solvus, these latter fluids would progressively lose  $\text{CO}_2$  to a vapor phase on progressive migration upwards through the crust.

#### REFERENCES

- Baker, T. and Lang, J. R. (2001) Fluid inclusion characteristics of intrusion-related gold mineralization, Tombstone-Tungsten magmatic belt, Yukon Territory, Canada. *Mineralium Deposita* 36, 563-582.
- Duan, Z., Møller, N. and Weare, J. H. (1995) Equation of state for  $\text{NaCl-H}_2\text{O-CO}_2$  system: Prediction of phase equilibria and volumetric properties. *Geochimica et Cosmochimica Acta* 59, 2869-2882.
- Heinrich, C. A. (2007) Fluid-fluid interactions in magmatic-hydrothermal ore formation. *Reviews in Mineralogy and Geochemistry* 65, 363-387.
- McCoy, D., Newberry, R. J., Layer, P., DiMarchi, J. J., Bakke, A., Masterman, J. S. and Minehane, D. L. (1997) Plutonic-related gold deposits of interior Alaska. *Economic Geology Monograph* 9, 191-241.
- Ramboz, C., Pichavant, M. and Weisbrod, A. (1982) Fluid immiscibility in natural processes: use and misuse of fluid inclusion data II. Interpretation of fluid inclusion data in terms of immiscibility. *Chemical Geology* 37, 29-48.

## Redox evolution of seawater in the Late-Permian Zechstein Basin: implications from redox-sensitive trace elements in fluid inclusions in halite

Eszter SENDULA<sup>1</sup>, Benjamin C. GILL<sup>1</sup>, J. Donald RIMSTIDT<sup>1</sup>, Tim K. LOWENSTEIN<sup>2</sup>, Javier GARCÍA-VEIGAS<sup>3</sup>, Robert J. BODNAR<sup>1</sup>

<sup>1</sup>Fluids Research Laboratory, Department of Geosciences, Virginia Tech, Blacksburg, Virginia, U.S.A.

<sup>2</sup>Department of Geological Sciences and Environmental Studies, Binghamton University, New York, U.S.A.

<sup>3</sup>Scientific and Technological Centers, University of Barcelona, Spain

E-mail: [seszter1@vt.edu](mailto:seszter1@vt.edu)

Oceanic Anoxic Events (OAE) are thought to be partly responsible for mass extinction events and subsequent slow recovery of marine ecosystems during Earth's history (Bond & Grasby, 2017). Minor and trace elements that show variations of valence state, isotope fractionation and solubility as a function of redox conditions are extensively used as paleoredox proxies. The concentrations of trace elements in sedimentary rocks are indirect indicators of the redox state of seawater at the time of deposition, but can be subject to changes due to post-depositional remobilization during diagenesis (Tribouillard et al., 2006). However, analysis of primary fluid inclusions in evaporite minerals (e.g. gypsum, halite) can provide direct information about the chemical composition of evaporating seawater and have been used to document changes in major ion concentration of paleo-seawater during the Phanerozoic Eon (Lowenstein et al., 2014).

The goal of this study is to develop a methodology to quantify ratios of minor and trace elements (Rb, Sr, Mo, Ba, Li, B, V, U, Fe, Mn, Se, Cr, Cu) in paleo-seawater based on Laser Ablation Inductively Coupled Plasma Mass Spectrometer (LA-ICP-MS) analysis of primary fluid inclusions in marine halites, and evaluate whether the element ratios may be related to redox conditions. The samples used to develop and test the methodology are from Przyborów IG3 borehole (N51°47'59.27"–E15°46'16.27") from the Polish sector of the European Southern Permian Basin, and contain halite samples from all four major Zechstein evaporate cycles (PZ1 to PZ4). Previous studies of primary fluid inclusions from these halite samples by García-Vegías et al. (2011) suggests that the major-ion chemistry of the seawater changed from sulfate-rich brines, similar in composition to modern evaporated seawater, to sulfate-depleted (calcium-rich) brines during the latest Permian. This change coincides with a drop in  $\delta^{34}\text{S}$  and was interpreted to be the result of overturn of anoxic sulfidic deep-waters that coincides with the Permian–Triassic mass extinction event. Since iron and manganese are more soluble in water under reducing conditions than under oxidizing conditions, and uranium, molybdenum and vanadium behave in the opposite manner, we expect to see changes in measured redox-sensitive trace element ratios Fe/U, Mn/U, Fe/V, Mn/V, Fe/Mo, Mn/Mo and Mn/Fe as a function of change in redox conditions.

Major, minor, and redox sensitive trace elements of 25-100  $\mu\text{m}$  single fluid inclusions were measured using LA-ICP-MS at Virginia Tech. The selected fluid inclusions are in primary growth zones of halite, contain only a single phase (brine) and have negative crystal shapes. Note that the results and interpretations presented below assume that the trace elements being analyzed behave conservatively and that ratios in seawater are little affected by earlier precipitation of carbonate and gypsum. However, to our knowledge, experimental studies to confirm this assumption have not been undertaken and important future work will attempt to determine the behavior of redox sensitive elements during seawater evaporation.

Our preliminary data show significantly higher ratios of Fe/U, Mn/U, Fe/V, Mn/V, Fe/Mo and Mn/Mo in halite samples with sulfate-depleted (calcium-rich) brines in the PZ2 and lower PZ3 cycles compared to samples with sulfate-rich brines in the PZ1, upper PZ3 and PZ4 cycles (Figure 1.). We observe increasing ratios against Mn at the upper, overall more oxidized, sulfate-rich part of the section at 1170-1100 m depth. This can be explained by a gradual shift to relatively more reducing water compositions within the redox range where iron is still sequestered in a solid phase as ferric iron ( $\text{Fe}^{3+}$ ). This is consistent with the increasing Mn/Fe ratios, relatively constant Fe/U, Fe/V and Fe/U ratios and decreasing concentration of sulfate in this part of the section. The overall trends support the previous interpretation of a transition from relatively oxic to anoxic conditions (Ca-rich zone) and then back to relatively oxic conditions (upper  $\text{SO}_4$ -rich zone) concluded by García-Vegías et al. (2011).

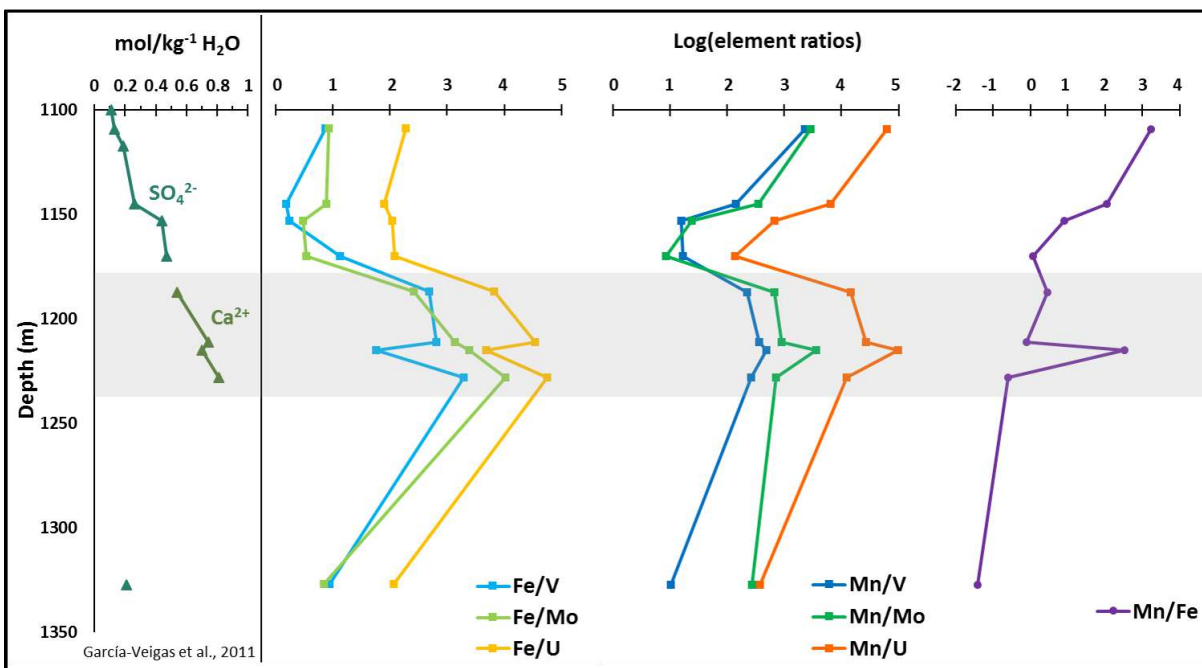


**Figure 1.** Trace element ratios in primary fluid inclusions in Late-Permian halite from the Polish sector of the European Southern Permian Basin. The increase in element ratios in the part of the section, which is characterized by sulfate-depleted (calcium-rich) major ion chemistry (shaded), is in agreement with the previous interpretation of a redox change in the basin to a more reducing environment.

#### REFERENCES

- Bond, D.P.G., Grasby, S.E. (2017) On the causes of mass extinctions, *Palaeogeography Palaeoclimatology Palaeoecology* 478, 3-29.
- García-Veigas, J. et al. (2011) Zechstein saline brines in Poland, evidence of overturned anoxic ocean during the Late Permian mass extinction event, *Chemical Geology* 290 (3-4), 189-201.
- Lowenstein, T.K. et al. (2014) 8.21 - The geologic history of seawater, In: Turekian, K.K. (Ed.) *Treatise on Geochemistry* (Second Edition), (Elsevier, Oxford) 569-622.
- Tribouillard, N. et al. (2006) Trace metals as paleoredox and paleoproductivity proxies: An update, *Chemical Geology* 232, 12-32.

## ***Invited* – Determination of source rock facies of oils trapped in single inclusions by ToF-SIMS**

Sandra SILJESTRÖM<sup>1</sup>, Robert POTTORF<sup>2</sup>, Sebastien DREYFUS<sup>2</sup>, Stephen P. BECKER<sup>2</sup>

<sup>1</sup>Department of Materials and Chemistry, RISE Research Institutes of Sweden, Stockholm, Sweden

<sup>2</sup>ExxonMobil Upstream Research Company, Houston, Texas, U.S.A.

E-mail: [sandra.siljestrom@ri.se](mailto:sandra.siljestrom@ri.se)

Fluid inclusions are micron-scale fluid-filled cavities in rock, which record movement of past to present-day fluids (oil, gas, and water) through the rocks. By mechanical crushing followed by solvent or thermal extraction - gas chromatograph-mass spectrometer (GC-MS), detailed molecular and isotopic data of petroleum inclusions can be obtained, however, the crushing process does not discriminate between geochemical signatures of different fluid inclusion generations within same rock. It has been shown that, time-of-flight secondary ion mass spectrometry (ToF-SIMS) may be used to detect biomarkers in single inclusions (Siljeström et al. 2009, Siljeström et al., 2010). However, the interpretation of the ToF-SIMS spectra and application to single hydrocarbon inclusions molecular geochemistry remains challenging due to the lack of reference data on oils. To overcome this issue, well characterized oils from different source facies, thermal maturity and biodegradation level were analysed by ToF-SIMS and used to calibrate the instrument.

Results show that the ratio of dibenzothiophene to phenanthrene (DBT/Phen) compounds may be used as a hydrocarbon source facies indicator. This ratio successfully discriminates oils sourced from organic matter deposited in marine carbonate environment from oils generated from marine clastic source rocks. Additionally, the calculated ToF-SIMS ratios also show a linear relationship with the same ratios calculated from GC-MS data.

In addition to the DBT/Phen ratio, results have also been obtained from the phenanthrene ratio for the determination of maturity of oils. The results show that the ratio has to be calibrated separately for oils from different rock facies but then a linear relationship can be found between the ratio and increasing maturity.

To validate the DBT/Phen ratios for the analysis of single oil inclusions by ToF-SIMS, synthetic inclusions were formed in a KCl saturated solution using one of the oils from the marine clastic calibration suite. The DBT/Phen ratio was then calculated from ToF-SIMS spectra of the marine clastic oil trapped in the synthetic fluid inclusions and compared to the ratios of the calibration oil suites. Ratios obtained from standard inclusions are similar to the ones calculated for the marine clastic oil suite demonstrating that Phen/DBT ratio can be used on hydrocarbon inclusions, down to a size of 7  $\mu\text{m}$ , without significant matrix effects, and therefore, the calibration suite may be used to characterize the source facies of oils trapped in fluid inclusions. Using these results the origin of oils trapped in natural inclusions within the Elk Basin Field, Big Horn Basin, WY, USA and other locations were determined.

### REFERENCES

- Siljeström, S., Lausmaa, J., Sjövall, P., Broman, C., Thiel, V., Hode, T. (2010) Analysis of hopanes and steranes in single oil-bearing fluid inclusions using time-of-flight secondary ion mass spectrometry (ToF-SIMS). *Geobiology* 8, 37–44.
- Siljeström, S., Hode, T., Lausmaa, J., Sjövall, P., Thiel, V. (2009) Detection of organic biomarkers in crude oils using ToF-SIMS. *Organic Geochemistry* 40, 135-143.



## Invited – A magmatic flotation model that genetically links iron oxide–apatite (IOA) and iron oxide–copper–gold (IOCG) deposits

Adam C. SIMON<sup>1</sup>, Jaayke KNIPPING<sup>2</sup>, Martin REICH<sup>3</sup>, Fernando BARRA<sup>3</sup>, Artur P. DEDITIUS<sup>4</sup>, Laura BILENKER<sup>5</sup>, Tristan CHILDRESS<sup>1</sup>

<sup>1</sup>Department of Earth and Environmental Sciences, University of Michigan, Ann Arbor, Michigan, U.S.A.

<sup>2</sup>Institut für Mineralogie, Leibniz Universität Hannover, Germany

<sup>3</sup>Department of Geology and Andean Geothermal Center of Excellence (CEGA), FCFM, Universidad de Chile, Chile

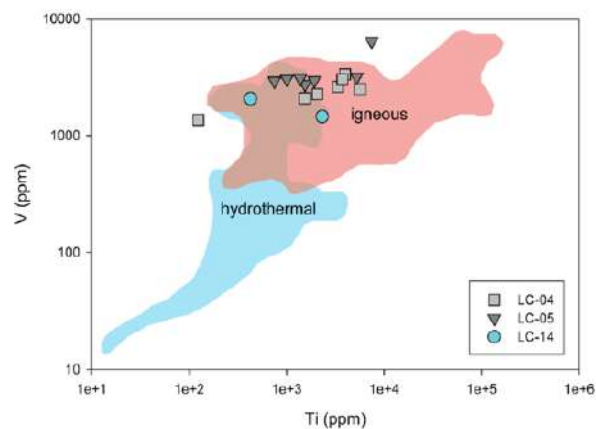
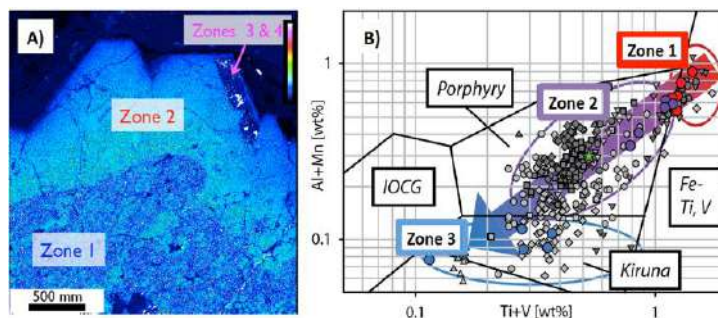
<sup>4</sup>School of Engineering and Information Technology, Murdoch University, Australia

<sup>5</sup> Department of Earth, Ocean, & Atmospheric Sciences, University of British Columbia, Canada

E-mail: simonac@umich.edu

Iron oxide – apatite (IOA) and iron oxide – copper – gold (IOCG) deposits are commonly spatially and temporally related to each other and to magmatism in subduction zone environments, and commonly hosted in magmatic rocks. Iron-oxides in both deposit types are Ti-poor relative to Fe-oxides in igneous rocks. Sulfides enriched in Cu and Au are present in both deposit types, although modally are more abundant in IOCGs. Mineralization is structurally controlled, notably in the Chilean Iron Belt (CIB) where mineralization occurred in regional-scale, trench-parallel faults. In general, temperatures of mineralization are 500 to >650 °C for magnetite and apatite in IOAs, and 400 – 550 °C and 300 – 400 °C, respectively, for Fe-oxides and sulfides in IOCGs. In this study, we interrogated the chemistry of magnetite, hematite, apatite, actinolite and pyrite from the Los Colorados IOA deposit, and magnetite and hematite from the Mantoverde IOCG deposit, both in the CIB, to develop a new model that explains the formation of IOA and IOCG deposits as a continuum resulting from combined magmatic and magmatic-hydrothermal processes.

EPMA X-ray mapping reveals that magnetite grains are strongly zoned. The concentrations of Ti, V, Al, and Mn are the highest in magnetite cores (zone 1) and progressively decrease toward the magnetite rims (zones 2 and 3), which is consistent with magnetite that crystallized at progressively cooler temperatures. When plotted on the magnetite discriminant diagram, the trace element signature of magnetite is consistent with growth from an evolving magmatic-hydrothermal fluid.



The concentrations of Ti and V in magnetite can be used to discriminate magnetite from among igneous, magmatic-hydrothermal and low-temperature hydrothermal sources. Magnetite from Los Colorados overlaps with igneous and magmatic-hydrothermal magnetite.

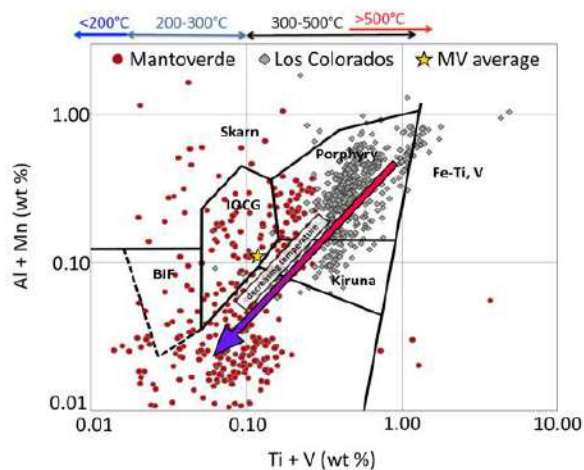
The values of  $\delta^{56}\text{Fe}$  and  $\delta^{18}\text{O}$  for magnetite samples from Los Colorados and Mantoverde plot within the global range for magnetite from igneous rocks, indicating that Fe and O in both deposits are derived from a magmatic source reservoir. Pyrite from Los Colorados contains elevated concentrations of Co, Ni, Cu, Au, Ag, and As, and is compositionally similar to pyrite from the Mantoverde and

Ernest Henry IOCG deposits, and Aguablanca magmatic Cu-Ni sulfide deposit. The trace element characteristics of pyrite from Los Colorados are consistent with an intermediate to mafic magma source for metals in pyrite.

$\Delta^{18}$ actinolite-magnetite from Los Colorados is 4.10‰, which yields a calculated minimum formation temperature of 630 °C. The  $\delta D$  values of magnetite (-53.5 ± 1.5‰) and actinolite (-59.3 ± 1.7‰) indicate a mantle source for H. Apatite grains from Los Colorados are zoned with respect to halogens and water. The highest F concentrations are in grain cores, and systematically the Cl/F ratio increases toward grain boundaries. Chlorine is also enriched proximal to cracks. The highest F concentrations overlap F-rich apatite crystallized from silicate melt, and the highest Cl concentrations overlap apatite crystallized from magmatic-hydrothermal fluid. Halite-saturated fluid inclusions are present in zone 2 rims of magnetite grains from Los Colorados. The inclusions are small, typically <5µm, and indicate that magnetite zone 2 grew in equilibrium with a brine. The concentrations of [Al + Mn] vs. [Ti + V] in magnetite from Los Colorados and Mantoverde are consistent with magnetite crystallization from a cooling magmatic-hydrothermal fluid in both deposits.

These data led to the development of the following new genetic model that explains IOA and IOCG deposits as a single continuum that forms by a combination of magmatic and magmatic-hydrothermal processes:

- 1) Magnetite and apatite microlites crystallize as near-liquidus phases in oxidized, intermediate-mafic silicate melts. Magmatic magnetite will be enriched in trace elements such as Ti, V, Mn and Al. Magmatic apatite will be enriched in F, and have a high F/Cl ratio.
- 2) During magma decompression, magnetite and apatite surfaces promote nucleation of gas bubbles from the silicate melt, and bubbles nucleate on the surface of these crystals (demonstrated experimentally). As volatile exsolution proceeds during decompression, the bubbles coalesce and sweep up magnetite and apatite microlites, forming a crystal-fluid suspension. The bulk density of the fluid suspension is less than the density of the surrounding magma as long as the suspension contains ≤37 vol% microlites, and the suspension will ascend buoyantly via channels that develop as the magma solidifies.
- 3) Chlorine, S, P and metals (Cu, Au, Co, Ni) partition efficiently from the silicate melt to the fluid. Experiments show that the fluid will have a high Co/Ni ratio. The magmatic-hydrothermal fluid chemistry will be dominated by FeCl<sub>2</sub>, KCl and NaCl. Experiments indicate that at 800 °C and 140 MPa the fluid contains ~6 wt% Na, ~11 wt% K and ~7 wt% Fe. Model calculations indicate that as the fluid ascends and decompresses, the concentrations of Na and K increase, whereas Fe decreases. Thus, during ascent, magnetite microlites continue to grow, sourcing Fe from the decompressing and cooling magmatic-hydrothermal fluid. Likewise, apatite continues to grow, becoming more Cl-rich as it grows from the magmatic-hydrothermal brine. This is consistent with the presence of brine inclusions and decreasing concentrations of Ti, V, Mn and Al in magnetite zone 2, and increasing core-to-rim Cl/F ratios of apatite at Los Colorados. Increasing Na and K concentrations of the brine during decompression reduce the potential for sodic and potassic alteration, neither of which is observed at Los Colorados.
- 4) During ascent along pre-existing structurally enhanced dilatant zones that act as conduits (e.g., faults, fractures zones, brecciated host rocks, volcanic feeder zones, caldera systems, etc.), magnetite and apatite will reach neutral buoyancy and drop out of the fluid suspension to form a magnetite-apatite ore body that is concordant with the fault, and depending on the local porosity and permeability of the host rock, the fluid suspension may percolate laterally into the host rock forming disseminated mineralization, which is commonly observed in IOAs.
- 5) The fluid that cools at this level of neutral buoyancy can precipitate sulfides, notably pyrite that will scavenge metals from the fluid, resulting in pyrite with a high Co/Ni ratio.
- 6) For a rapidly ascending fluid, a significant amount of the suspension will continue to ascend. As the fluid evolves to lower pressure and temperature, it precipitates magnetite (and hematite if the fluid becomes oxidized) and sulfides to form an IOCG deposit.



## Rock volatiles stratigraphy: A tool for petroleum exploration and production

Michael P. SMITH

*Advanced Hydrocarbon Stratigraphy, Inc, 2931 W21st, Tulsa, OK 74107, USA*

*E-mail: ahstrat.aol.com*

Amazing as it may seem, there is considerable uncertainty as to the nature of the rocks and fluids drilled by oil and gas wells, even today in 2018. Well logs can be misleading. Many of today's pay zones are considered low visibility. This is especially a problem in sediments bearing fresh non-saline water. Also in this era of low oil prices, many wells are not logged to save money. This is particularly true in horizontal wells, as they are more expensive, difficult, and time consuming to log. Tool loss is also a higher risk in horizontal wells, and the cost of replacing expensive logging tools falls on the company drilling the well, and usually not on the well logging company.

The low cost alternative to well logs is to analyze drilling mud and cuttings, free drilling by-products, to determine the location of pay zones, the nature of the product, and the quality of the reservoir. The desire to do this is not new. Although this was difficult to realize in the past, it is even more difficult today with PDC (polycrystalline diamond compact) bits that result in cuttings fragments often less than 1 millimeter in diameter.

I invented Fluid Inclusion Stratigraphy (FIS), now available through Schlumberger, and Fluid Inclusion Volatiles (FIV), now a proprietary ExxonMobil technology, to allow rapid, large scale mapping of Fluid Inclusions in cuttings as a way of gaining otherwise unavailable insights into petroleum systems.

Although these technologies have proven valuable in reducing exploration and production risks, they have not proven successful in mapping present day pay zones. It is my experience that petroleum inclusions tend to form more in water dominated sediments than in zones of high oil or gas saturation. Also, some oil fields occur in young clastic sediments, at relatively shallow depths, in tectonically quiet basins, such as offshore Gulf of Mexico, where oil inclusions are not to be found. And the advent of widespread PDC bit drilling, with often sub-millimeter sized cuttings particles, and often disrupts whatever inclusions were originally present in the cuttings samples.

Further, I designed the FIS and FIV analytical processes to analyze volatiles only from fluid inclusions. Other sources of volatiles are removed from the samples by a combination of heating and vacuum extraction. This is particularly important for cuttings from wells drilled using Oil Based Mud (OBM). Otherwise the OBM signal overwhelms the FI signal. Any non-inclusion volatiles that survive these treatments are characterized before inclusion volatiles are introduced to the mass spectrometer, and are mathematically subtracted during data reduction.

However, mapping present day pay zones using cuttings requires analyzing today's pore fluids, instead of discarding them via heat and vacuum and mathematically subtracting them from the result.

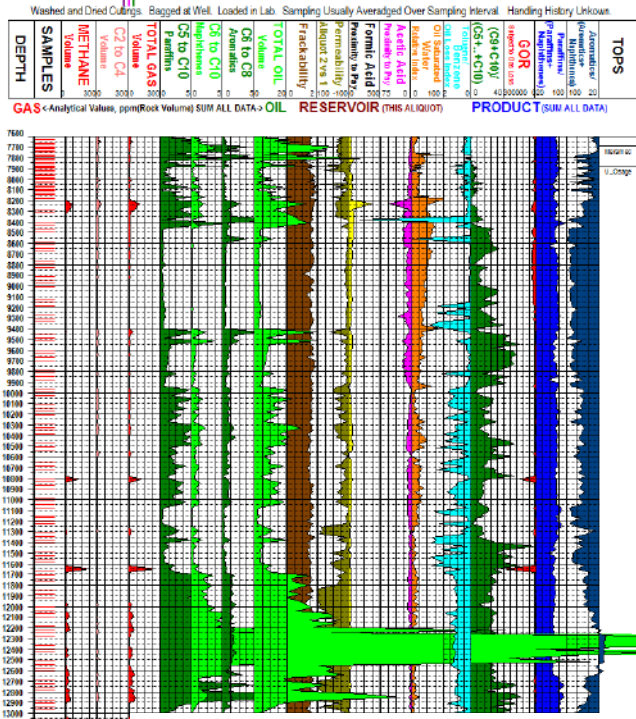
I have developed a gentle extraction and analyses technology called Rock Volatiles Stratigraphy (RVStrat<sup>sm</sup>, patents pending) aimed at analyzing all the volatiles in a cuttings sample. By design, this technology is not limited to Fluid Inclusions, but analyzes all extractable volatiles in a sample.

I am presenting this technology at PACROFI in part because it is an outgrowth of my work on analyzing FI volatiles, and in part because it has become obvious to me that mapping petroleum inclusions does not map pay zones.

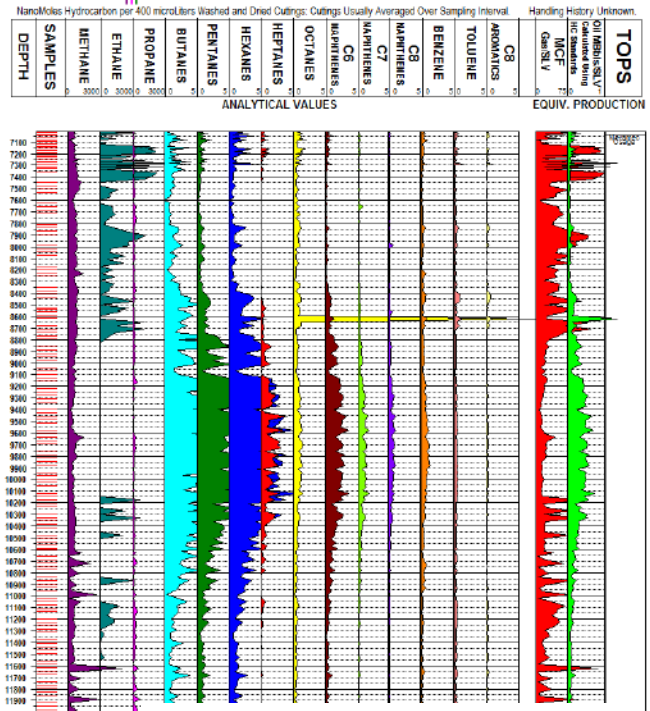
RVStrat<sup>sm</sup> analyzes volatiles in petroleum inclusions, but it also analyzes volatiles in cracks, tight pores, as well absorbed and adsorbed volatiles. To accomplish my goals I built a Cryo Trap Mass Spectrometer (CT/MS) system. Volatiles are extracted from each individual sample at two pressures, 50 and 5 millibars and frozen onto liquid nitrogen (LN<sub>2</sub>) traps, and analyzed by allowing the frozen volatiles to sublime and enter the mass spectrometer according to their sublimation points under high vacuum. This provides a measure of compound separation and quantitation similar to that obtained in GC/MS systems. However, the CT/MS system is non-selective. All compounds that can be extracted and frozen are analyzed.

Examples of RVStrat<sup>sm</sup> logs from PDC cuttings from 4 horizontal wells are shown on the next page. They show responses indicative of: oil filled fractures; changes in rock properties; faulting; pay zone identification. These and other examples will be discussed in detail.

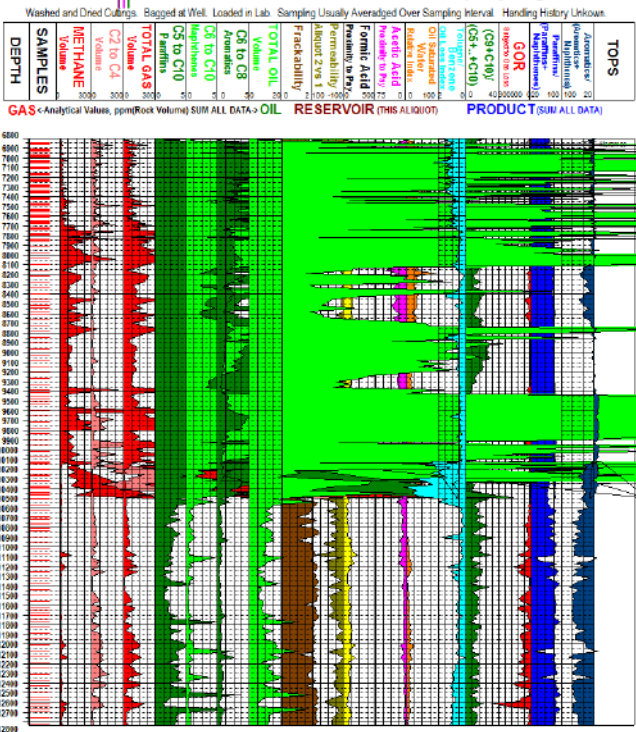
**Advanced Hydrocarbon Stratigraphy** | **Oil Filled Fracture Identification Example**  
**AHS Loaded-In-Lab Rock-Volatiles Property-Log**



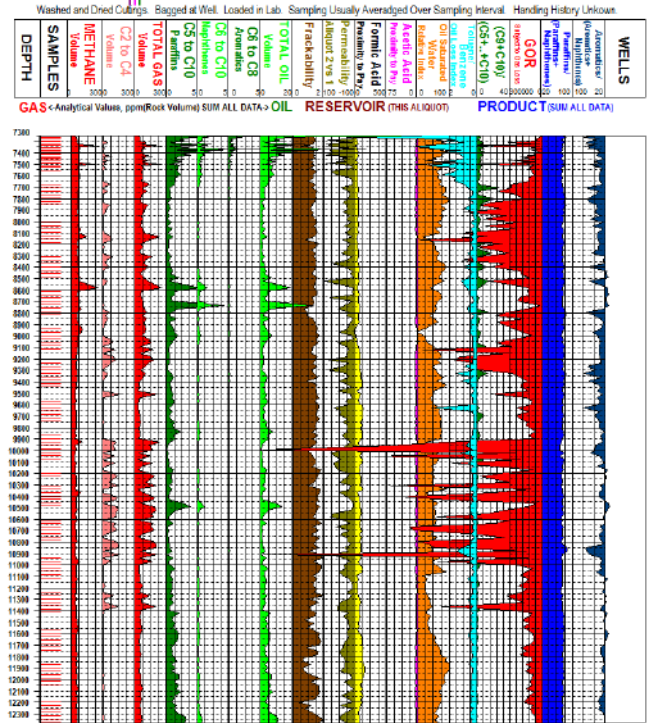
**Advanced Hydrocarbon Stratigraphy** | **Rock Properties Identification Example**  
 Fixed HC Scales, SLV=Standard Lateral Volume=4500" long, Radius=100"



**Advanced Hydrocarbon Stratigraphy** | **Fault Identification Example**  
**AHS Loaded-In-Lab Rock-Volatiles Property-Log**



**Advanced Hydrocarbon Stratigraphy** | **Pay Zone Identification Example**  
**AHS Loaded-In-Lab Rock-Volatiles Property-Log**



AHS, 2931 W 21st St, Tulsa, OK 74107 USA AHSTRAT@AOL.COM  
 Phone: (01)-918-583-2474 Mobil: (01)-918-671-0355 FAX: (01)-918-583-2475

AHS, 2931 W 21st St, Tulsa, OK 74107 USA AHSTRAT@AOL.COM  
 Phone: (01)-918-583-2474 Mobil: (01)-918-671-0355 FAX: (01)-918-583-2475

## Determination of F concentrations in ore-stage MVT fluids through SEM-EDS analysis of fluid inclusion decrepitates

Sarah E. SMITH-SCHMITZ, Martin S. APPOLD

Department of Geological Sciences, University of Missouri, Columbia, Missouri, U.S.A.

E-mail: ses7f1@mail.missouri.edu

Most Mississippi Valley-type (MVT) deposits consist principally of sulfide minerals with negligible to moderate quantities of fluorite (Leach and Taylor, 2009). However, some MVT districts, such as the Illinois-Kentucky district, are fluorite-dominant, suggesting different chemical conditions for mineralization. One hypothesis is that fluorite-dominant MVT deposits formed from anomalously F-rich fluids compared to typical sedimentary brines and MVT ore fluids. A corresponding hypothesis is that the fluids that formed fluorite-dominant MVT deposits derived their F from local coeval magma bodies. Support for these hypotheses comes from Kenderes and Appold (2017), who found F concentrations ranging from 680 to 4300 ppm in sphalerite-hosted fluid inclusions from the Illinois-Kentucky district, which is closely associated temporally with local ultramafic magmatism. In contrast, Kenderes and Appold (2017) found fluid inclusions from the fluorite-poor Tri-State district, which has no known relationship to contemporaneous magmatism, to contain undetectable concentrations of F, i.e. less ~100 ppm. However, in order to have more confidence in these hypotheses, ore fluid F concentrations from more MVT deposits, both magmatic and amagmatic, must be determined. The purpose of the present study is to carry out such a survey.

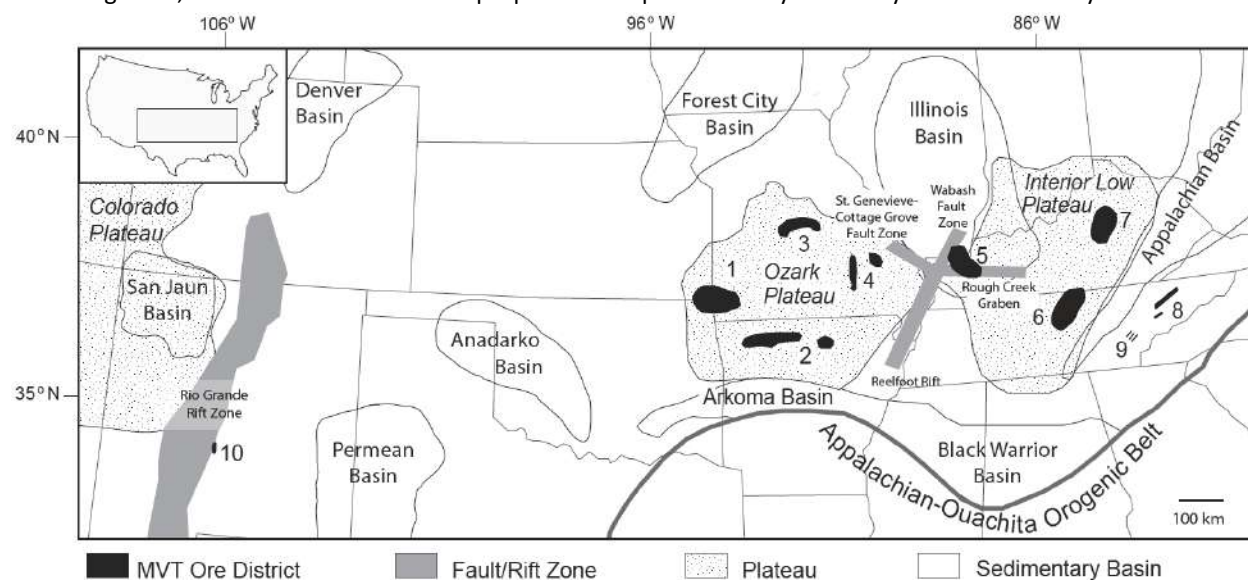


**Figure 1.** Map showing locations of MVT districts included in this study, other major MVT districts, and major geologic features: Tri-State district (1), Northern Arkansas district (2), Viburnum Trend, Missouri district (4), Illinois-Kentucky district (5), Central Tennessee district (6), Central Kentucky district (7), East Tennessee district (8), Sweetwater Tennessee district (9), and Hansonburg, New Mexico district (10). Modified from Pelch et al. (2015).

Five MVT districts with variable fluorite:sulfide abundances and from diverse geologic settings have been selected for the present study (Fig. 1). Hansonburg, New Mexico is a rift-associated fluorite-dominant district that resembles the Illinois-Kentucky district. Sweetwater, Tennessee is a fluorite-dominant district that has no known genetic association with contemporaneous igneous activity. The Central Kentucky and Central Tennessee districts have moderate fluorite:sulfide mineral ratios. The Viburnum trend of the Southeast Missouri district is sulfide-dominant and contains negligible fluorite (Roeder et al. 1968; Kyle, 1976; Anderson et al. 1982; Misra et al., 1989; Voss et al., 1989).

Samples of sphalerite have been selected for fluid inclusion analysis from the Central Tennessee, Central Kentucky, Sweetwater, and Viburnum trend districts. Drusy quartz that paragenetically overlaps fluorite

mineralization has been selected for the Hansonburg district, as sphalerite predates fluorite mineralization in this deposit. Doubly polished thin sections of the samples have been examined petrographically to identify primary fluid inclusion assemblages. Microthermometry of the primary fluid inclusion assemblages has been performed on chips made from the thin sections. The chips will be thermally decrepitated and the resulting solute mounds (Fig. 2) will be analyzed using an SEM equipped with dual, co-planer EDS detectors. The element concentrations measured in the decrepitate mounds will be converted to mass ratios relative to chloride (F/Cl ratios).

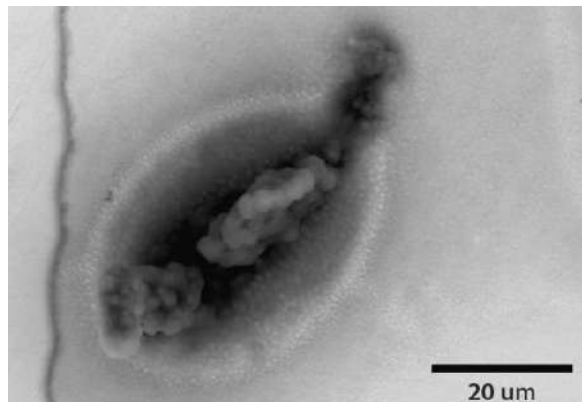


**Figure 2.** Back scattered electron image of a fluid inclusion decrepitate mound from sample CTEW1BM4-1, Central Tennessee.

Instrument and mineral specific calibrations curves, necessary to convert the measured F/Cl ratios to fluid inclusion fluoride concentrations, have been produced using a series of model ore fluid standards with average major element MVT ore fluid composition (Wenz et al. 2012) and dissolved fluorine concentrations from 10 to 2000 ppm. Salinities derived from microthermometry data and district specific reported chlorine concentrations will be used with the F/Cl calibration curves to determine absolute fluid inclusion fluorine concentrations and by implication, ore fluid fluorine concentrations for the districts.

The predicted ore fluid F concentrations from the MVT districts in this study, in addition to those reported by Kenderes and Appold (2017), will be considered in relation to the relative abundance of fluorite and coeval igneous rocks in the MVT districts. The results should help clarify to what degree ore fluid F concentration and coeval magmatism control fluorite abundance in MVT deposits.

#### REFERENCES

- Kenderes S.M. and Appold M.S. (2017) Fluorine concentrations of ore fluids in the Illinois-Kentucky district: evidence from SEM-EDS analysis of fluid inclusion decrepitates, *Geochim. Cosmochim. Acta* 210, 2017, 132–151.
- Kyle, J. R. (1976) Brecciation, alteration, and mineralization in the Central Tennessee zinc district. *Econ. Geol.* 71, 892-903.
- Leach, D. L. and Taylor, R. D. (2009) Mississippi Valley-type lead-zinc deposit model. US Geological Survey Open-File Report, 1213.
- Misra, K. C., Kopp, O. C., Paris, T. A., and Linkous, M. A. (1989). Mississippi Valley-type fluorite-barite-sphalerite mineralization in the Sweetwater district, Tennessee. *Carbonates and Evaporites* 4, 211.
- Pelch, M. A., Appold, M. S., Emsbo, P., & Bodnar, R. J. (2015). Constraints from Fluid Inclusion Compositions on the Origin of Mississippi Valley-Type Mineralization in the Illinois-Kentucky District. *Economic Geology*, 110, 3, 787-808.
- Roedder, E., Heyl, A. V., & Creel, J. P. (1968). Environment of ore deposition at the Mex-Tex deposits, Hansonburg district, New Mexico, from studies of fluid inclusions. *Economic Geology*, 63, 336-348.
- Voss R. L., Hagni R. D. and Gregg J. M. (1989) Sequential deposition of zoned dolomite and its relationship to sulfide mineral paragenetic sequence in the Viburnum Trend, southeast Missouri eds. S. J. Mazzullo and J. M. Gregg. *Carbonates and Evaporites* 4, 195–209.
- Wenz, Z. J., Appold, M. S., Shelton, K. L., & Tesfaye, S. (2012). Geochemistry of Mississippi Valley-type mineralizing fluids of the Ozark Plateau: A regional synthesis. *American Journal of Science*, 312, 1, 22-80.

## Fluid inclusion evidence for methane-dominated thermochemical sulfate reduction in the North German Basin

Marta SOŚNICKA, Volker LÜDERS

GFZ, German Research Centre for Geosciences, Potsdam, Germany

E-mail: sosnicka@gfz-potsdam.de

Hydrogen sulfide (H<sub>2</sub>S) is a common non-hydrocarbon gas in natural evaporate-hosted reservoirs. It can be produced by thermal decomposition of sulfur-bearing organic matter in kerogens, thermal cracking of sulfur-containing crude oil or by biotic/abiotic redox reactions between sulfate and hydrocarbons (e.g. Orr, 1977). In low-temperature sedimentary environments (T<80°C) bacterial sulfate reduction (BSR) is the principle H<sub>2</sub>S-forming reaction. BSR causes large sulfur isotope fractionation between sulfate and sulfide ( $\Delta^{34}\text{S}$  sulfate-H<sub>2</sub>S), of up to -72‰, averaging -51‰ in natural systems (e.g. Rudnicki et al., 2001). At temperatures above 80°C most sulfate-reducing bacteria cease metabolism and at temperatures  $\geq 120^\circ\text{C}$  thermochemical sulfate reduction (TSR) is the major process generating H<sub>2</sub>S in deep subsurface reservoirs (e.g. Worden and Smalley, 1996; Machel, 2001). During TSR, hydrocarbons react with dissolved sulfate producing, e.g. H<sub>2</sub>S, CO<sub>2</sub>, elemental sulfur and water (e.g. Krooss et al. 2008). Fractionation between sulfate and sulfide ( $\Delta^{34}\text{S}$  sulfate-H<sub>2</sub>S) due to TSR strongly depends on temperature but is less intense compared to BSR (e.g. Seal, 2006). During the past 20 years many studies have been performed for a better understanding of this abiotic alteration process. Although much is understood about TSR, there is still some debate about e.g. reacting hydrocarbons. It has been shown that higher hydrocarbons react faster during

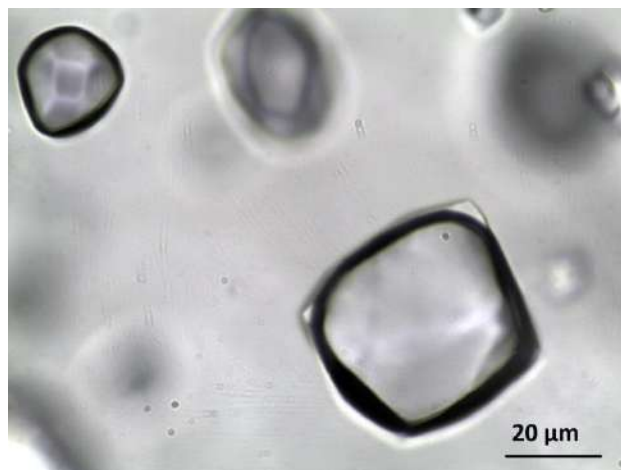


**Figure 1.** C-O-H-S±N-bearing gas inclusions hosted in fluorite.

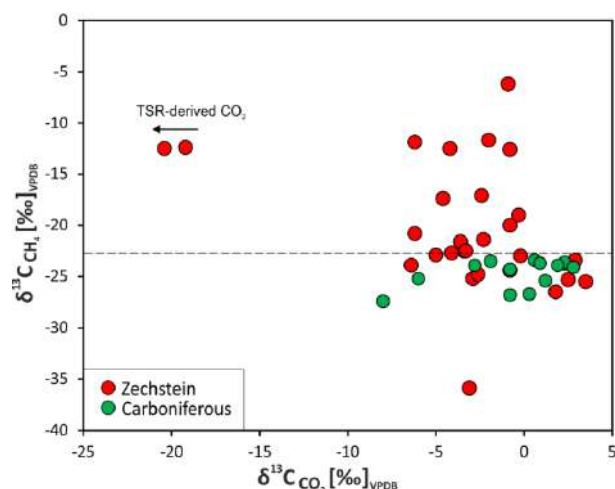


**Figure 2.** C isotopic compositions of fluid inclusion gases in Zechstein and Upper Carboniferous reservoirs. Samples plotting above the dashed trend line are largely fractionated due to TSR, whereas samples plotting below the line show low or no H<sub>2</sub>S content.

TSR than methane, however, in deep dry gas reservoirs CH<sub>4</sub> is the dominant reacting hydrocarbon (Cai et al., 2004).

In the North German Basin natural dry gases with high concentrations of hydrogen sulfide (5-35%) occur in deep Zechstein-2-Carbonate (Ca<sub>2</sub>) gas reservoir in the so-called "H<sub>2</sub>S Province". The latter is situated in the northern part of the Lower Saxony Basin (LSB) and adjacent Pompeckj Block (PB), in the southern part of the Zechstein Basin. The LSB and PB significantly differ in burial history and structural evolution (Bruns et al., 2013). High H<sub>2</sub>S content in this part of the North German Basin is considered to be derived by TSR (Krooss et al., 2008).

For this study core samples of fracture-fill mineralization hosted by Ca<sub>2</sub> carbonate were collected from boreholes drilled in the northern part of the LSB and adjacent PB. The studied samples host abundant gas-rich inclusions that contain complex C-O-H-S±N-mixtures (Figure 1) and co-genetically trapped aqueous two-phase brine inclusions. The latter show homogenization temperatures between 150 and 160°C. Gas-rich inclusions in fluorite yield low-pressure



## Invited – Mineral inclusion thermobarometry: A new approach to estimate the temperatures and pressures of hydrothermal ore formation

Matthew STEELE-MACINNIS<sup>1</sup>, Kyle T. ASHLEY<sup>2</sup>, Drew W. BARKOFF<sup>3</sup>

<sup>1</sup>Department of Earth & Atmospheric Sciences, University of Alberta, Edmonton, Alberta, Canada

<sup>2</sup>Department of Geology and Environmental Science, University of Pittsburgh, Pittsburgh, Pennsylvania, U.S.A.

<sup>3</sup>Department of Geoscience, University of Nevada Las Vegas, Las Vegas, Nevada, U.S.A.

E-mail: steelema@ualberta.ca

Pressure and depth of hydrothermal mineralization are important variables in determining the size, geometry and alteration style of mineral deposits. However, pressures of hydrothermal systems are commonly only loosely constrained, because traditional methods of thermobarometry have certain shortcomings when applied to hydrothermal veins and metasomatic rocks. An alternative and complementary approach, which shows promising agreement with paleodepths estimated from structural reconstruction and stratigraphy, involves Raman spectroscopic analysis of pressurized mineral inclusions, coupled with elastic modeling to restore the inclusions to entrapment temperature and pressure (Ashley et al., 2014). While this approach has recently become increasingly popular in the study of metamorphic terranes, few studies have applied this method to hydrothermal rocks. The approach has been previously tested at one hydrothermal skarn by Barkoff et al. (2017). Here we present additional testing of the technique, showing promising results at multiple hydrothermal skarns of the Yerington district, NV.

The conceptual model for this approach is as follows: mineral inclusions within rigid host minerals are

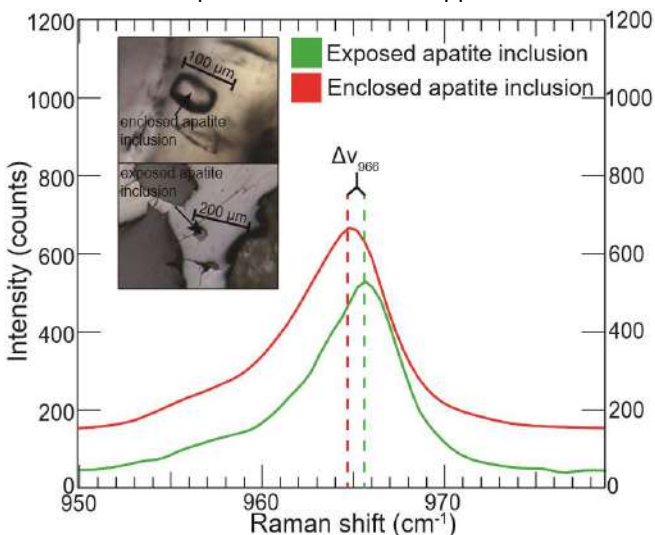


**Figure 1.** Raman peak shift of apatite inclusion in garnet from Casting Copper skarn, compared to the (1-atm) standard apatite peak position measured using an inclusion exposed to the surface by polishing. From Barkoff et al. (2017).

prevented from relaxing to ambient pressure owing to the mechanical constraints imposed by the surrounding host. This leads to some level of retained, or residual, pressure within the inclusion. The magnitude of retained pressure is indicated by the shift in the pressure-sensitive Raman peak position of the inclusion phase (Fig. 1; from Barkoff et al., 2017). Therefore, through Raman spectroscopy we constrain the peak shift relative to the peak position of a standard (at ambient pressure), and use this peak shift to estimate the retained pressure. We then apply an elastic model to calculate the pressure-temperature locus that satisfies mechanical equilibrium between inclusion and surroundings – that is, conditions at which internal and external pressure are equal. This approach allows us to estimate the conditions at which the inclusion was enclosed by the surrounding host.

The results by Barkoff et al. (2017) showed that, whereas mineral inclusions trapped in high-pressure metamorphic terranes commonly show positive retained pressures, mineral

inclusions trapped in relatively high-temperature, low-pressure hydrothermal settings may show *negative* (i.e., tensile) internal pressures. Nevertheless, the results by Barkoff et al. (2017) indicated that these negative pressures could be reliably used to estimate formation temperature and pressure, with results comparing favorably with previous estimates.

To test this method in the context of hydrothermal mineral deposits, we apply this approach at three skarns in the Ludwig area, Nevada (from shallowest to deepest): Casting Copper, Douglas Hill, and Hill 5923. Garnets at Casting Copper are andradite-rich and inclusions in garnet are predominantly apatite. At both of the deeper skarns,

garnets are andradite-grossular solid solutions, and host inclusions of apatite as well as quartz (Fig. 2), and calcite (at Douglas Hill). The occurrence of two or three different mineral inclusions together in the same garnet hosts at Douglas Hill and Hill 5923 enabled us to compare results obtained from multiple inclusion-host pairs, and combining the results obtained from multiple inclusion phases permits independent evaluation of both pressure and temperature simultaneously.

Raman spectroscopy shows that at ambient conditions, all three inclusion phases at all three skarns are under tension (negative pressures), and the magnitude of tension varies with pressure and temperature of formation. In particular, we note higher magnitudes of tension within inclusions hosted in garnet from the higher-temperature skarns. Magnitude of tension also differs between apatite, quartz and calcite inclusions from one locality, according to the different elastic properties of these three inclusion phases.

Based on our elastic modeling calculations, at inferred trapping temperatures of 400, 450 °C and 500 °C, respectively, pressure estimates based on apatite and calcite inclusions from all three deposits are in good agreement with stratigraphic paleodepth estimates. Quartz inclusions consistently yield higher pressures, compared to the other two inclusion phases. The intersections of results calculated using multiple inclusion phases simultaneously provides a reasonable independent match with both formation temperature *and* pressure, without requiring prior knowledge of the formation temperatures, although once again results that include quartz inclusions are somewhat higher, compared to the results based on intersections of apatite+calcite inclusions. These results generally reaffirm that Raman spectroscopy of mineral inclusions, combined with elastic modeling, is a promising method for thermobarometry of hydrothermal rocks, but suggest that apatite and calcite inclusions are better candidates whereas quartz is somewhat less clear. This latter result is broadly consistent with our previous findings for higher-pressure metamorphic rocks, which suggested that quartz inclusions tend to yield pressures higher than expected (Ashley et al., 2016) – likely because of as yet unaccounted for issues with regard to stress anisotropy within quartz inclusions.

In summary, although questions remain especially with regard to quartz inclusions, overall the results are encouraging, and apatite and calcite inclusions seem especially promising for thermobarometry of hydrothermal rocks. The next steps will be to apply this method to other, less well characterized skarns and other types of hydrothermal systems as well.

#### REFERENCES

- Ashley, K.T. et al. (2014) Geothermobarometric history of subduction recorded by quartz inclusions in garnet, *Geochem, Geophys, Geosyst* 15, 350-360.  
 Barkoff, D.W. et al. (2017) Pressures of skarn mineralization at Casting Copper, Nevada, USA, based on apatite inclusions in garnet, *Geology* 45, 947-950.  
 Ashley, K.T. et al. (2016) Quartz-in-garnet inclusion barometry under fire: Reducing uncertainty from model estimates, *Geology* 44, 699-702.

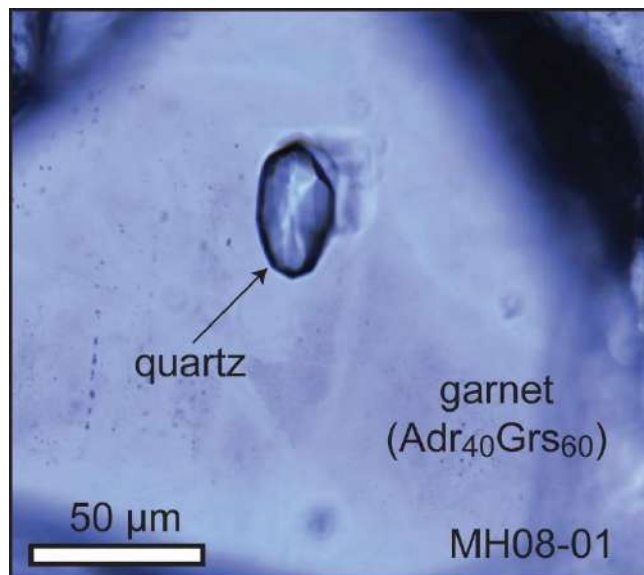


**Figure 2.** A quartz inclusion hosted in garnet from the Hill 5923 skarn.

## A model for composition and density of H<sub>2</sub>O-NaCl-CO<sub>2</sub> fluid inclusions

Matthew STEELE-MACINNIS

*Department of Earth & Atmospheric Sciences, University of Alberta, Edmonton, Alberta, Canada*

*E-mail: steelema@ualberta.ca*

Fluid inclusions approximated by the system H<sub>2</sub>O-NaCl-CO<sub>2</sub> are common in a wide variety of geologic settings. Therefore, tools to interpret the physico-chemical properties of these fluids from analytical data are needed. Several existing computer packages are widely used to interpret properties of such fluid inclusions, especially the Flincor/MacFlincor packages (Brown, 1989; Brown and Hagemann, 1995) and the CLATHRATES package (Bakker, 1997). Both have advantages and disadvantages. The main drawbacks of Flincor/MacFlincor are that these packages have not been updated in recent years and that they are now difficult to compile and run on modern PCs. The main drawback of CLATHRATES is that the programs must be re-executed for each individual inclusion, microthermometric (or other) data must be entered manually, and output data must be extracted from the resulting text files one-by-one, rendering interpretation and compilation of large datasets prohibitively time consuming. Both programs also incorporated some approximations and simplifications in the solver approach that, while generally not major issues, are worth revisiting in light of modern computational power and equations of state that permit full treatment of mass balance and isochoricity without simplifications.

This study presents a generic approach to determine these properties of H<sub>2</sub>O-NaCl-CO<sub>2</sub> inclusions, based on petrographic, microthermometric and/or Raman spectroscopic data, invoking constraints of mass balance and conservation of bulk molar volume. The algorithm is implemented using a combination of new correlation equations and existing equations of state. The approach is deliberately generic, accepting a range of possible input data types according to the observed petrographic, microthermometric and/or microanalytical properties of individual inclusions. Specifically, the approach can handle input data of the following types: 1)  $T_{m,clath} \leq T_{h,CO_2}$ ; 2)  $T_{m,clath} > T_{h,CO_2}$ ; 3)  $T_{m,clath} \geq T_{m,ice}$ ; and 4)  $T_{m,clath}$  &  $P_{m,clath}$  (Fall et al., 2011). For each type of input data, an additional constraint is provided either by the volume fraction of the carbonic portion (at any temperature, most commonly at room  $T$ ), or the total homogenization temperature. In each case, the procedure used in the calculation is based on simultaneously solving for the bulk composition and bulk density that satisfies phase equilibrium constraints at each observed phase change temperature ( $\pm$ pressure). As such, mass balance and isochoricity are explicitly maintained in the numerical method. The current implementation is valid for inclusions with salinity from zero to 24.2 wt% NaCl, and CO<sub>2</sub> concentration from 1.85 to 99.8 mol% CO<sub>2</sub> (relative to CO<sub>2</sub>+H<sub>2</sub>O).

The computer program is written in Visual Basic for Applications in Microsoft Excel. As such, the program allows fast calculation of large datasets that can be entered in spreadsheet format (output data are also written out in the same spreadsheet), with each row in the sheet corresponding to one inclusion. The program includes a main module for computing composition, density and isochore based on the input data of the various types outlined above. The program also includes tools for reconstructing and plotting phase boundaries (solvus lines) and isochore contour plots for a given composition. In addition, the program includes tools to calculate and plot the pressure-temperature trajectories of the inclusion during heating, to help visualize the observed microthermometric properties according to the phase diagram in pressure-temperature space. The program is available from the author upon request.

### REFERENCES

- Bakker, R. J. (1997) Clathrates: computer programs to calculate fluid inclusion V-X properties using clathrate melting temperatures. *Comp Geosci* 23, 1-18.
- Brown, P. E. (1989) FLINCOR: A microcomputer program for the reduction and investigation of fluid inclusion data. *Am Mineral* 74, 1390-1393.
- Brown, P. E., Hagemann, S. G. (1995) Macflincor and its application to fluids in Archean lode-gold deposits. *Geochim Cosmochim Acta* 59, 3943-3952.
- Fall, A. et al. (2011) Combined microthermometric and Raman spectroscopic technique to determine the salinity of H<sub>2</sub>O-CO<sub>2</sub>-NaCl fluid inclusions based on clathrate melting. *Geochim Cosmochim Acta* 75, 951-964.



## N<sub>2</sub>, CO<sub>2</sub>, and CH<sub>4</sub> fugacities determined for gas mixtures from 10-500 bars at 22 °C using Raman spectroscopy

D. Matthew SUBLETT Jr.<sup>1</sup>, Hector M. LAMADRID<sup>2</sup>, Matthew STEELE-MACINNIS<sup>3</sup>, Georg SPIEKERMANN<sup>4</sup>, Robert J. BODNAR<sup>1</sup>

<sup>1</sup>Fluids Research Laboratory, Department of Geosciences, Virginia Tech, Blacksburg, Virginia, U.S.A.

<sup>2</sup>Department of Earth Sciences, University of Toronto, Toronto, Ontario, Canada

<sup>3</sup>Department of Earth & Atmospheric Sciences, University of Alberta, Edmonton, Alberta, Canada

<sup>4</sup>Institut für Erd- und Umweltwissenschaften, Universität Potsdam, Potsdam, Germany

E-mail: dsublett@vt.edu

An ideal gas is one that assumes the individual gas molecules occupy no volume and do not interact with other gas particles. The partial pressures of individual gas components within an ideal gas mixture are related to the total pressure and mole fractions of the components according to:

$$P_i = X_i \cdot P \quad [1]$$

where  $P_i$  is the partial pressure of component  $i$ ,  $X_i$  is the mole fraction of component  $i$ , and  $P$  is the total pressure exerted on the gas mixture. In an ideal gas mixture, the sum of the partial pressures of each component is equal to the total pressure. At low pressures, many common gases can be approximated as ideal gases because there is sufficient space between molecules such that attractive and repulsive forces are adequately weakened and may be ignored in thermodynamic calculations. Thus, determining the mixing behavior of gases at low pressures is relatively simple. However, as pressure increases the individual molecules move closer together and the attractive or repulsive forces between molecules become too strong to reasonably be ignored. There is a new “effective” partial pressure for each component described as the fugacity of the gas components. The fugacity of a gas takes into account the non-ideality of the gas by scaling the partial pressure calculated in equation 1 by a dimensionless quantity known as the fugacity coefficient. The fugacity coefficient is equal to one for an ideal gas, and as such, the partial pressure and the fugacity of an ideal gas are equivalent. However, the fugacity coefficient deviates from one for a non-ideal gas. Calculations involving the fugacity of non-ideal gas mixtures can be tedious as it is time consuming to determine fugacities from experimental data, requiring volumetric measurements of the gas at several PTX conditions and the derivation of an equation of state that relates the volume of the gas as a function of PTX. A single measurement of the volume at one PTX condition is not sufficient to determine an equation of state. Lamadrid et al. (2017b) recently described a new method of determining the fugacity of N<sub>2</sub>, CH<sub>4</sub>, and CO<sub>2</sub> gases in mixtures utilizing Raman spectroscopy. This study extends this method to gas compositions of 25% N<sub>2</sub>, 25% CO<sub>2</sub>, and 50% CH<sub>4</sub> and 15% N<sub>2</sub>, 60% CO<sub>2</sub>, and 25% CH<sub>4</sub>, as well as the use of molecular dynamics modeling to better understand the molecular interactions responsible for the non-ideality of the mixtures.

Raman spectra were collected from 10-500 bars at 25°C for the aforementioned gas mixtures. The spectra were converted to Raman pressures using pure gas calibration data for CO<sub>2</sub>, CH<sub>4</sub>, and N<sub>2</sub> determined using results from Lamadrid et al. (2017a), Fall et al. (2011), and Lin et al. (2007), and this study. Pressures determined from the Raman spectra do not correspond to the partial pressures of the individual gases determined from equation 1 (see Figure 1), nor do the sum of these pressures equate to the total pressure. The pressure determined from the Raman spectra can be used to determine the fugacity of the components using the following relationship from Lamadrid et al. (2017b):

$$f_i = P_i \cdot \frac{f_v}{P_v} \quad [2]$$

where  $f_i$  is the fugacity of component  $i$ ,  $P_i$  is the partial pressure,  $f_v$  is the fugacity determined by the Redlich-Kwong equation of state for the pure gas component using the Raman pressure, and  $P_v$  is the Raman pressure. Fugacities

calculated from equation 2 are in good agreement with fugacities predicted using the Redlich-Kwong equation of state applied to the mixture (see Figure 2). Thus, utilizing Raman spectroscopy, the fugacity of CO<sub>2</sub>, CH<sub>4</sub>, and N<sub>2</sub> can be determined easily over a range of PTX conditions. The method may also be applied to determine fugacities of gases at elevated temperatures by conducting in situ Raman analyses using a high temperature and pressure cell. Finally, this method may be used to approximate the internal pressure of fluid inclusions containing CO<sub>2</sub>, CH<sub>4</sub>, and N<sub>2</sub> by calculating fugacities using both the Redlich-Kwong equation of state and equation 2 for a range of pressures and determining where the two fugacity values are equivalent for all three gases.

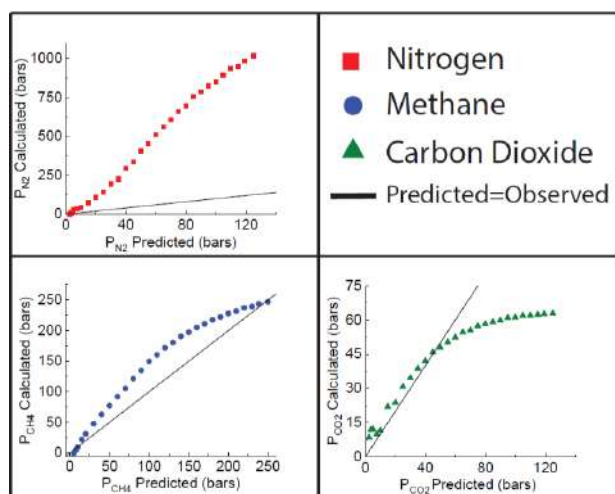


**Figure 1.** Comparison of the partial pressures of each component predicted using eq. 1 vs the Raman pressures of each component calculated using the Raman peak position for the 25% N<sub>2</sub>, 25% CO<sub>2</sub>, and 50% CH<sub>4</sub> mixture

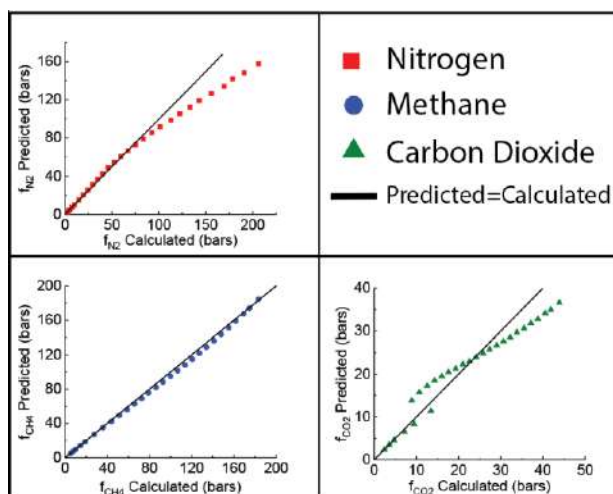


**Figure 2.** Comparison of the fugacities of each component calculated using equation 2 vs the fugacities predicted using the Redlich-Kwong EOS for the 25% N<sub>2</sub>, 25% CO<sub>2</sub>, and 50% CH<sub>4</sub> mixture

#### REFERENCES

- Fall, A. et al. (2011) Combined microthermometric and Raman spectroscopic technique to determine the salinity of H<sub>2</sub>O–CO<sub>2</sub>–NaCl fluid inclusions based on clathrate melting, *Geochim. Cosmochim. Acta* 75, 951-964.
- Lamadrid, H. M. et al. (2017a) Reassessment of the Raman CO<sub>2</sub> densimeter, *Chem. Geol.* 450, 210-222.
- Lamadrid, H. M. et al. (2017b) Relationship between Raman spectral features and fugacity in mixtures of gases, *J. of Raman Spectroc.* 49, 1-13.
- Lin, F. et al. (2007) Experimental determination of the Raman CH<sub>4</sub> symmetric stretching ( $\nu_1$ ) band position from 1–650 bar and 0.3–22 °C: Application to fluid inclusion studies, *Geochim. Cosmochim. Acta* 71, 3746-3756.

## Analysis of Water Content in Melts (Silicate Glass) Using Raman Spectroscopy

Heather M. VANDERGRIFT<sup>1</sup>, Robert J. BODNAR<sup>1</sup>, Maxim GAVRILENKO<sup>2</sup>, Michael KRAWCZYNSKI<sup>3</sup>

<sup>1</sup>Fluids Research Laboratory, Department of Geosciences, Virginia Tech, Blacksburg, Virginia, U.S.A.

<sup>2</sup>Department of Geological Sciences & Engineering, University of Nevada, Reno, Nevada, U.S.A.

<sup>3</sup>Department of Earth and Planetary Sciences, Washington University in St. Louis, St. Louis, Missouri, U.S.A.

E-mail: heathv7@vt.edu

Recent years have seen significant research advances and interest related to the concentration of volatiles in natural silicate melts. This interest has been driven by the knowledge that volatile contents of magmas play an important role in the style of volcanic eruptions. This information is being applied in studies of melt inclusions from historical eruptions to compare eruption explosivity with volatile contents of melts in order to develop predictive models for future eruptions.

Various techniques have been used to determine the volatile contents of melt inclusions, including differences from EMPA analysis, FTIR, SIMS, and Raman spectroscopy. Each of these techniques offers advantages and disadvantages. While EMPA difference results tell us that additional components (elements) not accounted for in the list of elements being detected are present, it is not possible to identify the missing components. FTIR provides highly precise data for H<sub>2</sub>O and CO<sub>2</sub> in silicate glasses, but requires fairly large melt inclusions that must be exposed on both the top and bottom of the thin section. SIMS provides reliable data for H<sub>2</sub>O, CO<sub>2</sub>, F, Cl and S, but is expensive to use and facilities are limited. Raman provides excellent spatial resolution and has been used to determine H<sub>2</sub>O contents of glass, but has relatively poor detection limits compared to FTIR and SIMS.

Here we describe the results of Raman analysis of the H<sub>2</sub>O contents of experimentally produced silicate glasses. The H<sub>2</sub>O contents had been determined previously by EMPA difference. Each sample was gently polished with a 0.3-micron alumina grit before being analyzed by Raman spectroscopy to remove the carbon coating from EMPA. Analyses were done using a 541 nm laser, a 600 grooves/mm diffraction grating, 400 micron hole, 150 micron slit, and 3 collections of 300 s each using the 100x objective and with the spectrometer centered at 3325 cm<sup>-1</sup>. To calibrate the measurements and test for reproducibility, three standard glass samples containing 4.61, 5.86 and 8.08 wt% H<sub>2</sub>O were analyzed (Fig. 1). Two separate spots were analyzed on each standard focused to a depth 0.3 microns below the surface. The area under the H<sub>2</sub>O band in the Raman spectrum was determined using an 8<sup>th</sup> order polynomial base-line correction and Gaussian peak fitting. The average area determined for the two measured spots was calculated and used to determine the H<sub>2</sub>O content of the unknown following the method described by Thomas (2000). Accordingly, the ratio of the peak areas of the standard (Fig. 2) and unknown is proportional to the ratio of the H<sub>2</sub>O content of the standard and the unknown.

The preliminary results show that the H<sub>2</sub>O content estimated using the method described by Thomas (2000) is consistent with H<sub>2</sub>O contents determined by EMPA difference. For example, the H<sub>2</sub>O content of unknown F087 3.3 wt.% from EMPA difference, and the Raman value is 3.1 wt%. The H<sub>2</sub>O content of unknown F104 is 10.1 wt% and the Raman-determined value is 9.2 wt%. In general, the difference between the EMPA value and Raman value is less than 10%.

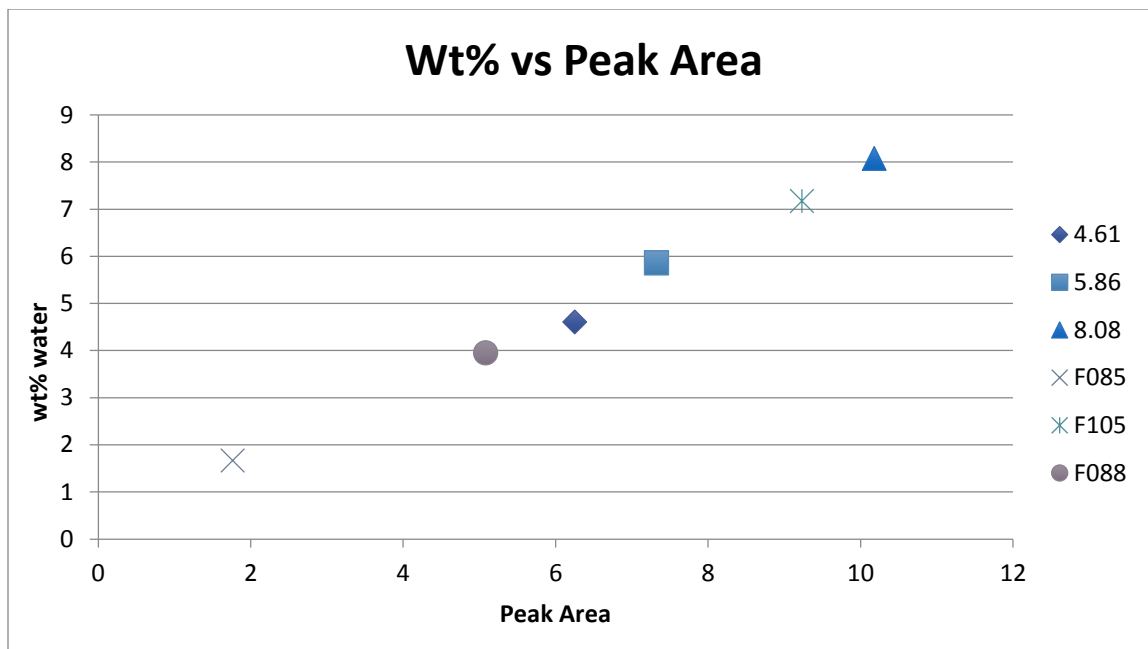


**Figure 1.** Relationship between peak area (standards included) and weight percent water based on Raman analysis.

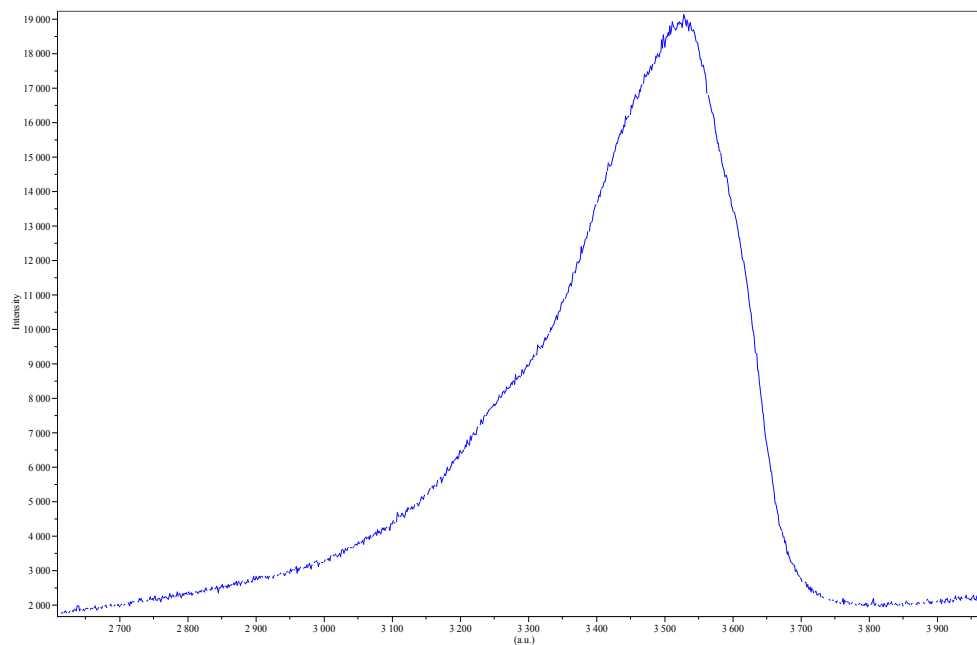


**Figure 2.** Spectrum of standard glass containing 4.61 wt% water.

REFERENCES

Thomas, R. (2000) Determination of water contents of granite melt inclusions by confocal laser Raman microprobe spectroscopy, *American Mineralogist* 85, 868-872.

## Keynote – Fluid inclusions in ice

Edwin D. WADDINGTON

*Earth and Space Sciences, University of Washington, Seattle, Washington, U.S.A.*

*E-mail: edw@uw.edu*

Polar ice sheets in Greenland and Antarctica, mountain glaciers, and sea ice on the Arctic and Southern Ocean are major reservoirs of ice on Earth. All three ice reservoirs contain fluid inclusions, but their contents, formation processes, and geophysical importance differ markedly. In the interiors of the Greenland and Antarctic ice sheets, the inclusions contain air and water vapor. In mountain glaciers, which are often at their pressure-melting temperature, the inclusions can be 1% of the volume, and can contain air, water, water vapor, or all three. In sea ice, the fluid in the inclusions is usually brine and vapor. In comparison with other rocks, ice bodies are chemically simple systems in which solid, liquid, and vapor are predominantly one chemical species, H<sub>2</sub>O. However, this simplicity can be illusory, because even at -55°C at South Pole, ice is still at 85% of its melting temperature, and this relative warmth means that the vapor phase continually affects inclusions through sublimation and deposition.

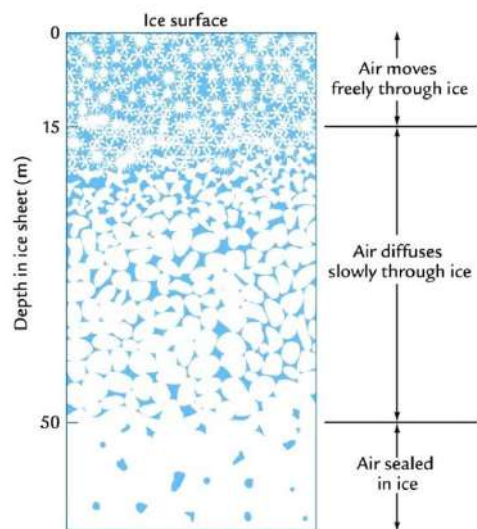


**Figure 1.** Left – Firn consolidation and occlusion of air bubbles. Air in bubbles is always younger than the ice that traps it. The difference is called  $\Delta$ age. Right – Bubbly ice recovered in a shallow ice core. Credit: Lonnie Thompson, The Ohio State University.

Ice cores from the polar ice sheets have provided climate histories going back 800,000 years (EPICA, 2004), and a search is underway now for million-year-old ice in East Antarctica. The temperature history at a site can be found from stable isotopes ( $\delta$ D or  $\delta^{18}$ O of H<sub>2</sub>O) in the ice, and air trapped in bubbles provides the only surviving samples of Earth's atmosphere in the past. Firn is the intermediate stage between snow and glacier ice, as accumulating snow compacts under its own weight. However, the process can take centuries to millennia, during which air in the firn can still mix with the free atmosphere, so correlating paleotemperatures to greenhouse gases such as CO<sub>2</sub> and CH<sub>4</sub> requires accurate calculation of the age difference between the air and the ice that holds it. That difference ( $\Delta$ age) is estimated with firn-compaction models. Most models since Herron and Langway (1980) are based on the Robin (1958) hypothesis - each decrease in porosity is proportional to the increase in overburden stress. This is an inherently steady-state assumption, and most models are empirically tuned using measured depth-density profiles, mean-annual temperatures, and accumulation rates, all of which are assumed to be steady.

Recent efforts, e.g. Arthern et al. (2010), use more physics in the firn-consolidation equations, following concepts developed in hot-powder pressing of ceramics and metals. The effective viscosity or strength of firn depends on the evolving microstructural properties of the ice-air aggregate, such as specific surface area, and distributions of grain size, neck area, and coordination number. Evolution equations for microstructural properties as functions of overburden stress, temperature, and the current microstructural state can now be tested with  $\mu$ -CT

scans of firn cores (e.g. Figure 2) that track those properties with increasing age under a range of climate conditions. When an effective viscosity can be computed at each stage, a transient continuum compaction equation can be solved for firn density. New estimates of  $\Delta$ age in ice cores refined in this way should contribute to improved interpretations of paleoclimate states. Evolution of intrinsic permeability can also be inferred.

Isotopic analysis of air in bubbles, (Sowers et al., 1992), also informs us about past climate and about  $\Delta$ age. Firn is a huge diffusion column, and heavy isotopes such as  $^{40}\text{Ar}$ , and  $^{15}\text{N}$  in  $\text{N}_2$  gravitationally settle and concentrate at the bottom, where bubbles are trapped. In a steady climate, deviations from atmospheric values indicate the depth of the diffusive column, and that depth in turn contains information about temperature and snow accumulation rate at the time. When climate changes abruptly, heavy isotopes move toward colder depths, enhancing or counter-acting the gravitational settling. The effects can be separated because  $^{40}\text{Ar}$  diffuses more slowly than  $^{15}\text{N}$ . Since the atmosphere is globally well-mixed, correlating trace-gas concentrations also allows new ice cores to be dated (WAIS, 2015).

Sea ice forms from freezing seawater in the polar oceans. With seawater at  $-2^\circ\text{C}$ , and the air at  $-32^\circ\text{C}$  above e.g. a 10 cm layer of growing ice, temperature gradients can exceed  $300^\circ\text{C m}^{-1}$ . During the freezing process, salt is excluded from the ice lattice, causing a salinity gradient under the thickening ice. Because heat diffuses in the water faster than salt, a layer of super-cooled water  $\sim 10$  cm thick forms under the ice, which grows by sending fingers or platelets into the super-cooled water, rather than by advancing as a planar front (as lake ice would). The fingers trap seawater in pockets in the growing ice, forming brine inclusions. The freezing point of a brine inclusion must match the temperature of the surrounding ice. When the ice cools, the brine is too dilute, and water freezes onto the walls of the inclusions, raising the salinity and shrinking the inclusions. When the ice warms, so ice melts off the walls, diluting the brine and enlarging the inclusions. Enlarged brine pockets can join up, forming vertical brine channels, which ultimately drain the brine back into the ocean below. The vertical channels make the sea ice mechanically anisotropic and weak for horizontal shear, which is important for ship operations and pack-ice forecasts. Cores reveal texture and strength, and can sample microbial activity in the brine channels.

#### REFERENCES

- Arthern, R. J., D.G. Vaughan, A.M. Rankin, R. Mulvaney, E.R. Thomas (2010). In situ measurements of Antarctic snow compaction compared with predictions of models. *JGR*. 115, F03011. <https://doi.org/10.1029/2009JF001306>.
- WAIS-Divide Project Members. (2015) Precise interhemispheric phasing of abrupt climate change during the last ice age. *Nature*, 520, 661-665.
- Dadic, R., P.C. Mullen, M. Schneebeli, R.E. Brandt, and S.G. Warren (2013) Effects of bubbles, cracks, and volcanic tephra on the spectral albedo of bare ice near the Transantarctic Mountains: Implications for sea glaciers on Snowball Earth. *JGR Earth Surface* 118(3). doi:10.1002/jgrf.20098.
- EPICA Community Members, (2004) Eight glacial cycles from an Antarctic ice core. *Nature* 429: 623-628.
- Herron, M. and C.C. Langway (1980) Firn densification: an empirical model. *J. Glaciol.* 25(93), 373-385.
- Lundin, J.M.D., and 13 others. (2017) Firn Model Inter-Comparison Experiment (FirnMICE). *J. Glaciol.* 63, 401-422.
- Robin, G. de Q. (1958). *Glaciology III: Seismic shooting and related investigations, Norwegian-British-Swedish Antarctic Expedition, 1949-52*. Scientific Results 5, 134. Oslo: Norsk Polarinstitut.
- Sowers, T., M. Bender, D. Raynaud, and Y.S. Korotkevich (1992)  $\delta^{15}\text{N}$  of  $\text{N}_2$  in air trapped in polar ice: a tracer of gas transport in the firn and a possible constraint on ice age–gas age differences. *JGR* 97, 15683–15697.

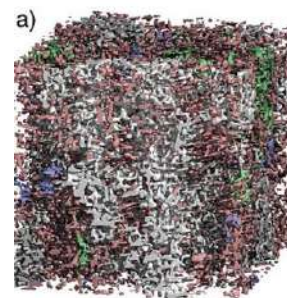


**Figure 2.**  $\mu$ -CT image of firn near close-off density. From Dadic et al. (2015).

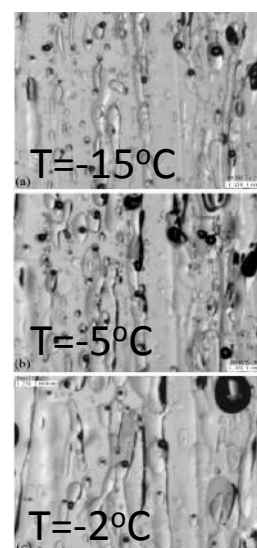


**Figure 3.** Brine pockets and channels enlarge as temperature increases.

## Unraveling the history of ultra-deep fractures in sedimentary basins

Qiqi WANG, Stephen E. LAUBACH, András FALL

*Bureau of Economic Geology, Jackson School of Geosciences, The University of Texas at Austin, Austin, Texas, U.S.A.*

*E-mail: wangqiqi@utexas.edu*

In the past half-decade unprecedented opportunities have arisen for extracting information about the origin and persistence of fracture porosity from fracture samples. Even in largely open fractures, localized cement deposits and fluid inclusion assemblages accumulated during fracture growth provide unique records of fluid composition and temperature. With burial history or cement accumulation models these records can yield evidence of the timing and rate of fracture formation.

Here we unravel the history of fracture in the ultra-deep Lower Cretaceous Frontier Formation sandstones using core samples from two wells in the Madden field, Wyoming (Figure 1). The Madden structure is an east-west trending anticline discovered in the 1960s (Brown and Shannon, 1989). The Big Horn 2-3 was an early deep delineation well. In 1992, shortly after retrieving the core we describe, the Big Horn 3-36 well blew out and caught fire; subsequently gas was produced at a rate of about 5 MMcfd, testifying to the efficacy of open fractures as fluid conduits in these low porosity sandstones.

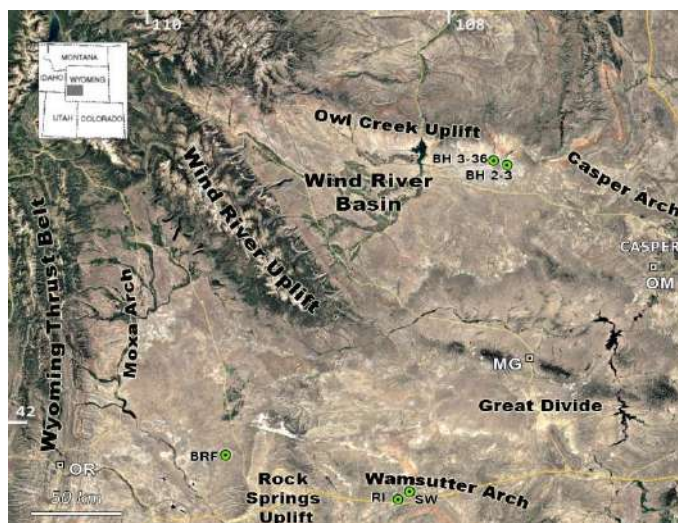


**Figure 1.** Location of deep ‘Bighorn’ BH 3-36 and 2-3 cores in Wyoming. RI, SW and BRF are other core locations (shallower depths) and OR, MG, and OM are outcrop locations of fractured Frontier Formation being compared with subsurface data.

called a ‘gap deposit’ to distinguish them from the overall fracture of which they form a part, is typically marked by a fluid inclusion assemblage trapped along the gap deposit centerline (Figure 2).

Gap deposit thicknesses normal to fracture walls in more shallowly buried sandstones typically range from less than 1  $\mu\text{m}$  to more than 1 mm, but commonly are less than 20  $\mu\text{m}$  (avg. ca. 10  $\mu\text{m}$ ) (Laubach et al., 2004). But gap sizes in our deep samples are wider, with many in the range of 40  $\mu\text{m}$ . Cross-cutting relations documented by mapping cement textures, allows the relative time sequence of fluid inclusion assemblages to be documented. Quartz deposits that span between fracture walls are separated by porous fractures having thin quartz lining (rinds) or these areas or residual void space may be filled with calcite.

Preliminary fluid inclusion results show that FIAs record a wide range of temperatures from about 140°C to 260°C or more, and have a fairly narrow salinity range that is mostly less than 2 wt% NaCl. The high temperature of fracture formation likely accounts for the wide sizes of quartz gap deposits, since temperature is a main control on spanning potential (Lander and Laubach, 2015). Assuming measured temperatures reflect burial depths, for typical Rocky Mountain region burial histories for the Frontier Formation (i.e. Laubach et al., 2016), our FIA results imply that fractures grew over tens of millions of years. Although further analysis is needed, both wells may contain a

Our samples are from depths of 6240 to 6244 m. Frontier sandstones are dominantly litharenites to sublitharenites, with average composition of 64% quartz, 6% feldspar, and 30% lithics, although more quartz-rich facies are locally present. Opening-mode fractures are aligned at a high angle to beds and thus have steep dips. Fractures are lined and locally bridged with quartz deposits (Figure 2). Overall apertures of the fractures we mapped are 400-700  $\mu\text{m}$ . As in other moderately-deeply buried sedimentary rocks, isolated bridges of cement deposited during fracture opening in otherwise open fractures have rod or pillar-like shapes that are typically oriented normal to, and connect opposite, opening-mode walls.

Bridges contain wall-rock fragments and cement arranged in crack-seal texture that records repeated cracking and local cement accumulation along fractures within the bridges as well as zoned, non-crack seal quartz. Each crack-seal increment,

temperature gap (ca. 170-210°C) that could mark a hiatus in fracture growth. A hiatus in fracture widening was documented in fractures from the Frontier Formation in the Green River Basin from depths of 4538 to 4547 m (Laubach et al., 2016).

Fracture mineralogy and textures were documented using transmitted light petrography and cathodoluminescence (CL) imaging obtained with a Zeiss Sigma High Vacuum Field Emission SEM with an Oxford X-Max 50 Silicon drift detector (SDD) and a Gatan MonoCL4 system specifically configured for large-area mosaic SE, BSE, EDS, and CL imaging. The SEM was operated at 12–15 kV and at large sample currents for panchromatic and color CL imaging. For microthermometry we used a USGS-style gas flow heating/freezing stage mounted on an Olympus microscope equipped with a 40× objective (N.A.=0.55) and 15× oculars.

In agreement with previous results from other sandstones (e.g., Fall et al., 2015) our results show that fractures in sandstones can grow over long time periods and retain porosity at great depth (>6 km) and high temperature (>170°C) for tens of millions of years.

#### ACKNOWLEDGEMENTS

Research supported by grant DE-FG02-03ER15430 from Chemical Sciences, Geosciences and Biosciences Division, Office of Basic Energy Sciences, Office of Science, U.S. Department of Energy, and by the Fracture Research and Application Consortium.

#### REFERENCES

- Brown, R.G., Shannon, L.T. (1989) The #2-3 Bighorn: an ultra-deep confirmation well on the Madden anticline. Gas Resources of Wyoming. 40<sup>th</sup> Annual Field Conf., Wyo. Geol. Assoc. Guidebook, 181-187.
- Fall, A., Eichhubl, P., Bodnar, R. J., Laubach, S.E., Davis, J.S. (2015) Natural hydraulic fracturing of tight-gas sandstone reservoirs, Piceance Basin, Colorado. *Geol. Soc. Am. Bull.* 127(1-2), 61-75.
- Lander R.H., Laubach, S.E. (2015) Insights into rates of fracture growth and sealing from a model for quartz cementation in fractured sandstones. *Geol. Soc. Amer. Bull.* 127(3-4), 516-538.
- Laubach, S.E., Fall, A., Copley, L.K., Marrett, R., Wilkins, S. (2016) Fracture porosity creation and persistence in a basement-involved Laramide fold, Upper Cretaceous Frontier Formation, Green River Basin, U.S.A. *Geol. Mag.* 153 (5/6), 887-910.
- Laubach, S., Lander, R., Bonnell, L., Olson, J., Reed, R. (2004) Opening histories of fractures in sandstone. In Cosgrove, J.W., Engelder, T., eds., *The initiation, propagation, and arrest of joints and other fractures*, *Geol. Soc. London Sp. Pub.* 231, 1-9.

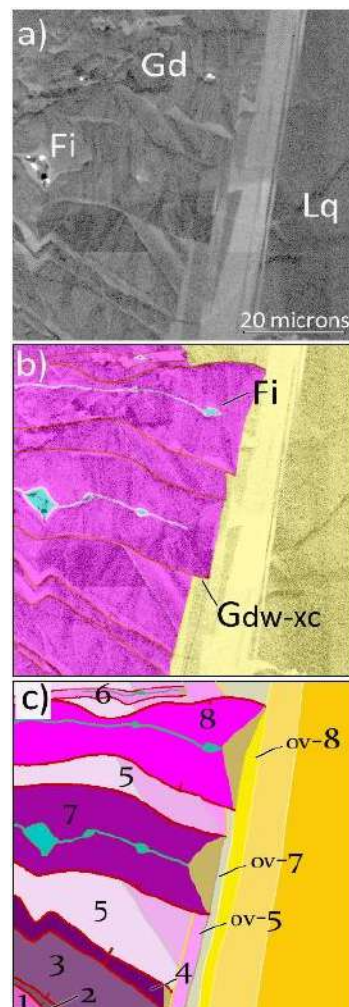


**Figure 2.** SEM-CL (a), (b) and map (c) of edge of bridge deposits showing crack-seal texture. Gd; Gdw-cx gap deposits and crosscutting relations. Lq, non-crack seal quartz. FIA locations marked by blue color in(c). Numbers indicate sequence of gaps and overgrowths.

## Keynote – Reassessing Cl in melt inclusions: new insights on magma and magmatic fluid geochemistry based on Cl solubility in silicate melts

Jim WEBSTER

Department of Earth & Planetary Sciences, American Museum of Natural History, New York, New York, U.S.A.

E-mail: [jdw@amnh.org](mailto:jdw@amnh.org)

Identifying pulses of fluid-saturated magma, both intrusive and eruptive, is essential for understanding a host of magmatic-hydrothermal processes (Wallace et al., 1995). Accurate interpretation of buoyancy-driven fluid ascent and fluid accumulation at apices of plutons; component exchange between hydrothermal fluid, melt, and minerals; the deposition of granite-related magmatic-hydrothermal mineralization; and/or the explosive fragmentation and eruption of volatile-enriched melts requires unambiguous recognition of the presence of exsolved magmatic fluids. Research on magmatic Cl has proven useful for understanding degassing, melt evolution, and other igneous processes. Magmatic Cl behavior varies strongly with its solubility in melt, and Cl solubility and its partitioning between melts and fluids vary with the Cl content of the system, melt composition, pressure, and the abundance of oxidized magmatic sulfur; temperature has a lesser influence. Given these solubility relationships and that they differ from those with the other primary, COHS magmatic volatiles, Cl can provide unique insights on magma evolution and fluid exsolution when understood in the context of its solubility in melts.

Some publications on magmatic Cl include ambiguous references to “high” versus “low” Cl in melt inclusions and the magmas they represent. Equivocal characterizations like these hinder the interpretation of volatile behavior during magma evolution because they describe relative rather than absolute concentrations. This is particularly problematic for Cl because its solubility in melt and its partitioning between melts, minerals, and fluids vary so strongly with melt composition and magmatic Cl contents. Consequently, a few studies have applied

experimentally determined Cl solubility limits to Cl contents of melt inclusions (Webster et al., 2015) and in matrix glasses (Balcone-Boissard et al., 2016) to track hydrosaline liquid or brine exsolution in felsic magmas. Most other studies, however, do not account for the fundamental control of melt composition on Cl dissolution in silicate melts and coexisting fluids. Chlorine solubility is determined experimentally with silicate melts that are saturated in brine ± vapor, and modeled Cl solubilities represent maximum values that are fixed in the melt due to thermodynamic equilibrium with a hydrosaline liquid or brine (with or without a coexisting aqueous or aqueous-carbonic vapor phase) at a fixed pressure, temperature, and melt composition.

This study presents a new method of interpreting melt Cl concentrations that are normalized to their Cl solubilities. We apply the method to the Cl concentrations of > 5000 mafic to felsic melt inclusions (MI) and matrix glasses (MG) (Figure 1), but we focus on Cl in approximately 3800 dacitic to rhyolitic MI and MG (Figure 2) representing 68 felsic igneous systems to elucidate the behavior of Cl during magmatic, magmatic-hydrothermal, degassing, and mineralizing processes. Most of these glasses are metaluminous and rhyolitic, but the compositions range from sub-alkaline dacites to alkaline trachytes and pantellerites and comendites and also include alkali-poor to alkali-enriched rhyolites. Tectonically, most glasses come from eruptive systems including volatile-enriched

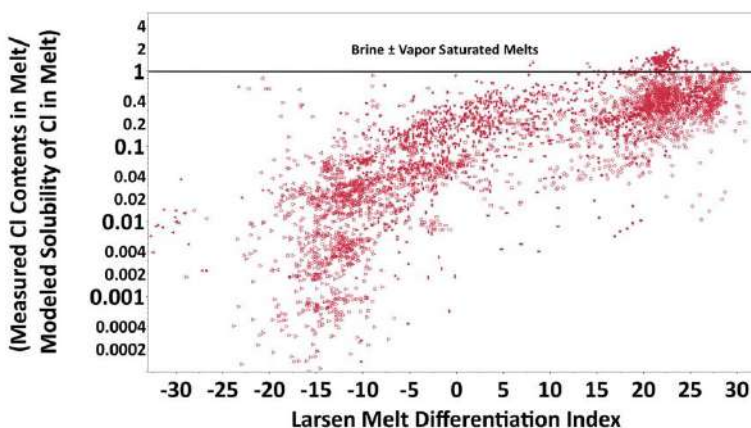


**Figure 1.** Measured Cl concentrations normalized to Cl solubilities (calculated for 50 MPa) for > 5000 basaltic to rhyolitic melt inclusions and matrix glasses as a function of melt evolution expressed as the Larsen index =  $[(\text{SiO}_2/3)+(\text{K}_2\text{O}) - (\text{CaO})-(\text{Mg})-(\text{FeO}) \text{ wt.\% basis}]$ .

subduction-related magmas, back-arc basins, and continental rhyolitic systems. Other MI represent hot-spot related oceanic granites; rift-related granites; tin-mineralized porphyritic granites; and other Cu-, W-, Mo-, Ag-, base metal-,  $\pm$  Nb-mineralized porphyritic granites.

The influence of decreasing pressure, associated with magma ascent-driven decompression, on Cl solubility in brine-  $\pm$  vapor-saturated melts is interpreted for these 68 felsic magmas. The modeled Cl solubilities in melt decrease and, hence, the solubility-normalized Cl ratios (i.e., measured Cl contents/modelled Cl solubilities) increase, with reduced pressure. Comparison (Figure 2) of the solubility-normalized Cl ratios of the MI and MG with the horizontal line that represents solubility-normalized Cl ratios of unity identifies the pressure at which the felsic melt was saturated in brine  $\pm$  vapor. For example, glasses from 2 systems overlap with and 4 others lie above the line indicating saturation in brine at mid-crustal pressures equal to or greater than 600 MPa, respectively. Moreover, Cl in glasses from 10 additional systems are consistent with saturation in brine at near-surface pressures of 20 MPa.

One can also model the effects of fractional crystallization, magma mixing, degassing, and/or brine assimilation on Cl behavior at fluid-absent or fluid-saturated conditions and compare the modeled results with MI and MG from each magmatic system (Figure 2). The solubility-normalized Cl concentrations of felsic MI and MG show a variety of trends as well as fluctuating ranges in dispersion or scatter in the data when plotted relative to the

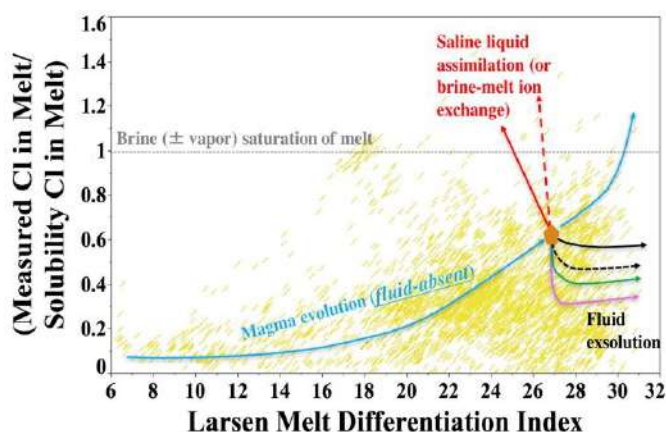


**Figure 2.** Measured Cl concentrations normalized to modeled Cl solubilities (calculated for > 3800 felsic melt inclusions and matrix glasses at 200 MPa) as a function of the Larsen differentiation index applied to processes of magma evolution and fluid exsolution.

vapor, brine or integrated vapor plus brine) range from 0.3 to nearly 70 wt.%. This very wide range in Cl contents decreases significantly with increasing fluid mass (i.e., with increasing crystallization and melt evolution). For instance, the fluid(s) contain 0.3 to  $\leq$  18 wt.% Cl with 2 grams of fluid, and the modeled fluids contain only 0.3 to 11 wt.% Cl when the mass of fluid increases to 4 grams (for a fluid/melt ratio of  $4 \times 10^{-2}$ ).

This approach offers great promise for modeling fluid exsolution and estimating Cl concentrations of magmatic fluids and coexisting melts during Cl exchange processes, but significantly more experimental data on Cl solubilities in melts and on Cl partitioning between melts and fluids are required for mid- to shallow-crustal pressure conditions, in addition to these extant constraints for 200 MPa. Also, the dramatic influence of oxidized magmatic sulfur on Cl partitioning must be better determined.

#### REFERENCES

- Wallace, P. (2005) Volatiles in subduction zone magmas: concentrations and fluxes based on melt inclusion data, *Journal of Volcanology and Geothermal Research* 140, 217-240.
- Webster, J.D. et al. (2015) Experimental and modeled chlorine solubilities in aluminosilicate melts at 1 to 7000 bars, *American Mineralogist* 100, 522-535.
- Balcone-Boissard, H. et al. (2016) Chlorine as a geobarometer for alkaline magmas: evidence from a systematic study of the eruptions of Mount Somma-Vesuvius, *Nature* DOI:10.1038/srep21726.

## Keynote – The fate of sulfur at the magmatic-hydrothermal transition in the porphyry ore-forming environment

Zoltán ZAJACZ, Alexandra TSAY, Nuur GHAZALI

Department of Earth Sciences, University of Toronto, Toronto, Ontario, Canada

E-mail: zajacz@es.utoronto.ca

Porphyry-type Cu ( $\pm$ Au, Mo) ore deposits are even larger positive anomalies for sulfur in the Earth's crust than they are for Cu. Their ore metal and sulfur budget is thought to be derived from aqueous fluids released from associated large upper crustal magma reservoirs. Sulfur plays multiple roles in the genesis of these deposits: 1) it acts as a ligand to form complexes with certain ore metals in high temperature fluids; 2) it facilitates the precipitation of sulfide ore minerals and 3) it is a key to the acid rock alteration typically occurring at higher levels in porphyry systems (i.e. sericitic and advanced argillic alteration zones). Porphyry deposits most commonly occur in association with relatively oxidized, hydrous magmas and much of the S is thought to enter the hydrothermal system as magmatic SO<sub>2</sub> (e.g. Sillitoe 2010 and references therein). The SO<sub>2</sub> disproportionates to H<sub>2</sub>S and H<sub>2</sub>SO<sub>4</sub> at lower temperature. The such-formed H<sub>2</sub>S may react with dissolved metal chloride complexes to form ore metal sulfides, whereas the H<sub>2</sub>SO<sub>4</sub> will cause acid alteration and the precipitation of hydrothermal sulfates (e.g. anhydrite and alunite). Most of the S is stored in the form of anhydrite in porphyry ore deposits and much of the anhydrite occurs in the higher-temperature potassic alteration zone (e.g. Gustafson and Hunt, 1975), which lacks acid alteration suggesting that the origin of anhydrite here cannot be explained by the disproportionation of magmatic SO<sub>2</sub>. As most of the ore metal endowment of porphyry deposits is concentrated in the potassic alteration zone, it is critical to understand the mechanism of anhydrite and sulfide precipitation in this zone because it may help us answer key open questions in porphyry ore genesis, such as the significance of S and metal donation from mafic magmas and the relative significance of vapor and brine phases in ore mineral precipitation.

Recent studies have proposed various new mechanisms to explain the formation of anhydrite in porphyry deposits, including direct H<sub>2</sub>SO<sub>4</sub> transfer from the magma to the hydrothermal system and chemisorption of magmatic SO<sub>2</sub> by Ca-rich minerals in the host rock (Binder and Keppler, 2011; Henley et al., 2015; Mavrogenes and Blundy, 2017). However, both of these would still induce strong acid alteration of the host rock and thus are at odds with the presence of anhydrite in the potassic alteration zone. Similarly, the proposition of Blundy et al. (2015) of deep mafic-magma sourced SO<sub>2</sub> interacting with metal-rich brines accumulated at shallower levels to produce ore metal sulfides involves the production of abundant HCl and thus would result in acid alteration.

We hypothesized that anhydrite component can directly dissolve into high-temperature brines and may precipitate later on simply due to cooling without involving reaction with the host rock. To test this hypothesis, we conducted experiments to 1) assess the solubility anhydrite in magmatic fluids as a function of fluid salinity, temperature and pressure; and 2) test if oxidizing conditions may allow the partitioning of sulfur into the brine phase during vapor-brine separation. For these purposes, experiments were conducted in rapid-quench Molybdenum-Hafnium Carbide pressure vessel assemblies in the *P-T* range of 120 – 240 MPa and 600 – 900 °C. The fluid phase(s) were trapped in the form of synthetic fluid inclusions (SFI) at run *P-T* in quartz fractured *in situ* during the experiment after the attainment of equilibrium. Most anhydrite solubility experiments were conducted at *P*=240 MPa confining pressure to allow free variation of fluid salinity without intersecting the vapor-brine immiscibility field. Experiments aiming to determine the brine/vapor partition coefficients of S ( $D_S^{b/v}$ ) were mostly conducted at *P*=130 MPa and *T*=900 °C and followed the methodology developed by Zajacz et al. (2017). Vapor and brine salinities are around 4 and 60 wt% NaCl equivalent at these conditions, respectively. Particular attention was paid to testing the effect of *f*O<sub>2</sub> and thus the oxidation state of S on  $D_S^{b/v}$ . The concentration of S and other major and trace elements in the SFI were determined by Laser Ablation Inductively Coupled Plasma Mass Spectrometry (LA-ICP-MS) at the University of Toronto. The analytical procedure optimized for quantitative sulfur analysis involved the use of an in house-built low-S background ablation cell and the measurement of <sup>34</sup>S.

The results show that the solubility of anhydrite exponentially increases with fluid salinity (Fig. 1) and reaches very high values in high salinity supercritical fluids and also in sub-critical brines with similar salt concentration. At the same time, the solubility of anhydrite in brines is highly temperature dependent and drops by

about a factor of 5 as  $T$  decreases from 900 °C to 600 °C. On the other hand, the brine/vapor partitioning experiments showed that while  $S$  does show a strong preference for the vapor phase at reducing conditions where  $S$  is dominantly in 2- oxidation state, this behavior drastically changes with increasing  $fO_2$ . The value of  $D_S^{b/v}$  increased from about 0.2 to 0.9 with  $fO_2$  increasing from one log unit below to 1.8 log unit above the Ni-NiO buffer. Note that the  $fO_2$  of most porphyry Cu systems is around or above the latter value. The addition of significant HCl to the bulk fluid (HCl/total Cl = 0.25) did not cause a statistically significant change in  $D_S^{b/v}$  at either oxidizing or reducing conditions.

Keeping in mind that many magmas associated with porphyry ore deposits are anhydrite saturated, our results suggest that primary magmatic brines could carry a significant amount of dissolved anhydrite component, which would rapidly precipitate upon cooling, explaining the presence of anhydrite in the potassic alteration zone. Even if the input magmatic fluids are in the single phase field and have low to moderate salinities as observed in some porphyry systems, still a significant amount of  $S$  would partition into the brine phase upon the commonly seen brine condensation during the decompression of ascending magmatic fluids. Subsequent cooling of these brines would also facilitate anhydrite precipitation without causing acid alteration. One may question if most of the  $S$  is present as sulfate species in these high- $T$  brines, how do ore metal sulfides precipitate from them? The most likely explanation is electron exchange between Fe and S in the fluid phase. Primary magmatic fluids contain high concentrations of iron in the form of dissolved Fe(II)Cl<sub>2</sub>. Upon cooling, Fe could donate electrons to S, yielding Fe<sup>3+</sup> and S<sup>2-</sup>. Commonly occurring potassic alteration zone minerals such as magnetite, biotite and even K-feldspar can serve as an Fe<sup>3+</sup> sink, while the production of S<sup>2-</sup> facilitates the precipitation of chalcopyrite and bornite. The reactions involved in sulfide precipitation produce much smaller amount of acid species than alternative mechanisms.

#### REFERENCES

- Binder, B. and Keppler, H. (2011) The oxidation state of sulfur in magmatic fluids. *Earth Planet. Sci. Lett.* 301, 190-198.
- Gustafson, L.B. and Hunt, J.P. (1975) The porphyry copper deposit at El Salvador, Chile. *Econ. Geol.* 70, 857-912.
- Sillitoe, R.H. (2010) Porphyry Copper Systems. *Econ. Geol.* 105, 3-41.
- Zajacz, Z. et al. (2017) The partitioning of Cu, Au and Mo between liquid and vapor at magmatic temperatures and its implications for the genesis of magmatic-hydrothermal ore deposits. *Geochim. Cosmochim. Acta* 207, 81-101.
- Henley R.W. et al. (2015) Porphyry copper deposit formation by sub-volcanic sulfur dioxide flux and chemisorption. *Nature Geoscience*, 8, 210-215.
- Mavrogenes J. and Blundy J. (2017) Crustal sequestration of magmatic sulfur dioxide. *Geology*, 45, 211-214.
- Blundy J. et al. (2015) Generation of porphyry copper deposits by gas-brine reaction in volcanic arcs. *Nature Geoscience*, 8, 235-240.

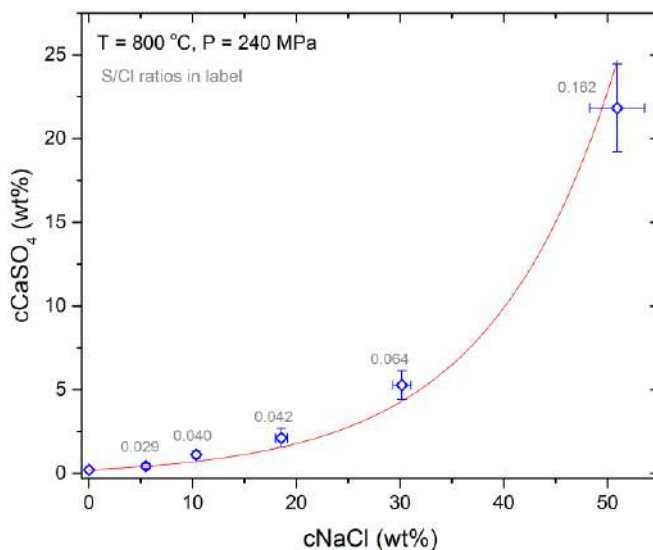


**Figure 1.** The solubility of anhydrite as a function of fluid salinity at  $T=800$  °C and  $P=240$  MPa. Uncertainties are reported at  $1\sigma$ ; S/Cl molar ratios in the fluid are shown in label.

## **Application of fluid inclusions to study shale hydrocarbon – a case study of Shaxin Well #2 on the southwestern margin of the Paleogene Qaidam Basin, northwest China**

Min ZHANG, Guangxi OU

*Beijing Research Institute of Uranium Geology, Beijing 100029, China*

*E-mail: zhangmin715@126.com*

Using inclusion petrography, the fluorescence characteristics of inclusions, and a microscopic temperature analysis, we combined the characteristics of tectonic activity and the evolution of hydrocarbon source rocks to comprehensively study the accumulation periods of Paleogene shale hydrocarbon reservoirs in Shaxin Well #2 on the southwestern margin of the Qaidam Basin. Due to the special property of general diagenesis of fine minerals in shale, for this study, we selected the interlayer of siltstone and fine sandstone in shale hydrocarbon reservoirs as the subject of analysis. The comprehensive studies indicate that this shale oil-gas reservoir experienced two periods of oil-gas filling processes: the first period occurred in late Miocene (N1) sedimentation, when the organic matter for the hydrocarbon source rocks were in the middle of its low-maturity stage; there is a lack of a vertical grooming system, and the accumulation scale is small. The second period occurred in late Pliocene (N2) sedimentation and continues today; this period was accompanied by massive tectonic movement during the late Himalayan period. The type of mature hydrocarbons in the deep hydrocarbon source rocks migrated along the fault network to the sandstone reservoirs, accumulated, and became reservoirs. The scale of hydrocarbons was relatively large during this period and is also the most important hydrocarbon accumulation process in the area.

### REFERENCES

- Bodnar, R.J. (1990) Petroleum migration in the Miocene Monterey Formation, California, USA: constraints from fluid-inclusion studies. *Mineral. Mag.* 54: 295-304.
- McLimans, R.K. (1987) The application of fluid inclusions to migration of oil and diagenesis in petroleum reservoirs. *App. Geochem.* 2: 585-603
- Ou, G.X., Li L.Q., Sun, Y.M. (2006) Theory and application of the fluid inclusion research on the sedimentary basins. *Bull. Min. Petrol. Geochem.* 25, 1-11.
- Tao, S.Z. (2006) Sequence of diagenetic authigenic mineral: the basis of timing the inclusions formation in sedimentary rock. *Petrol. Explor. Dev.* 33, 154-160.
- Yin, C.M., Zhang, B.Q. (2005) Petroleum resource status and development strategy in Qaidam Basin. *Eng. Sci.* 7, 78-82.



## Keynote – Fluid inclusions in Astromaterials: Direct samples of early solar system aqueous fluids

Michael ZOLENSKY<sup>1</sup>, Queenie H.-S. CHAN<sup>2</sup>, Yoko KEBUKAWA<sup>3</sup>, Robert J. BODNAR<sup>4</sup>, Marc FRIES<sup>1</sup>

<sup>1</sup>Astromaterials Research and Exploration Science, NASA Johnson Space Center, Houston, Texas, U.S.A.

<sup>2</sup>School of Physical Sciences, Open University, Milton Keynes, U.K.

<sup>3</sup>Division of Materials Science and Chemical Engineering, Yokohama National University, Yokohama, Japan

<sup>4</sup>Fluids Research Lab, Department of Geosciences, Virginia Tech, Blacksburg, Virginia, U.S.A.

E-mail: michael.e.zolensky@nasa.gov

**Introduction** We have become increasingly aware of the fundamental importance of water, and aqueous alteration, on primitive solar-system bodies (Zolensky et al., 2008). All classes of astromaterials studied show some degree of interaction with aqueous fluids. We have direct observations of cryovolcanism of several small solar system bodies (e.g. Saturnian and Jovian moons) (Lellouch et al., 2002), and indirect evidence for this process on the moons Europa, Titan, Ganymede, and Miranda, and the Kuiper Belt object Charon (Cook et al., 2007), and so are certain of the continuing and widespread importance of aqueous processes across the solar system. Nevertheless, we are still lacking fundamental information such as the location and timing of the aqueous alteration and the detailed nature of the aqueous fluid itself.

**Fluid Inclusions in Meteoritic Halite** Two thermally-metamorphosed ordinary chondrite regolith breccias (Monahans 1998, hereafter simply “Monahans” (H5) and Zag (H3-6)) were found by us to contain fluid inclusion-bearing halite (NaCl) crystals (Zolensky et al. 1999, 2000) dated by K-Ar, Rb-Sr and I-Xe systematics to be ~4.5 billion years old (Zolensky et al., 1999, 2000; Whitby et al., 2000; Bogard et al., 2001), and thus the trapped aqueous fluids and solids are at least as ancient. Heating/freezing studies of the aqueous fluid inclusions in Monahans halites (Zolensky et al., 1999) demonstrated that they were trapped near 25°C, and their continued presence in the halite grains requires that their incorporation into the H chondrite asteroid occurred after that body’s metamorphism ended, since heating would have caused fluids to exit the halite (Zolensky et al., 1999). The initial results of our O and H isotopic measurements on Monahans and Zag halite brine inclusions (Yurimoto et al., 2014) can be explained by simple model mixing asteroidal and cometary water.

These halites also contain solids with a wide mineralogy, including abundant organics which we have been investigating by FTIR,  $\mu$ -L<sup>2</sup>MS, Raman spectroscopy, STXM-XANES, NanoSIMS, and UPLC-FD/QToF-MS (Kebukawa et al., 2014; Chan et al., 2018). These organics show a wide chemical variation, representing organic precursors, intermediates and reaction products that possibly include life’s precursor molecules. The halite crystals exhibit a diverse organic content that includes a mixture of C- and N-bearing materials comprising macromolecular carbon exhibiting a wide range of structural order, non-conjugated aromatic molecules, imine, nitrile and/or imidazole compounds, and amino acids. The solids and organics contain excesses of neutron-rich isotopes of H, O, N and Cr, requiring a very cold formation location. The enrichment in <sup>15</sup>N reflect sources of interstellar <sup>15</sup>N such as ammonia and amino acids. Our study reveals that the halite parent body, possibly a trans-neptunian object injected into the inner solar system by giant planet migration and becoming a C, P or D class asteroid (Vokrouhlický et al., 2016), shows evidence for a complex combination of biologically- and prebiologically-relevant molecules.

**Locating Fluid Inclusions In Other Astromaterials** The presence of fluid inclusions in the rather fragile halite crystals in Monahans and Zag suggested that fluids must have also been preserved in other meteoritic minerals, such as carbonates and silicates. This is supported by the discovery of decrepitated fluid inclusions in the nakhlites, appearing as dark trails through augite grains (Bridges et al., 2000). Therefore, we have been carefully examining newly-prepared thin sections of CM and CI chondrites for fluid inclusions, locating potential aqueous fluid inclusions in Ivuna (CI), Murray (CM2), Mighei (CM2), Sayama (CM2), ALH 84029 (CM2), Tagish Lake (C2) and LON 94101 (CM2), and Sutter’s Mill (C2) in carbonate, sulfide, olivine and enstatite crystals (Fig. 1). Optical, SEM and synchrotron X-ray computed tomography imaging indicate that calcite and sulfides in Sutter’s Mill have abundant, though very small, fluid inclusions (Tsuchiyama et al., 2014; Zolensky et al., 2017). The success of this survey demonstrates that we can expect to find aqueous fluid inclusions in numerous, varied meteorites. These inclusions had not been previously detected because they are very small (none larger than a few micrometers), and because of the high potential for creating spurious fluid inclusions during standard sample preparation procedures.

**Implications** It is well recognized that aqueous fluids, especially brines, were important in the early Solar System. Such fluids are probably present today below the surfaces of the icy moons Europa and Callisto (Hartogh et al., 2011). Brown and Hand (2013) proposed that NaCl and KCl dominate the non-ice component of the leading hemisphere of Europa, and that the most abundant salts in Europa ocean brines are chlorides. Samples of ancient, inner solar system water have survived in the form of aqueous fluid inclusions in chondrites and, probably, other classes of meteorites. Meteoritic fluid inclusions thus offer a unique opportunity to study early Solar System brines in the laboratory. Inclusion by inclusion analyses of the trapped fluids in carefully-selected samples will, in the immediate future, provide detailed information on the evolution of aqueous fluids as they interacted with anhydrous solid materials, and the evolution of prebiotic organic compounds. Thus, real data can replace calculated fluid compositions in thermochemical calculations of the evolution of water and aqueous reactions in comets, asteroids, moons and the terrestrial planets (Zolotov, 2008). Analysis of the organics that accompany these brine samples will shed important new light on the origin of life.

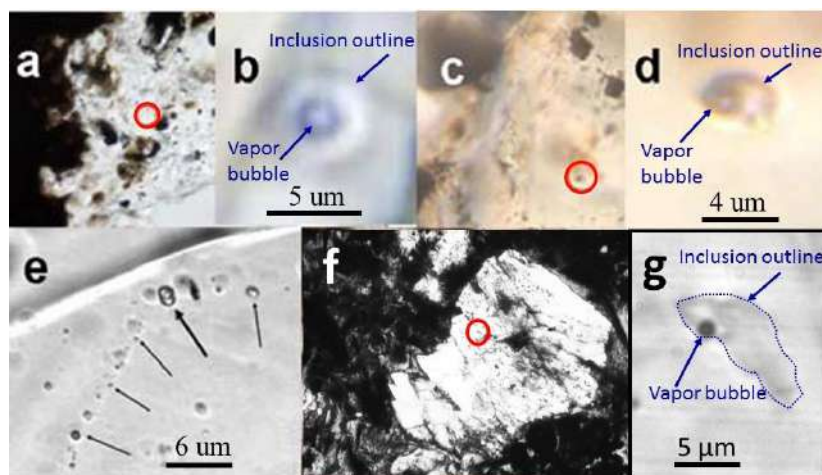


**Figure 1.** Two phase fluid inclusions in extraterrestrial calcite. (a) Primary fluid inclusion in the Murray CM2 chondrite at low mag. (circle). (b) Same Murray inclusion at high mag. (c) Primary fluid inclusion in the Tagish Lake C2 chondrite at low mag. (circle). (d) Same inclusion at high mag. (e) Secondary fluid inclusions in Tagish Lake. (f) Primary fluid inclusion in the Ivuna CI chondrite at low mag. (red circle). (g) Same Ivuna inclusion at high mag.

#### REFERENCES

- Bogard et al. (2001) *Meteoritics & Planetary Science* 36, 107-122.  
 Bridges et al. (2000) *Lunar and Planetary Institute Science Conference XXXI*, Abstract #1590.  
 Brown and Hand (2013) *The Astronomical Journal* 145, 110-117.  
 Chan et al. (2018) *Science Advances* 4 (p.eaao3521).  
 Cook et al. (2007) *The Astrophysical Journal* 663, 1406-1419.  
 Hartogh et al. (2011) *Nature* 478, 218-220.  
 Kebukawa et al. (2014) Abstracts, 77th Annual Meeting of the Meteoritical Society.  
 Lellouch et al. (2002) *Nature* 421, 45-47.  
 Tsuchiyama et al. (2014) Abstracts, 77th Annual Meeting of the Meteoritical Society.  
 Vokrouhlický et al. (2016) *The Astronomical Journal* 152:39, 1-20.  
 Whitby et al. (2000) *Science* 288, 1819-1821.  
 Yurimoto et al. (2014) *Geochemical Journal* 48, 1-12.  
 Zolensky et al. (1999) *Science* 285, 1377-1379.  
 Zolensky et al. (2000) *Lunar and Planetary Science XXXI*, The Lunar and Planetary Institute.  
 Zolensky et al. (2008) In *Oxygen in the Solar System*, MSA Revs. in *Mineralogy and Geochemistry* 68, pp. 429-462.  
 Zolensky et al. (2017) In *The Origin, History and Role of Water in the Evolution of the Inner Solar System*, *Philosophical Transactions of the Royal Society A*. 375, Article 20150386.  
 Zolotov (2008) *Lunar and Planetary Institute Science Conference XXXIX*, Abstract 2349.

## List of Participants

#	Name	Affiliation	E-mail address
1	Martin Appold	University of Missouri, USA	appoldm@missouri.edu
2	Wyatt Bain	University of Alberta, Canada	wbain@ualberta.ca
3	Stephen Becker	ExxonMobil, USA	stephen.becker@exxonmobil.com
4	Mitchell Bennett	USGS, USA	mbenn16@gmail.com
5	Márta Berkesi	Eötvös University Budapest, Hungary	marta.berkesi@gmail.com
6	Bob Bodnar	Virginia Tech, USA	rjb@vt.edu
7	Julien Bourdet	CSIRO Energy, Australia	julien.bourdet@csiro.au
8	Rosmer Brito Smith	ExxonMobil, USA	rosmerbrito@gmail.com
9	Philip Brown	University of Wisconsin, USA	pebrown@wisc.edu
10	Taras Bryndzia	Shell, USA	Taras.Bryndzia@shell.com
11	Bob Burruss	USGS (retired), USA	bob.burruss@gmail.com
12	Kristina Butler	The University of Texas at Austin, USA	kristina.butler@conocophillips.com
13	Lauren Cassel	Devon Energy, USA	lauren.cassel@dvn.com
14	Katrina Cox	Core Labs, USA	katrina.cox@corelab.com
15	Michael Decindis	University of Arizona, USA	mdecindis@email.arizona.edu
16	Tim Diggs	Aramco Services, USA	timothy.diggs@aramcoservices.com
17	Dom Druke	Independence Resources, USA	Dom.Druke@independenceresources.com
18	Vanessa Dyja-Person	H-Expertise Services, USA	vanessa.dyja-person@h-expertise-services.com
19	Hunter Edwards	Virginia Tech, USA	ehunter5@vt.edu
20	Alexy Elias-Bahnan	Université de Lorraine, France	alexey.elias-bahnan@univ-lorraine.fr
21	András Fall	The University of Texas at Austin, USA	andras.fall@beg.utexas.edu
22	Regina Ferreira	Denver, Colorado, USA	fluidinc@comcast.net
23	Stephanie Forstner	The University of Texas at Austin, USA	stephanie.forstner@beg.utexas.edu
24	Benedek Gál	ConocoPhillips, USA	Benedek.Gal@conocophillips.com
25	Bob Goldstein	University of Kansas, USA	gold@ku.edu
26	Gary Gray	Rice University, USA	ggg2@rice.edu
27	Tibor Guzmics	Eötvös University Budapest, Hungary	tibor.guzmics@gmail.com
28	Janet Haggerty	University of Tulsa, USA	janet-haggerty@utulsa.edu
29	Jordan Jensen	University of Arizona, USA	jljensen@email.arizona.edu
30	Sona Joseph	ExxonMobil, USA	sona.e.joseph@exxonmobil.com
31	Jan Braly Kihle	Institute for Energy Technology, Norway	jaki@ife.no
32	Yury Klyukin	Virginia Tech, USA	yury84@vt.edu
33	Hector Lamadrid	University of Toronto, Canada	hm.lamadrid@utoronto.ca
34	Pilar Lecumberri-Sanchez	University of Alberta, Canada	lecumber@ualberta.ca
35	Cin-Ty Lee	Rice University, USA	ctlee@rice.edu
36	Zhaoqi Li	CGG Houston, USA	haoqili83@gmail.com
37	Fang Lin	Chevron, USA	fanglin@chevron.com
38	Volker Lüders	GFZ Potsdam, Germany	value@gfz-potsdam.de

39	Gordon MacLeod	Chesapeake, USA	gordon.macleod@chk.com
40	Dan Marshall	Simon Fraser University, Canada	marshall@sfu.ca
41	Oscar Martínez Zárate	Université de Lorraine, France	oscar_martinez@uadec.edu.mx
42	Celestine Mercer	USGS, USA	cmercerc@usgs.gov
43	Raymond Michels	Georesources-CREGU, France	raymond.michels@univ-lorraine.fr
44	Madison Miller	University of Louisiana, USA	Madison.Miller@colorado.edu
45	Lowell R Moore	Virginia Tech, USA	moorelr@vt.edu
46	Megan Newcombe	Columbia University, USA	newcombe@ldeo.columbia.edu
47	Guangxi Ou	Research Institute of Uranium Geology, China	1508716884@qq.com
48	Jacques Pironon	Université de Lorraine, France	jacques.pironon@univ-lorraine.fr
49	Zsófia Poros	ConocoPhillips, USA	zsofia.poros@conocophillips.com
50	Bob Pottorf	ExxonMobil (Retired), USA	rjpotto@gmail.com
51	Jim Reynolds	Fluid Inc, USA	fluidinc@comcast.net
52	John Ridley	Colorado State Univeristy, USA	jridley@colostate.edu
53	Eszter Sendula	Virginia Tech, USA	eszter1@vt.edu
54	Sandra Siljeström	RISE Research Institutes of Sweden	sandra.siljestrom@ri.se
55	Adam Simon	University of Michigan, USA	simonac@umich.edu
56	Jinny Sisson	University of Houston, USA	j_sisson@netzero.com
57	Christopher Smith	University of Arizona, USA	smithcm1@email.arizona.edu
58	Dennis Smith	AHS, USA	dp.smith@earthlink.net
59	Mike Smith	AHS, USA	ahstrat@aol.com
60	Sarah Smith	University of Missouri	ses7f1@mail.missouri.edu
61	Timothy Smith	AHS, USA	tracesmith8@aol.com
62	Marta Sośnicka	GFZ Potsdam, Germany	sosnickamarta@gmail.com
63	John Stainforth	Shell	JGStain@aol.com
64	Matthew Steele-MacInnis	University of Alberta	steelema@ualberta.ca
65	Cole Stringer	AHS, USA	c.c.stringer15@gmail.com
66	Shelley Stringer	AHS, USA	shelleystringer7@gmail.com
67	Matt Sublett Jr	Virginia Tech, USA	dsublett@vt.edu
68	Laura Taylor	University of Houston, USA	taylorllaura@gmail.com
69	Heather Vandergriff	Virginia Tech, USA	heathv7@vt.edu
70	Esra Inan Villegas	Shell, USA	esra.inan@shell.com
71	Ed Waddington	University of Washington, USA	edw@uw.edu
72	David T Wang	ExxonMobil, USA	david.t.wang@exxonmobil.com
73	Qiqi Wang	The University of Texas at Austin, USA	wangqiqi@utexas.edu
74	Matt Wasson	ConocoPhillips, USA	Matt.S.Wasson@conocophillips.com
75	Jim Webster	American Museum of Natural History, USA	jdw@amnh.org
76	Zoltán Zajacz	University of Toronto, Canada	zajacz@es.utoronto.ca
77	Min Zhang	China University of Petroleum, China	zhangmin715@126.com
78	Michael Zolensky	NASA Johnson Space Center, USA	michael.e.zolensky@nasa.gov



## Notes









